

OBSERVATIONAL AND TIMING STUDIES  
OF COMPACT BINARIES CONTAINING  
COMPACT OBJECTS AND EVOLVED STARS

**Kyle Alan Corcoran**

Grand Rapids, Michigan

B.S. Physics, High Point University, 2019  
M.S. Astronomy, University of Virginia, 2021

A Dissertation Presented to the  
Graduate Faculty of the  
*University of Virginia*  
in Candidacy for the Degree of  
*Doctor of Philosophy*

Department of Astronomy

University of Virginia  
December 2024

Committee Members:  
Scott M. Ransom  
Steven R. Majewski  
Phil Arras  
Thomas Kupfer  
David A. Nichols

© Copyright by  
Kyle Alan Corcoran  
All rights reserved  
December, 2024

*Me: Ellorie, did you know I've been in school this whole time?*

*Ellorie: Oh no! I forgot that!*



# ABSTRACT

Compact binary stars are a cornerstone of and often the first step in exploring some of the most interesting processes in the Universe. These systems, which typically have orbital periods of less than a day, take on many different appearances and probe various points of stellar evolution. Some populations of binary stars are large and well studied, while others are smaller and therefore benefit from each new discovery and characterization of its class. It is only through complementary and comprehensive studies of the variety of binary types that we hope to gain a more cohesive picture of how these systems and their constituent parts evolve and give way to other interesting astrophysical phenomena.

This thesis presents investigations of three different types of compact binaries. These studies assume complementary approaches to characterize stellar systems via observational, computational, and timing techniques, as well as to describe individual systems and their populations. Chapter 2 presents a case study of a B-type hot subdwarf (sdB) and the optical photometry and spectroscopy obtained to characterize it. The study of this system represents the first effort in a forthcoming series of papers aimed at increasing and better-characterizing the compact, binary-hot-subdwarf population. Chapter 3 describes an analysis of 45 previously classified white dwarf–main sequence (WDMS) binaries using high-resolution, near-infrared spectra from the Apache Point Galactic Evolution Experiment. This study not only added additional

systems to the number of compact WDMS systems – arguably the largest population of compact binaries that have undergone common-envelope evolution – with derived orbital periods but it also pointed out potential alterations to the chemical composition of the MS companion during the common-envelope phase. Finally, Chapter 4 presents a new technique for achieving long-term timing solutions of redback (RB) millisecond pulsars. Owing to the erratic nature of the orbit and circumbinary material in these systems, previous studies could only track the rotation of the pulsar over baselines of a few years. By decoupling the pulsar’s spin from its binary orbit, we show that RB spin parameters could be derived from almost 20 years of archival data.

## ACKNOWLEDGEMENTS

To say my graduate school experience looked very different at times (well I guess most of the time) from what is typical seems, objectively, like an understatement. This thesis and the things in it would not have been possible without the guidance, help, grace, and support of countless peers, collaborators, and loved ones. It is impossible to name everyone here, but please know that I appreciate all of you as you've joined me on this journey.

To Brad and the rest of my High Point physics family, what was once a dream inspired by all of your passions is now coming to a close as reality. Undeclared, freshman-year me would never have believed all of what I've been able to do and accomplish as a result of all of the mentorship I received throughout undergrad. I owe a lot of who I am as a scientist and as a person to you all, and I wouldn't have made that leap had it not been for you, Brad.

To Mark, Connor, and Xinlun, thank you for joining me in countless rabbit holes we explored in the pursuit of physics. From our conversations about dark photons to our numerous April Fools' arXiv ideas to our scheduling of puppy time to mitigate the effects of super cry festive, I couldn't have survived the first year of grad school without you. Connor, you showed me the power of having a vertical monitor, and I always know where I can go for linux help. Xinlun, wading into research our first year felt so much more attainable with another first-year student in the group navigating

the same process, and I'm not sure I could have been as productive without your help. Mark, I'm still not sure we aren't the same person, but, as long as you keep your hair longer, people can hopefully tell us apart in appearance. Also to Samer, thank you for formally increasing our year's cohort by 25%.

To the  $N + 1$  and  $N - 1$  years from me, thank you for braving homework sets and class projects alongside me. I appreciate you bearing with me through re-explaining things you just explained to me multiple times, especially when I was struggling to type out equations on a keynote document we were using as a whiteboard rather than just writing them down on paper. We will always have those quick trips to do Pokémon Go raids, the many outtakes from wavelength and other games, and, of course, our ever-growing volleyball cult (even though I have to live vicariously through pictures now).

To Chris, Robby, and Hannah, thank you for your wisdom, help, and support during my time in Steve's research group. I learned many of the skills and much of the APOGEE knowledge I needed to do my own research from discussions of your work. You all played an integral part in my choosing UVA, and I can't express in words how grateful I am for that.

To Deven, thank you for all your help as I tried to understand pulsars, debug code, and figure out why whatever batch of short-chunk searches I was doing at the time stopped with no error outputs (a common occurrence for me). I'm still sorry one of the first days I was able to come into the NRAO offices in almost two years happened to be the day they were getting names for the door unbeknownst to us all, and that I sat at your desk that day.

To Alex (the dangerous one), Alex (Alex 2), Olivia, Rey, Tasha, and the many other pulsar friends that have joined in the group since I started four years ago, thank you for your shared love of really spinnny stars. I've learned a lot about the

many facets of analyzing radio data from you all that I never truly thought about given the weird, messy nature of the pulsars I've conditioned myself to believe are normal when in fact they are some of the least normal.

To Thomas, thank you for encouraging me to pursue my crazy ideas chasing short-period, white dwarf binaries and for your collaboration. I appreciate the time you took to help me learn.

To Steve, thank you for your guidance and support during my time in your group. I learned much about scientific writing and observing through your help, feedback, and teaching.

To Scott, I don't think I can thank you enough for everything you've done for me and all your support during our time together. Balancing research, life, and keeping tiny humans alive has certainly been the most difficult thing that I've had to do thus far in my life, and I know that hasn't made me an ideal PhD student. Your patience understanding, and advocacy has made all the difference in getting to this point. If you ever need someone to break some code you didn't think it was possible to break, I hope you know I'm always up to the task.

To Aaron and Amy, our LCC small group, and the rest of the LCC community, thank you for helping our family to grow so much in faith during our time in Palmyra and Charlottesville.

To my family and Kelsey's family, thank you for support and encouragement as I've completed this work. I've never been the best at communicating what it is that I actually do, but you still cheer me on and ask how to help as I do it.

To Ellorie and Easton, as I write the last bits of this section, we are watching an episode of the *Magic of Disney's Animal Kingdom* together. Every time I switch tabs, you ask me where my book went, Ellorie, and you won't let me set you down, Easton. I love you both with all my heart, and I wouldn't trade the time I got to

spend with you during the completion of this degree for the world. To future children we hope to have, at times your brother and sister made this whole grad school thing feel more stressful than it actually probably was in the best way possible, don't lord it over them too much.

To Kelsey, the love of my life, I don't think there is a way to fully encapsulate how thankful I am for your love and support in this journey. You've been with me since my first astrophysics presentation ever (even though it was at the same math conference where I didn't go to your presentation), through the gauntlet of grad school visits and all of the ups and downs grad school and life has to offer. I am so very grateful you were with me through these parts of our lives, and I'm so excited to start the next chapter with you and our family.

Finally, to God, through whom all of this is possible, be the honor and glory. As with every birthday card my grandparents sent me over the years, I leave you, the reader, with a verse to look up, ponder, and study.

With love,

Kyle

Psalm 8:3–4

# TABLE OF CONTENTS

<b>Abstract</b>	<b>v</b>
<b>Acknowledgements</b>	<b>vii</b>
<b>List of Figures</b>	<b>xvi</b>
<b>List of Tables</b>	<b>xvii</b>
<b>1 An Introduction to Various Compact Binaries</b>	<b>1</b>
1.1 Hot Subdwarf Stars . . . . .	2
1.2 White Dwarf–Main Sequence Binaries . . . . .	4
1.3 Redback Millisecond Pulsars . . . . .	6
1.4 Dissertation Overview . . . . .	8
1.5 Contributions . . . . .	9
<b>2 Discovery of a Deeply Eclipsing sdB+dM System</b>	<b>13</b>
2.1 Introduction . . . . .	13
2.2 Discovery Run . . . . .	16
2.3 Time–Series Spectroscopy . . . . .	18
2.3.1 Observations & Reductions . . . . .	18
2.3.2 Radial Velocity Curve . . . . .	19
2.3.3 Atmospheric Parameters . . . . .	21
2.4 Time–Series Photometry . . . . .	23
2.4.1 Observations & Reductions . . . . .	23
2.4.2 Binary Light Curve Modeling . . . . .	25
2.4.3 Orbital Ephemeris . . . . .	31
2.5 System Parameters . . . . .	31
2.6 Discussion . . . . .	32
2.7 Summary . . . . .	35
2.8 Appendix . . . . .	36
<b>3 Analysis of Previously Classified White Dwarf–Main Sequence Binaries</b>	<b>41</b>

3.1	Introduction . . . . .	41
3.2	The APOGEE Survey . . . . .	45
3.3	Global Assessment of the Previously Identified WDMS Systems . . . . .	47
3.4	Analysis of System Architectures . . . . .	54
3.4.1	<i>The Joker</i> Orbital Analysis of the Radial Velocities . . . . .	54
3.4.2	Estimating the Stellar Masses . . . . .	56
3.5	Descriptions of Individual Systems . . . . .	57
3.5.1	2M10243847+1624582 . . . . .	57
3.5.2	2M10552625+4729228 . . . . .	58
3.5.3	2M11463394+0055104 . . . . .	60
3.5.4	2M13054173+3037005 . . . . .	60
3.5.5	2M14544500+4626456 . . . . .	62
3.5.6	Wide Binaries . . . . .	65
3.5.7	Targets with 2-5 RV Visits . . . . .	66
3.5.8	Targets with a Single Visit . . . . .	69
3.6	Metallicity Distribution of WDMS Systems . . . . .	69
3.7	Summary . . . . .	76
3.8	Appendix: Systems with One or less High-Quality Visits . . . . .	78
<b>4</b>	<b>Long-term Timing of Redback Millisecond Pulsars in Globular Clusters</b>	<b>81</b>
4.1	Introduction . . . . .	81
4.2	Observations . . . . .	85
4.3	Timing Methodology . . . . .	86
4.3.1	Detections and Initial $T_{0,x}$ Measurements . . . . .	86
4.3.2	Producing TOAs . . . . .	88
4.3.3	Updating Orbital Properties . . . . .	89
4.3.4	Constructing Piecewise-Continuous Groups & Parameter Files . . . . .	90
4.3.5	Refining $T_{0,x}$ with TEMPO . . . . .	93
4.3.6	Refining $T_{0,x}$ via BTX Information & Gaussian Process Regression . . . . .	93
4.3.7	Isolating the MSP . . . . .	95
4.3.8	Fitting & Inflating Uncertainties . . . . .	96
4.4	Results . . . . .	97
4.4.1	Pulse Profiles . . . . .	97
4.4.2	Phase Variations . . . . .	97
4.4.3	Long-term Timing Solutions . . . . .	99
4.5	Discussion . . . . .	99
4.5.1	Applegate Model Applied to Ter5P . . . . .	99
4.5.2	Timing Solutions . . . . .	101
4.5.3	Positions and Proper Motions . . . . .	102
4.5.4	ROI Timing vs. Traditional Timing . . . . .	103
4.5.5	Phase Variation Analyses . . . . .	105

TABLE OF CONTENTS

xiii

4.5.6	Mitigating Systematics in the Future . . . . .	107
4.6	Summary . . . . .	108
4.7	Appendix: Dynamical Considerations . . . . .	109
4.7.1	Relating $T_0$ to $P_b$ & $\dot{P}_b$ . . . . .	109
4.7.2	Relating $T_0$ to $x$ . . . . .	110
4.7.3	Quadrupole Moments . . . . .	111
4.8	Appendix: Supplementary Tables . . . . .	113
<b>5</b>	<b>Future Work</b>	<b>121</b>
	<b>References</b>	<b>125</b>



# LIST OF FIGURES

1.1	<i>Gaia</i> CMD that highlights hot subdwarfs from Culpan et al. (2022) . . . . .	4
2.1	Discovery light curve and reduced SOAR/Goodman frames . . . . .	17
2.2	Radial velocity curves from SOAR/Goodman low-resolution spectra of our sdB+dM . . . . .	20
2.3	Atmospheric fits to H Balmer and He I lines in our 2019 spectra . . . . .	23
2.4	Apparent $T_{\text{eff}}$ , $\log g$ , & $\log y$ variations as a function of orbital phase . . . . .	24
2.5	Johnson $B$ & $R$ filter light curves and models . . . . .	28
2.6	Surface gravities as a function of sdB mass for potential mass ratio solutions . . . . .	29
2.7	Mass–radius diagram for the dM companion’s potential solutions . . . . .	34
2.8	Corner plot of the most probable light curve solution for $B$ data . . . . .	37
2.9	Corner plot of the most probable light curve solution for $R$ data . . . . .	38
3.1	CMD and Kiel diagram for confirmed or candidate WDMS systems in our sample . . . . .	48
3.2	Radial velocity curve for 2M10243847+1624582 . . . . .	58
3.3	Radial velocity curve for 2M10552625+4729228 . . . . .	59
3.4	Radial velocity curve for 2M11463394+0055104 . . . . .	61
3.5	Radial velocity curve for 2M13054173+3037005 . . . . .	63
3.6	Radial velocity curve for 2M14544500+4626456 . . . . .	64
3.7	Example of <i>The Joker</i> outputs used to place limits on orbital periods of WDMS systems with low numbers of visits . . . . .	66
3.8	Metallicity distributions and cumulative distributions for the WDMS systems in the wide binary and post-common-envelope samples . . . . .	72
3.9	Calculated orbit of 2M14244053+4929580 . . . . .	74
3.10	Mass ratio as a function of orbital period for our five systems and previously known systems . . . . .	75
4.1	Pulse profiles for the five RBs analyzed here . . . . .	84
4.2	Progression of $T_{0,x}$ measurements after applying various accuracy refinements . . . . .	87

4.3	Final $\Delta T_0$ values as a function of time and associated power spectral densities for all five RBs . . . . .	91
4.4	Timing residuals for all five RBs using our technique . . . . .	98
4.5	$\Delta T_0$ for Ter5P and NGC 6440D before and after removing their $\dot{P}_b$ .	100
4.6	Comparison of our technique with conventional methods . . . . .	104
4.7	Fractional deviation for our five RBs and Ter5A as a function of spin period & frequency, orbital period, and projected semi-major axis . .	106

# LIST OF TABLES

2.1	Parameters used to model $B$ and $R$ light curves for our sdB+dM . . .	30
2.2	Derived parameters for our sdB+dM from most probable solution . .	33
2.3	All of the possible light curve solutions output by LCURVE . . . . .	39
3.1	General information on the 45 WDMS systems/candidates . . . . .	53
3.2	Orbital parameters derived for wide binary and post-common-envelope, WDMS systems with <i>The Joker</i> . . . . .	68
3.3	Data for APOGEE systems in the cleaned sample with zero or one quality visit. . . . .	78
4.1	The final measurements of $T_{0,x}$ used in constructing the piecewise- continuous groups for each system. . . . .	115
4.2	Timing parameters for the RBs in Terzan 5 . . . . .	118
4.3	Timing parameters for M28H and NGC 6440D . . . . .	119



## CHAPTER 1

# AN INTRODUCTION TO VARIOUS COMPACT BINARIES

A majority of stars participate in binary or higher order star systems, and these systems come in a variety of stellar combinations and orbital configurations. As an ensemble, these multiple star systems provide vital tools for learning about numerous interesting astrophysical processes initiated by binary star interactions. Some of the most interesting astrophysical laboratories are binary systems with compact orbits. These systems, with periods ranging from a few minutes (Burdge et al., 2019) to even a few days, provide us the opportunity to study a range of particularly energetic astrophysical phenomena. Some compact binaries are the origins of Type Ia supernovae (Toloza et al., 2019), others allow us to test general relativity (Hulse & Taylor, 1975), and all sub-classes provide unique insights into binary evolution dependent on the mass ratios and initial binary separations. In the text that follows, I briefly introduce just a few of the many kinds of compact binaries and comment on their importance to understanding open questions in relevant sub-fields. Then, I give an overview of the structure of the subsequent chapters.

## 1.1 HOT SUBDWARF STARS

Evolving low-mass ( $< 8 M_{\odot}$ ) stars can produce core helium-burning stars of B-type known as hot subdwarfs (sdB). The most common avenue for forming these stars is that, as core-hydrogen fusion stops and the star begins to ascend the red giant branch, binary interactions can remove the envelope, leaving behind the helium core. The latter describes the common evolutionary element for two of the three formation scenarios thought to account for hot subdwarfs (Han et al., 2002, 2003); the third formation scenario does not depend on binary star evolution. The first channel is through an initial binary with a separation such that, as the star evolves, Roche lobe overflow to a K-type or earlier companion creates a wide binary containing a hot subdwarf. In these systems, the observed orbital periods – i.e., 10 days to around 1500 days – are much longer than that of compact binaries. Spectroscopic observations of these binaries reveal features from both the primary and secondary star, leading to their common moniker of “composite binaries.” There are many interesting physics problems that can be addressed using hot subdwarfs in composite binaries (see Vos et al., 2019); however, these are outside the scope of this thesis. More applicable to my studies is the second formation channel, in which the evolving giant envelopes the companion and the system enters a common envelope (CE) phase (see Ivanova et al., 2013, for a review). Angular momentum from the binary orbit can then be deposited into the envelope, and this process ejects the envelope from the system to leave behind the giant’s core. By virtue of closer initial separations, the resultant binaries are also found in short period orbits of typically a few hours (Maxted et al., 2001). Unlike their wider counterparts, the hot subdwarf is a dominant source of luminosity in the system, predominantly outshining its companion. Often the secondary in these systems is an M dwarf; however, more brown dwarf and white dwarf (WD) companions have been

found in recent years.

The observed properties of these short period binaries make them relatively distinguishable from other types of compact binaries. In the color-magnitude diagram (CMD), these systems live just blueward of the blue edge of the blue horizontal branch along the so-called extended horizontal branch. They are sub-luminous relative to their main sequence counterparts while also outshining the brightest WDs on the traditional cooling track. This places them apart, as seen in Figure 1.1, essentially only overlapping with other kinds of compact binaries containing a WD (e.g., cataclysmic variables) (Geier et al., 2019). Photometric and spectroscopic variability are also commonplace for these systems. Optical light curves display a wide range of variability such as pressure- and gravity-mode pulsations, eclipses, a significant reflection effect due to the irradiation of the close companions, and even ellipsoidal modulation and Doppler beaming (Barlow et al., 2022). Typical spectroscopic temperatures for these stars range from 20000 to 40000 K, and they display strong H Balmer lines. Time-series observations yield radial velocities (RV) that track the primary over the duration of the orbital period, and some systems even show the Roemer delay (Barlow et al., 2012).

There are many open questions in studies of hot subdwarfs in compact orbits, not all of which can be addressed here (see Heber, 2016, for a thorough review). Although mostly anecdotal, an active question in the field is whether the sdB mass ( $0.47 M_{\odot}$ ) often assumed in analyses of these systems is canonical or not (Han et al., 2002, 2003). The total population of sdB systems with full parameter solutions is still relatively small ( $< 100$ ), however, and the absence of double-line spectroscopic binaries means that deriving dynamical masses is not possible. Another common question stemming from the generally accepted formation channel of these binaries is what the minimum mass of the companion needs to be to remove the envelope. This question has far-

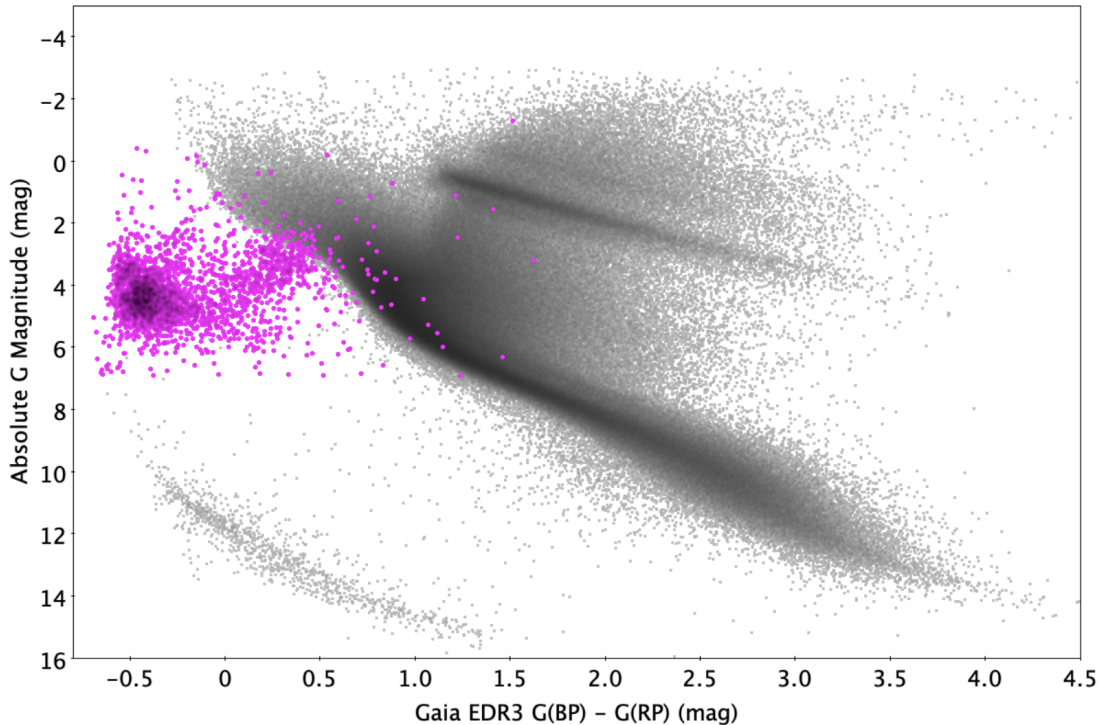


Figure 1.1: Figure from Culpan et al. (2022) highlighting the locations of hot subdwarf systems and candidates observed by *Gaia* in a CMD. Here  $G$ ,  $G_{BP}$ , and  $G_{RP}$  are the *Gaia* green, blue, and red passbands, respectively.

reaching implications for the effects sub-stellar and planetary mass objects have on the late stages of stellar evolution (Soker, 1998; Schaffenroth et al., 2014a, 2019). Hot subdwarfs with a massive WD companion can have orbits less than an hour, which can make them exceptional producers of gravitational waves. Therefore, investigations as to their viability as verification sources for the Laser Interferometer Space Antenna mission are of significant interest (Kupfer et al., 2024).

## 1.2 WHITE DWARF–MAIN SEQUENCE BINARIES

For binaries containing two low-mass, main sequence (MS) stars, the story is often not unlike that of a single, isolated star. In many of these systems, the two stars are separated from each other sufficiently to evolve independently. The more massive star

will naturally complete this process first, leading to a wide binary that now contains a WD and a MS star (Willems & Kolb, 2004). However, around 25% of these so-called WDMS binaries evolve more similarly to the systems in Section 1.1. With smaller initial separations, these stars enter a CE phase, leading, as previously discussed, to the ejection of the envelope from the system (Webbink, 2008). These post-CE binaries (PCEBs) also shrink from intermediate to shorter periods during this phase, and have various types of companions, albeit most commonly an M dwarf.

One of the things that makes WDMS binaries such an attractive class of compact binaries for study is the larger population of known and candidate systems. These systems have been popular targets of all-sky spectroscopic surveys such as the Sloan Digital Sky Survey (SDSS; Rebassa-Mansergas et al., 2016a), the Large sky Area Multi-Object fiber Spectroscopic Telescope survey (Ren et al., 2018), and the WD Binary Pathways Survey (Parsons et al., 2016; Rebassa-Mansergas et al., 2017) to name a few. The prevalence of spectra also means that a wealth of spectroscopic parameters are available to be paired with those derived from various all-sky photometric surveys (such as SDSS Rebassa-Mansergas et al., 2013), further increasing the number of potential systems. For PCEBs, there is an ever-growing population of more than 300 systems, with over a third of those having derived orbital periods (see the survey papers above, Miszalski et al., 2009; Nebot Gómez-Morán et al., 2011; Brown et al., 2023, and referenes therein). The distribution of orbital periods peaks around eight hours (Miszalski et al., 2009; Nebot Gómez-Morán et al., 2011) for these systems, and the most commonly cited maximum period for PCEBs is 100 days; however, a very small sample of systems have periods greater than this and may be formed through a distinct channel of the CE phase (Kawahara et al., 2018; Masuda et al., 2019). With the multi-visit strategies often employed in these surveys, time-series analyses can be done to derive RVs, which act as an additional avenue to derive

masses; moreover, some systems also show eclipses in optical photometry that can be used in constraining masses, too. These values can be paired with the atmospheric parameters from the combined, high-signal-to-noise spectra often published in the survey to give statistical views of the population (e.g., Camacho et al., 2014; Cojocaru et al., 2017).

The size of the PCEB population within the WDMS samples makes it a natural choice for exploring the physics of the CE and post-CE phases (Zorotovic et al., 2011) despite some biases toward hot WDs with late-type, M-dwarf companions in the overall sample of WDMS systems (Rebassa-Mansergas et al., 2016a; Ren et al., 2018). With so many systems in these catalogs, spectroscopically vetting and confirming potential systems is an ongoing process. Addressing some of the biases in the overall population by targeting underrepresented systems (such as cool WDs and non-M dwarf companions) also helps bring us towards a more complete sample (Parsons et al., 2016; Anguiano et al., 2022; Brown et al., 2023). This effort is well founded, as these systems provide insights into many interesting physics problems outside of just CE-evolution, such as orbital evolution via magnetic braking (Schreiber et al., 2010), gravitational wave emission and Type Ia supernova progenitors (Tolosa et al., 2019), age-metallicity relationships (Rebassa-Mansergas et al., 2016b), theoretical mass-radius relationships (Parsons et al., 2012a,b), and many more.

### 1.3 REDBACK MILLISECOND PULSARS

Although sharing some similarities rooted in binary interactions, rotating neutron stars (NS), called pulsars, have a vastly different evolutionary history than all the stars mentioned to this point. These small, extremely dense objects are born out of the evolution of high-mass stars ( $> 8 M_{\odot}$ ) after electron degeneracy pressure fails to support the star's core against mounting gravitational forces. A core-collapse

supernova (Type Ib, Ic, and II) leaves behind a NS (Large et al., 1968) that, through conservation of angular momentum, rotates and emits electromagnetic radiation from its magnetic poles (Pacini, 1967; Gold, 1968). Eventually these pulsars will spin down significantly and cross what is called the “death line,” after which the pulsar will turn off (Chen & Ruderman, 1993); however, binary companions can transfer mass to these dead pulsars, bringing along angular momentum that “recycles” the NSs to extremely short spin periods on the order of milliseconds (Alpar et al., 1982). These so-called millisecond pulsars (MSPs) are naturally found in close binary systems, typically with a low-mass, WD companion (Manchester et al., 2005; Tauris & van den Heuvel, 2006).

However, other MSP systems have companions not unlike some discussed in the previous two sections. The so-called “spider” pulsar family has members with a diverse set of companion types and proposed evolutionary states, such as the “hunter” with red giant companions (Swihart et al., 2018), the “tidarrens” with almost-planetary-mass companions (Romani et al., 2016), and the “false widows” which behave much more similarly to low-mass, X-ray binaries (LMXBs; Knight et al., 2023). More prevalent in the spider population, though, are the “black widows” (BW) and “redbacks” (RB), named for their propensity to ablate material from their companion and thus “devour” it. These two binary types share many similarities, including radio eclipses (e.g., Nice et al., 1990), drastic heating via the pulsar wind that can lead to optical variations (Bellm et al., 2016; Burdge et al., 2022), X-ray emission (Strader et al., 2019; Swihart et al., 2022), and even  $\gamma$ -ray pulsations (Nieder et al., 2020; Thongmeekom et al., 2024). The most obvious way to distinguish between these systems is by their companion mass, with BWs having lower-mass  $M_c < 0.1 M_\odot$  companions and RBs having  $0.1 M_\odot \lesssim M_c < 0.9 M_\odot$ , similar to low-mass, main sequence stars (Roberts, 2013; Strader et al., 2019; Swihart et al., 2022). These systems are present both in the Galactic field and globular clusters.

Both BWs and RBs, with their multi-wavelength nature, are popular choices for studying many astrophysical questions. These systems are often sought after in attempts to connect LMXBs to isolated MSPs (van den Heuvel & van Paradijs, 1988) in the theory of pulsar recycling. However, the population of these systems is not yet large enough to draw definitive conclusions in this process. Both BWs and RBs often harbor NSs that range from well above the canonical value  $1.4 M_{\odot}$  (e.g., Strader et al., 2019) to the most massive known NSs (Cromartie et al., 2020; Romani et al., 2022). This makes these binaries vital in studies probing the elusive, NS equation of state. Globular clusters, as effective factories for producing binaries and NSs, often host a handful of spiders that can be used in learning more about the cluster (Ransom et al., 2005; Prager et al., 2017). Short- to long-term follow-up observations also allow for pulsar timing techniques to provide valuable measurements on many system parameters in both BWs (e.g., Cromartie et al., 2020; Romani et al., 2022) and RBs (e.g., Nice et al., 2000).

## 1.4 DISSERTATION OVERVIEW

In this thesis, I detail my use of various observational, computational, and timing techniques to understand these various types of binaries. While not directly related to each other, the methods and results I will present are largely applicable to both their individual sub-fields as well as the broader area of compact binaries. In Chapter 2, I present a case-study of a deeply-eclipsing, hot subdwarf binary that, despite its unique photometric behavior, displays typical properties in the context of this population of binaries. This work highlights how dedicated spectroscopic and photometric follow-up observations in the optical can be used to understand individual systems better, leading eventually to a more-cohesive understanding of the population. In Chapter 3, I discuss new analyses of a small sample of WDMS binaries found in the

literature using properties derived from high-resolution, near-infrared spectroscopy. This work was not only a pilot effort for constructing a larger catalog of WDMS candidates, but it also highlights how long-term, spectroscopic surveys can be used to validate literature classifications, analyze sparsely sampled RV information, and better understand potential differences between populations formed through separate formation channels. In Chapter 4, I describe a novel technique developed to perform long-term timing studies of the MSP spin behavior in RBs, as well as the solutions for five systems that span nearly two decades of observation. In addition to the many methods involved in obtaining these timing solutions, this work shows how even messy and unconventional binaries can be used to study interesting astrophysical questions. Finally, I will review some of the key takeaways from each chapter, and I will comment on some possible future studies that have been enabled by these works.

## 1.5 CONTRIBUTIONS

At the time of this writing, both Chapters 2 and 3 have been published in peer-reviewed journals. Chapter 4 is currently being prepared for submission to *The Astrophysical Journal*. The references to these works are given at the beginning of each chapter.

I led Chapter 2 as first author, writing a majority of the text. However, the analyses presented were a collective effort by me and my co-authors. I did the analysis that led us to select this system for observations, participated in the discovery and spectroscopic observations, extracted the discovery light curve, performed the period finding analysis with *TESS*, fit the RV data, and created the ephemeris. Dr. Brad Barlow participated in all observations, reduced the data and prepared it for modeling, and performed the multi-color light curve and RV extractions, Dr. Veronika Schaffenroth performed the light curve modeling and stacked atmospheric modeling, Dr. Ulrich

Heber and Dr. Andreas Irgang performed the phase dependent atmospheric modeling shown in Figure 2.4 and helped improve the text describing the atmospheric modeling, and Stephen Walser participated in the observations and created Figure 2.7.

In Chapter 3, a large portion of the analyses were performed by myself, and I led the project as first author. The text is a combination of writing from myself, Dr. Steve Majewski, and Dr. Hannah Lewis. The orbital analysis of 2M14244053+4929580 was performed by Devin McDonald, the mass ratio analysis (i.e., Figure 3.10) was performed by Dr. Hannah Lewis, and the text and discussion on the young stellar objects was greatly aided by Dr. Marina Kounkel. Dr. Hannah Lewis also performed independent orbital analyses using *The Joker* for some of the systems, and aid from and discussions with her were pivotal in my bringing those analyses to fruition. Many co-authors also contributed fruitful discussion that improved the contents of the paper prior to publication.

Finally, Chapter 4 contains another first-author work where much of the analysis was performed by me. The majority of the text was written by me. Dr. Scott Ransom performed all of the time-series-data preparation, acquired SPIDER\_TWISTER detections for some of the RBs, created the pulse profiles in Figure 4.1, performed the orbital period derivative fitting for Ter5P and NGC 6440D, generated Tables 4.2 and 4.3, and performed the timing of NGC 6440D via conventional timing methods. Alexandra Rosenthal wrote the original code used to create the power spectral densities shown in Figure 4.3, and Dr. Scott Ransom wrote or contributed to the codes used for performing the BTX-derived- $T_0$  predictions, the pulsar “isolation,” the power spectral densities, and the Gaussian process regressions. The binary-piecewise model in PINT was developed by Dr. Patrick O’Neill. The observations used throughout the chapter are from a long-term monitoring program, and we made use of data obtained by Dr. Megan DeCesar, Dr. Paulo Freire, Dr. Jason Hessels, Dr. Ryan Lynch, Dr.

Scott Ransom, and Dr. Ingrid Stairs. Dr. Phil Arras helped with or derived many of the equations in Appendix 4.7, and many of them were originally presented by Dr. Brian Prager in (Prager, 2017).



## CHAPTER 2

# DISCOVERY OF A DEEPLY ECLIPSING SDB+DM SYSTEM

This chapter was originally published as Corcoran et al. (2021a).

## 2.1 INTRODUCTION

Most hot subdwarfs are core He–burning extreme horizontal branch (EHB) stars that formed from red giant progenitors that experienced mass loss near the tip of the giant branch, due to binary interactions (see Heber, 2016, for a detailed review). With temperatures from 20,000–45,000 K and spectra dominated by broad H Balmer lines, they are classified either as sdB stars or sdOB stars if they display the He II 4686 Å line. They show a tight mass distribution peaking near  $0.47M_{\odot}$  (the ‘canonical’ mass) and have radii around  $0.2R_{\odot}$ . Theoretical models such as those in Han et al. (2002, 2003) describe sdB formation scenarios that account for the mass loss in these systems, with three possible formation channels depending on the initial configuration and mass ratio of the binary. One formation channel produces an sdB via Roche lobe overflow (RLOF) to a MS companion of K type and earlier. The binaries that

form in this way are typically wide binaries ( $P = 10 - 1500$  d). These systems are often called “composite” binaries, as both stars are seen in the spectrum and account for 30 – 40% of all sdBs (for an overview see, Vos et al., 2019). The rest of the sdBs do not show any signs of a companion in their spectra. Maxted et al. (2001) showed that a high fraction of those sdBs do exist in short-period binaries leading to radial velocity variations. Those can be formed by common envelope (CE) evolution, which produces close binaries with periods as short as  $\sim 1.5$  hr with a hot subdwarf primary and a cool, low-mass companion. In this scenario, an evolving red giant and a companion object enter a CE, and the angular momentum resonant in the orbit of the binary is deposited into the envelope, ejecting it from the system. Typically, this companion is stellar in nature; however, Soker (1998) proposed that sub-stellar and even planetary mass companions could be sufficient to provide the orbital angular momentum necessary to eject the envelope (e.g., Schaffenroth et al., 2015). The remaining sdBs do not show any radial velocity variations and hence appear single. Such single sdBs could be formed by the merger of two He WDs. Another possibility is that a substellar companion was responsible for the mass loss, which was destroyed during the common envelope phase.

The main challenge in studying close sdB binaries and their properties comes from the single-lined nature of these systems, allowing only for mass limits inferred based on the proposed inclination; however, some systems benefit from the presence of an eclipse, which helps to constrain the inclination and allows for more precise mass measurements. These so called HW Vir systems also show photometric variation due to the reflection effect and have orbital periods of  $P < 1$  d, making them vital tools for sdB studies due to the relative ease in identifying them. The prototypical HW Vir is an sdB and M dwarf (dM) binary. A few systems containing a brown dwarf (BD) have also been discovered (e.g., Schaffenroth et al., 2014a).

The Eclipsing Reflection Effect Binaries from Optical Surveys (EREBOS) project (Schaffenroth et al., 2019) is an effort to increase the sample of known HW Vir systems and to measure orbital, atmospheric, and fundamental parameters of those binaries. EREBOS is especially interested in finding the lower-mass limit of an object able to remove the envelope in a CE phase and survive this phase in order to investigate the effect that sub-stellar companions have on the late stages of stellar evolution. Moreover, this project aims at studying post-CE systems spanning the entire range of periods and companion masses for these systems. For a better understanding of the poorly understood common envelope phase, see Ivanova et al. (2013). Until recently, the number of HW Vir binaries with known fundamental parameters was relatively small at 18 total systems. The EREBOS project dramatically increased this number by inspecting light curves from the Optical Gravitational Lensing Experiment (OGLE; Pietrukowicz et al., 2013; Soszyński et al., 2015) and Asteroid Terrestrial-impact Last Alert System (ATLAS; Tonry et al., 2018) surveys, finding over 150 new HW Vir candidates (Schaffenroth et al., 2019). With an extensive spectroscopic and photometric follow up campaign we will dramatically increase the number of systems with robust solutions.

Despite this unprecedented increase, HW Virs still represent only a small fraction of the sdB population. Given the typical radii of both components, these systems have to be relatively edge-on to show any eclipse. For example, the smallest, grazing eclipses occur in systems such ASAS 102322–3737 (Schaffenroth et al., 2013), a sdB+dM, at  $i = 65.9^\circ$ ; however, inclinations do range up to perfectly edge-on systems such as AA Dor (Kilkenny et al., 1978), a sdOB+dM/BD. One HW Vir system, Konkoly J064029.1+385652.2 (Derekas et al., 2015), is an sdO+dM binary that even shows a total eclipse due to a relatively small ( $R = 0.096 R_\odot$ ) sdO being in a nearly edge on ( $i = 87.11$ ) orbit with an inflated dM. Total eclipses are sometimes seen in

WD+dM binaries such as NN Ser (Parsons et al., 2010a), where a high inclination angle allows the dM to completely block the smaller WD along our line of sight. Due to the similarity in size between typical sdBs and dMs, even edge on systems struggle to achieve geometries sufficient to produce a total eclipse.

Here we present system parameters for the first deeply eclipsing sdB+dM system, *Gaia* DR2 6097540197980557440, which exhibits an eclipse in excess of  $\sim 5$  magnitudes in the optical. We discovered *Gaia* DR2 6097540197980557440 in the course of the EREBOS project while obtaining follow-up observations of known HW Virs using the Goodman spectrograph (Clemens et al., 2004) on the 4.1-m Southern Astrophysical Research (SOAR). In §2.2 we describe the initial observations leading to its discovery. In §2.3 we present time-series spectroscopic observations as well as the radial velocities and atmospheric parameters derived from them. In §2.4 we present multi-color, time-series photometric observations and the details of our light curve modeling solution. §2.5 presents system parameters derived from the best-fitting light curve modeling solution. In §4.5, we discuss how the system compares to the EREBOS sample at large, as well as potential follow-up studies. Finally, we summarize our work in §4.6.

## 2.2 DISCOVERY RUN

During a small amount of down time between SOAR/Goodman observations of EREBOS targets on 2019 June 9, we discovered *Gaia* DR2 6097540197980557440 with approximately 45 minutes of time-series photometry using Goodman in imaging mode with a Johnson *V* filter. We had previously identified *Gaia* DR2 6097540197980557440 as a strong candidate variable hot subdwarf from its anomalously high *Gaia* DR2 photometric uncertainty, and its inclusion in the Geier et al. (2019) catalog of candidate hot subdwarf stars (see Guidry et al., 2020; Barlow et al., 2022, for details). We unwittingly began observing just before primary eclipse and, upon noticing the star

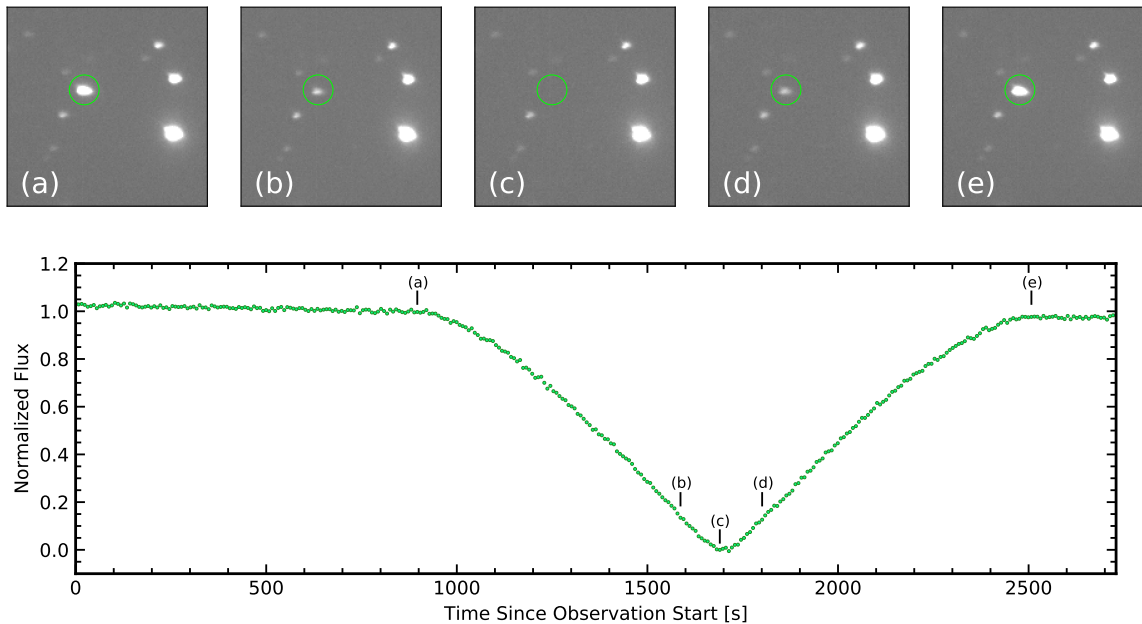


Figure 2.1: Discovery data for *Gaia* DR2 6097540197980557440 from SOAR/Goodman. *Top*: Raw Johnson *V* filter frames from the discovery data set obtained on 2019 June 9. We highlight five select frames corresponding to the marked locations on the light curve in the bottom panel. These frames represent phases (a) just prior to ingress, (b) shortly before the systems drops below detection limits, (c) during primary eclipse totality, (d) shortly after the system returns above detection limits, and (e) just after egress. *Bottom*: The corresponding light curve of *Gaia* DR2 6097540197980557440 in the Johnson *V* filter.

disappear from the raw image frames<sup>1</sup> (shown in Figure 2.1), continued observing long enough to safely capture egress. Using the processes described in §2.4.1, we constructed a light curve and determined that the primary eclipse lasted approximately 25 minutes. The shape of the eclipse stuck out to us immediately as being different than in other HW Vir binaries. Whereas the ingress and egress segments of most primary eclipses have *positive* second time derivatives (i.e., concave up), *Gaia* DR2 6097540197980557440’s second derivatives are *negative* during ingress and egress (i.e., concave down). This can only be explained by the geometry of a nearly perfectly

<sup>1</sup>At this moment, Stephen Walser, who was monitoring the frames as they came in, apologetically informed us he had ‘lost our star.’

edge-on eclipse, so we were eager to obtain photometry and spectroscopy over the full orbit to solve for all system parameters.

Unfortunately, we were unable to determine a precise orbital period for the system using our exploratory time-series photometry. However, *Gaia* DR2 6097540197980557440 was also observed by TESS in Sector 11 through full-frame image (FFI), 30-min cadence observations. The data were downloaded from the Mikulski Archive for Space Telescopes (MAST) web portal, and the `lightkurve` (Lightkurve Collaboration et al., 2018) Python package was used to extract time-series photometry from the FFIs. A Lomb-Scargle periodogram (Scargle, 1982) was computed and yielded an initial estimate of the system’s orbital period of  $P = 3.0614$  hr. This estimate helped guide subsequent observations.

## 2.3 TIME-SERIES SPECTROSCOPY

### 2.3.1 Observations & Reductions

We obtained 53 spectra using SOAR/Goodman on 2019 July 25 and 46 spectra on 2020 February 17, both in an uninterrupted series of back-to-back exposures. Each of these data sets covered roughly 75% of the  $\sim 3$ -hr orbital period. We used the 0.8'' long slit,  $2 \times 2$  binning, and the  $930 \text{ mm}^{-1}$  VPH grating (0.84 Å per binned pixel dispersion), giving us average spectral resolutions of 2.38 Å and 2.04 Å over the wavelength range 3600-5300 Å for the 2019 and 2020 data, respectively. We note that the spectral resolutions are different despite using the same instrumental configuration due to the camera-collimator focus values not being set to their optimal values during the 2019 observations. On both observing nights, we aligned the slit axis to a position angle of  $278.3^\circ$  E of N in order to place a bright star<sup>2</sup> 23.5'' away on

---

<sup>2</sup>Gaia DR2 6097528446950034944

the slit and monitor any drifts in the wavelength solution due to instrumental flexure. Individual spectra in each series were integrated for 120-s, yielding an average S/N of  $\sim 30$  per resolution element. We also obtained spectra of FeAr lamps immediately following each series for wavelength calibration purposes.

Reduction of the frames was carried out using the `ccdproc` task in `IRAF` (Tody, 1986, 1993). After bias-subtracting and flat-fielding all spectral images, we ran the `apall` task to extract a one-dimensional spectrum for each frame and remove a fit to the sky background. For the 2020 data, a wavelength solution was generated from the FeAr lamp spectra and applied to all individual spectra. We note that slow drifts in the wavelength solution over the course of the series are expected due to instrumental flexure, and thus the FeAr wavelength solution does not provide an accurate zero-point — only an accurate dispersion solution. For the 2019 data, an intermittent issue with the FeAr lamp prevented us from obtaining an accurate dispersion solution with it. Instead, we created a self template from the combined 2019 spectra and use the Balmer and He I lines to determine the wavelength solution. Once again, this only provides a dispersion solution and not an absolute RV zero point. Consequently, we are unable to report on the binary’s systemic velocity. The spectrum of *Gaia* DR2 6097540197980557440, shown in Figure 2.3, is dominated by strong H Balmer absorption features and weaker He I lines (4026, 4471, 4921, 5015 Å). The absence of the He II 4686 Å line rules out an sdOB classification.

### 2.3.2 Radial Velocity Curve

Radial velocity (RV) shifts were determined from non-linear, least-squares fits of Gaussian profiles to the sdB H Balmer lines, which was carried out using the `curve_fit` function in the Python package `scipy` (Virtanen et al., 2020a). The He I profiles were too noisy in individual spectra for this purpose. In order to correct

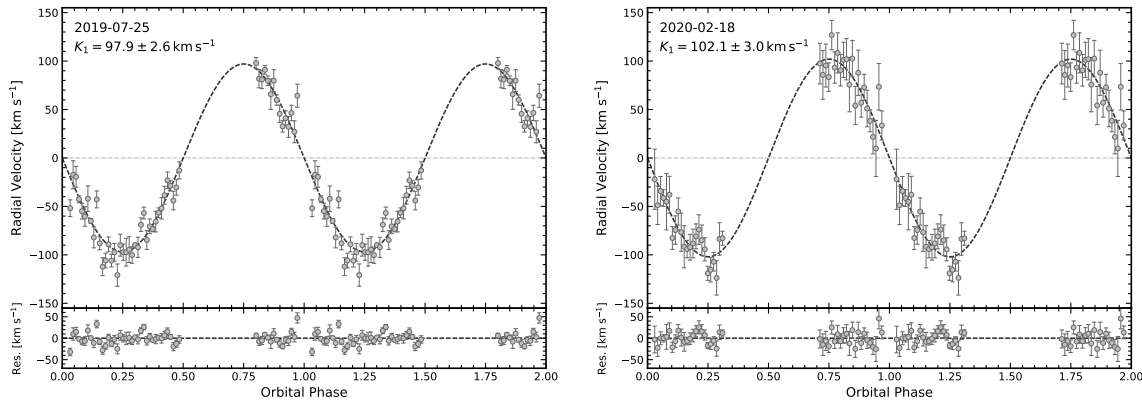


Figure 2.2: Radial velocity curves constructed from spectra obtained with SOAR/Goodman, plotted twice for better visualization. *Left:* Best fitting model for the data taken in 2019. *Right:* Best fitting model for the data taken in 2020. Both of these solutions agree within the error bars with the weighted average  $K_{\text{sdb}} = 100.0 \pm 2.0 \text{ km s}^{-1}$ .

for drifts in the wavelength solution (and thus drifts in the RVs) due to instrumental flexure during the observations, we also measured the relative velocity shifts of the absorption features of the second star on the slit. This object displayed spectral features consistent with a G/K-type star, and so we used the `crosscorrRV` function in the `PyAstronomy` library (Czesla et al., 2019) to measure velocity shifts via cross correlation. The second star’s RV curves revealed gradual, nearly-linear shifts on the order of  $\sim 75 \text{ km s}^{-1}$  over  $\sim 2$  hours, in both the 2019 and 2020 data sets. The magnitude and pattern of these shifts — slightly different on the two nights — were consistent with expectations given the target’s RA, DEC, average hour angle during each run, and associated Nasmyth cage rotations. We are confident they are due to instrumental flexure and not intrinsic RV variations of the second star on the slit. To remove this flexure drift from the target RV curves, we fitted low-order polynomials to the comparison star’s RV curves and subtracted this fit from the raw target star RV curves. The resulting RV curves are shown in Figure 2.2.

In order to determine the RV semi-amplitude of the sdB ( $K_{\text{sdb}}$ ), we fitted sine waves to each of the data sets separately, with the orbital period and phase fixed to the values described in §2.4.2. From the 2019 July 25 data, we find  $K_{\text{sdb}} = 97.9 \pm 2.6 \text{ km s}^{-1}$ , and from the 2020 February 17 data, we derive  $K_{\text{sdb}} = 102.1 \pm 3.0 \text{ km s}^{-1}$ . These results agree within their  $1\text{-}\sigma$  uncertainties, and we adopt as our final RV semi-amplitude their weighted average:  $K_{\text{sdb}} = 100.0 \pm 2.0 \text{ km s}^{-1}$ . The residuals in the bottom panels of Figure 2.2 are consistent with random noise and show the data are consistent with a circular orbit, as expected for post-common-envelope HW Vir binaries.

### 2.3.3 Atmospheric Parameters

For use in the spectroscopic analysis, model spectra are computed following the so-called hybrid approach (Przybilla et al., 2006b,a; Nieva & Przybilla, 2008). In this approach, deviations from local thermodynamic equilibrium (LTE) can be treated very efficiently using a combination of updated versions of the ATLAS12 (Kurucz, 1996), DETAIL (Giddings, 1981; Butler & Giddings, 1985), and SURFACE (Giddings, 1981; Butler & Giddings, 1985) codes. The ATLAS12 code, for which we use here the mean metallicity for hot sdBs according to Naslim et al. (2013), is initially used to compute the temperature/density structure of a line-blanketed, plane-parallel, and chemically homogeneous atmosphere in hydrostatic and radiative equilibrium. This LTE atmosphere is then used as input for the DETAIL code, which solves the coupled radiative transfer and statistical equilibrium equations to obtain occupation numbers in NLTE for hydrogen and helium. Finally, the SURFACE code is used to compute the final synthetic spectrum using the atmosphere from ATLAS12 and the occupation numbers from DETAIL as well as more sophisticated line-broadening data. Also taken into consideration are the recent improvements to all three codes (Irrgang et al.,

2018) concerning NLTE effects on the atmospheric structure, the implementation of the occupation probability formalism (Hubeny et al., 1994) for hydrogen and neutral helium, and new Stark broadening tables for hydrogen (Tremblay & Bergeron, 2009) and neutral helium (Beauchamp et al., 1997). The application of these models to sdBs is also shown in Schaffenroth et al. (2020).

The observed spectra are matched to the model grid by  $\chi^2$  minimization as described by Saffer et al. (1994) as implemented by Napiwotzki et al. (1999). We use six H Balmer lines and four He I lines. H  $\epsilon$  is excluded because of contamination by interstellar Ca II. Since the binary orbit is so tight, tidal friction probably has spun up the sdB star, which causes extra line broadening. However, the resolution of the spectra is insufficient to measure the projected rotational velocity  $v \sin i$ . We assume that the rotation of the sdB is tidally locked to the binary orbit and convolve the model spectrum with a rotational broadening profile with a corresponding  $v \sin i = 87 \text{ km s}^{-1}$  in the fitting procedure.

Previous studies have shown that some sdBs with reflection effects have atmospheric parameters that can vary with phase when analyzing spectra of sufficiently high S/N taken at different phases of the orbit (e.g., Schaffenroth et al., 2013, 2014b). These variations can be explained by the companion’s phase-variable contributions to the spectrum from only the reflection effect, causing apparent variations of order 1000 – 1500 K and 0.1 dex in the sdB temperature and surface gravity, respectively.

To account for any of these variations, we derived the atmospheric parameters from the single-radial velocity corrected spectra. Exemplary fits are shown for individual spectra from the 2019 and 2020 observing runs for similar orbital phases in Fig. 2.3. Results from both observing runs are consistent. The variations of the atmospheric parameters, which are consistent with previous determinations, can be seen in Fig. 2.4. The effective temperature appears to increase slightly near the

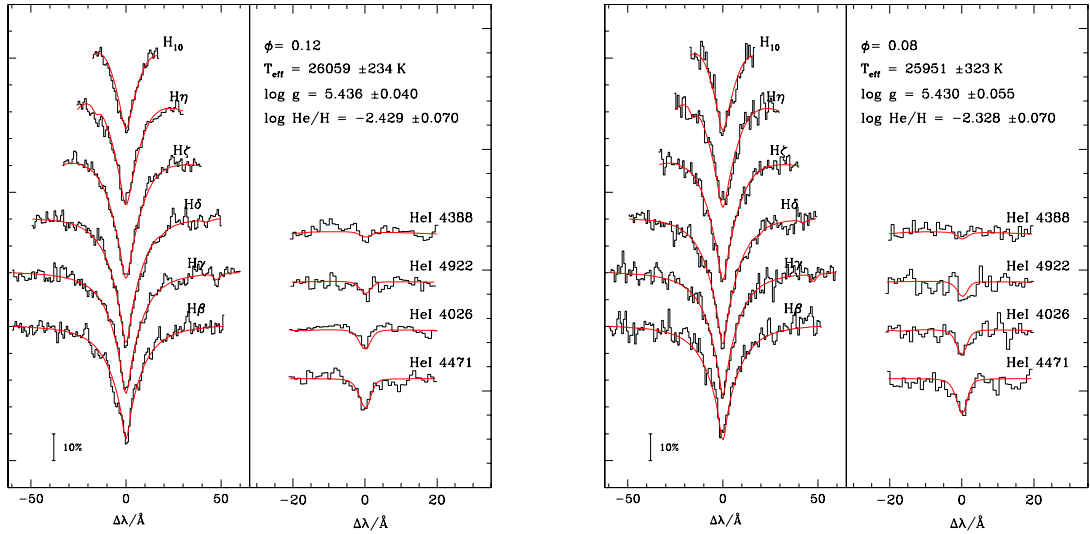


Figure 2.3: Line fits to the hydrogen Balmer and neutral helium lines in individual SOAR/Goodman spectra from 2019 (left hand panel) and 2020 (right hand panel). Listed in the upper right of each panel is the orbital phase and the resulting set of best fitting atmospheric parameters.

secondary eclipse. Any variations in the surface gravity or helium abundance ( $\log y$ ) remain below detection limits. In order to determine the atmospheric parameters of the sdB we averaged the parameters near the primary eclipse, where only the dark side of the companion is visible:  $T_{\text{eff}} = 26100 \pm 400\text{K}$ ,  $\log(g) = 5.50 \pm 0.07$ , and  $\log(y) = -2.32 \pm 0.10$ .

## 2.4 TIME-SERIES PHOTOMETRY

### 2.4.1 Observations & Reductions

Follow-up time-series photometry was obtained on 2020 February 18 using SOAR with the Goodman spectrograph in imaging mode. In an effort to obtain multi-color photometry for more precise modeling, the filter wheel was manually switched between the Johnson  $B$  and  $R$  filters every few minutes when not in primary or

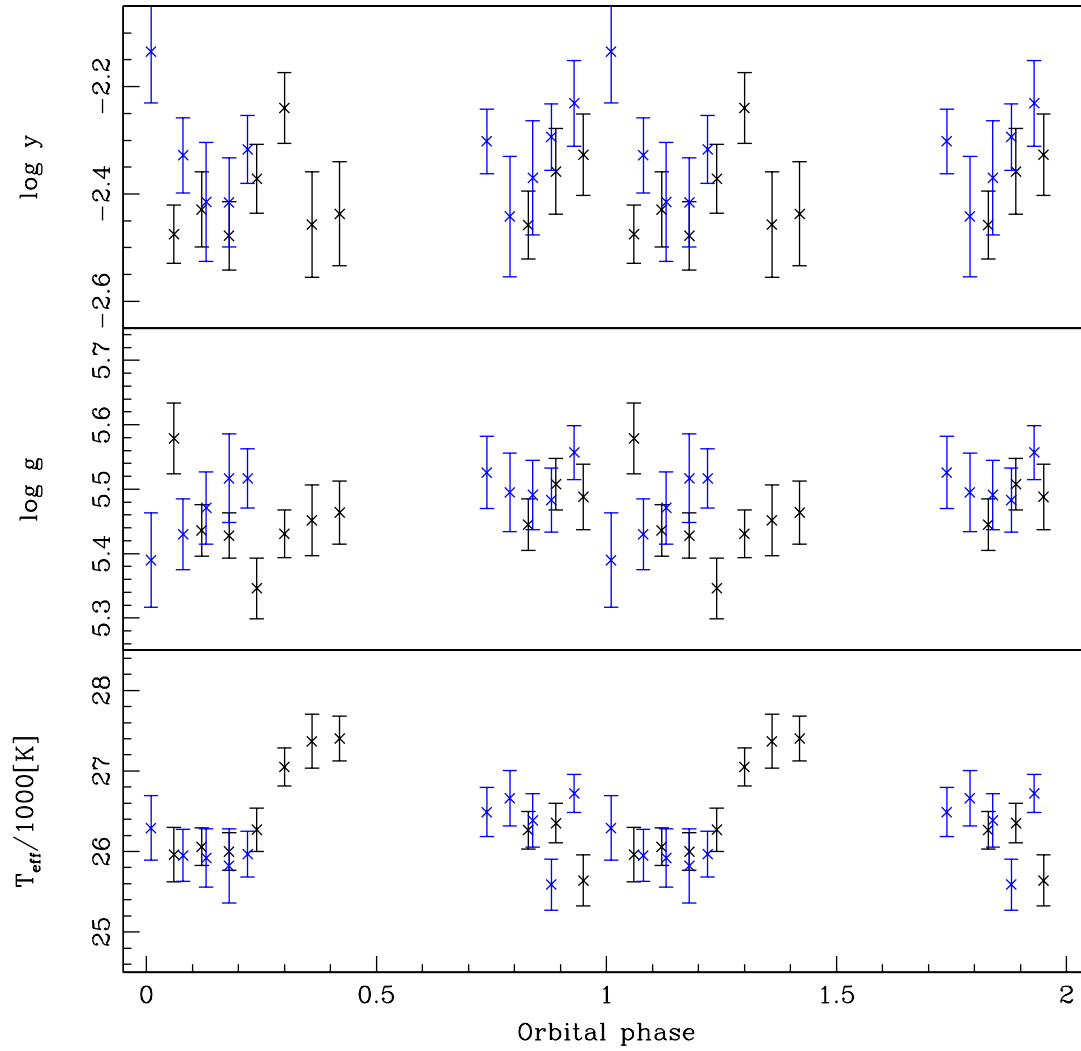


Figure 2.4: Apparent  $T_{\text{eff}}$  (bottom),  $\log g$  (middle),  $\log y$  (top) variations with  $1 \sigma$  error bars as a function of the orbital phase. Results from spectra taken in 2019 are shown in black while those from 2020 in blue.

secondary eclipse, and every 30 seconds during eclipses. The integration time was fixed to 5 seconds for both filters in order to minimize dead time and errors associated with changing this value back and forth every few minutes. We used  $2 \times 2$  binning and read out only a  $350 \times 175$  binned pixel subset of the image to minimize the readout time between exposures. This relatively small field still provided several nearby comparison stars through which to track sky transparency variations. We achieved a duty cycle of roughly 54% over the course of our observations, which covered a little more than one full orbital period. A more efficient duty cycle would have required either decreasing the subframe region further and sacrificing comparison stars, or increasing the exposure time and risk saturating the target and comparison stars.

Reduction of the SOAR frames was once again carried out using the `ccdproc` procedure in IRAF. Each raw image frame was first bias-subtracted and flat-fielded. We then extracted aperture photometry using a range of aperture sizes with a custom code utilizing the `photutils` (Bradley et al., 2019) Python package. Sky counts were removed using sky annuli drawn around the apertures. Apertures were chosen to maximize the signal-to-noise ratio (S/N) in each light curve. This process was repeated on multiple nearby, bright comparison stars to remove sky transparency variations and flux-normalize the light curves. Multiple cycles of observing are typically needed to remove airmass-related changes in the flux, therefore, any of these slight flux variations were not removed during the reduction process. The resulting differential light curves are shown in Figure 2.5 and used for modeling the binary.

### 2.4.2 Binary Light Curve Modeling

The *Gaia* DR2 6097540197980557440 light curve exhibits all the typical HW Vir features. The amplitude of the reflection effect is noticeably stronger in the *R* filter

( $\sim 30\%$ ) than in the  $B$  filter ( $\sim 20\%$ ), and it is quite strong in general compared to other reflection effect systems. Initially, this led us to believe that either the sdB was slightly hotter than in typical HW Virs, or the companion was slightly larger than usual. The deep primary eclipse, implying a nearly edge-on inclination, lent credence to the latter explanation. The shape of the eclipse itself sticks out amongst other HW Vir binaries. As mentioned in Section 2.2, the ingress and egress segments of the primary eclipse have negative second derivatives (more V-shaped) instead of the more frequently observed positive second derivatives (more U-shaped). This implies the eclipse geometry is nearly perfectly edge-on and that the companion might be slightly larger than the primary. Secondary eclipses are also present in the light curve, during which the sdB is blocking irradiated light from the cool companion. Notably, the flux at the center of the secondary eclipse returns to its exact value immediately preceding and following ingress and egress, respectively — further implying that the inclination must be nearly edge-on.

To model the light curves, we use the code `LCURVE` (for details, see Appendix A in Copperwheat et al., 2010). In addition to recreating deep eclipses, `LCURVE` was designed for binaries with WDs and has been used to fit WD+dM systems exhibiting the reflection effect (e.g., Parsons et al., 2010a); therefore, HW Vir binaries are naturally suited to be modeled in a similar fashion (see Schaffenroth et al., 2020, for an example and further details). To form full solutions for these systems, there are many parameters that are not all independent, so we can greatly improve our ability to constrain each solution by fixing as many parameters as possible. We fixed the sdB temperature to the value determined in our spectroscopic fit (described in §2.3.3). We also fix the gravitational limb darkening coefficients to values expected of a primary with a radiative atmosphere (von Zeipel, 1924) and a companion with a convective atmosphere (Lucy, 1967) by calculating the resulting intensities using a blackbody

approximation. Then we adopted a quadratic limb darkening law for the primary using the values in Claret & Bloemen (2011) closest to the parameters derived in our spectroscopic fits.

It is important to note that there is a large degeneracy in the light curve solutions of HW Vir binaries, even when fixing all of the above parameters. The orbit is certainly almost circular, so each model is not sensitive to the mass ratio ( $q$ ) of the system. For this reason we calculated different solutions over a range of various, fixed mass ratios. We then use a SIMPLEX algorithm (Press et al., 1992) to vary parameters such as the inclination, both radii, the companion’s temperature, albedo, and limb darkening, and even the period and primary eclipse time to help localize the solutions. Additionally, we allow for linear trends due to airmass-related changes in flux over the course of the observations.

Next we tested the degeneracy of each light curve solution and determined the parameter errors by performing Markov-Chain Monte-Carlo (MCMC) computations using `emcee` (Foreman-Mackey et al., 2013). We used the best-fit solution from our SIMPLEX algorithm for initial values, and then we again varied the inclination angle, both radii, the limb darkening coefficient assuming a linear limb darkening law for the companion, and the companion’s temperature and albedo for the mass ratio of our most probable solution (see §2.5). In all cases, the temperature of the companion is not well constrained as its fractional luminosity contribution to the system — outside of the reflection effect — is negligible. We therefore constrained the companion’s temperature to the range 2500 – 3500 K (the expected range for the low-mass companion). The results and errors from our `emcee` run (shown in Table 2.1) then form the basis for our most probable solution.

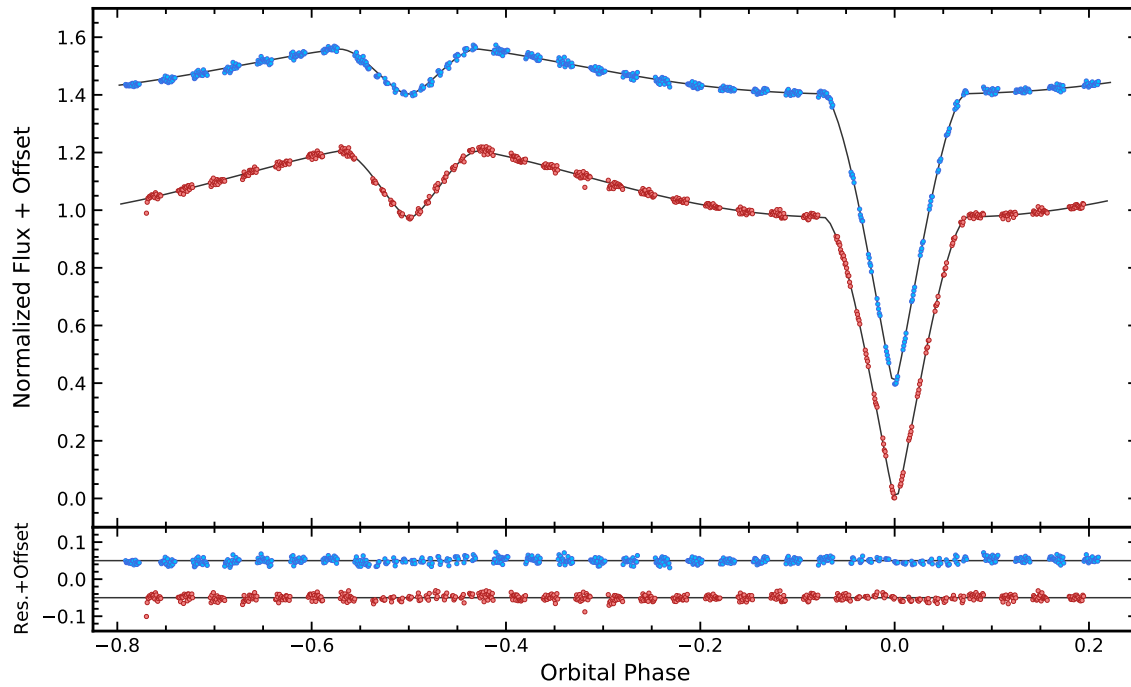


Figure 2.5: SOAR/Goodman light curves of *Gaia* DR2 6097540197980557440 in both the Johnson *B* (blue points) and *R* (red points) filters, along with their respective best-fitting models from §2.4.2. The *B*-filter light curve is offset by 0.4 for better visualization. Residuals are shown in the bottom panel with offsets of 0.05 and  $-0.05$  for the *B* and *R* curves, respectively.

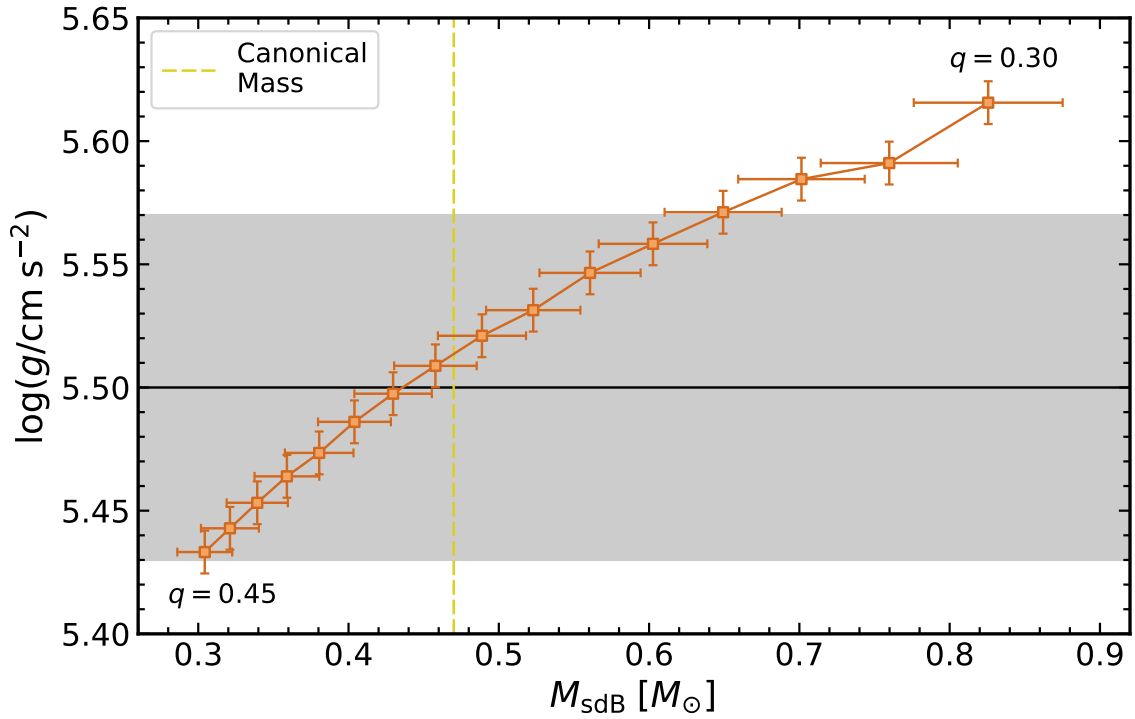


Figure 2.6: Photometric surface gravities plotted against their respective sdB masses for different mass ratio solutions ranging from  $q = 0.3 - 0.45$ , in 0.01 increments. The solid horizontal line (black) and shaded area represent the spectroscopically-derived  $\log(g)$  and associated  $1\text{-}\sigma$  error, respectively. The vertical dashed line (yellow) represents the canonical sdB mass of  $0.47 M_{\odot}$ . The intersection of these two lines shows that our most probable solution is the one with a sdB mass just below the canonical mass.

Table 2.1: Parameters used to model the light curve for both the SOAR/Goodman  $B$  and  $R$  data.

Parameter	SOAR/Goodman – $B$	SOAR/Goodman – $R$	Unit	Description
Fixed Parameters				
$q$ ( $M_{\text{dM}}/M_{\text{sdb}}$ )	0.375	0.375		mass ratio
$P$	0.127037	0.127037	d	orbital period
$T_{\text{sdb}}$	26100	26100	K	primary temperature from spectroscopy
$g_1$	0.25	0.25		gravitational darkening exponent
$g_2$	0.08	0.08		gravitational darkening exponent
$x_{1,a}$	0.097	0.070		primary linear limb darkening coefficient
$x_{1,b}$	0.285	0.222		primary quadratic limb darkening coefficient
Adjusted Parameters				
$i$	$90^{+0.0}_{-0.3}$	$90^{+0.0}_{-0.4}$	$^{\circ}$	inclination angle
$x_{2,a}$	0.2992	0.2734		companion linear limb darkening coefficient
$R_{\text{sdb}}/a$	$0.2180 \pm 0.0007$	$0.2174 \pm 0.0007$		primary radius
$R_{\text{dM}}/a$	$0.2402 \pm 0.0006$	$0.2407 \pm 0.0006$		companion radius
$T_{\text{dM}}$	$2800 \pm 500$	$3100 \pm 500$	K	companion temperature
$A_2$	$1.14 \pm 0.01$	$1.4 \pm 0.01$		companion albedo (absorb)
$m$	$0.00026 \pm 0.00001$	$0.00026 \pm 0.00001$		slope

### 2.4.3 Orbital Ephemeris

To aid in future observations of *Gaia* DR2 6097540197980557440, we have listed its orbital ephemeris ( $T_0$ ,  $P$ ) in Table 2.2. We adopt the orbital period from our best fit `emcee` solution in §2.4.2. To construct an initial eclipse time ( $T_0$ ), we fit inverted Gaussian profiles to both the  $B$  and  $R$  time-series data using `curve_fit`. We then adopt the weighted average of the central times from both filter series as our  $T_0$  value.

## 2.5 SYSTEM PARAMETERS

In Figure 2.6, we plot the surface gravity and sdB mass for each of the potential solutions, and we compare the photometric surface gravities to our spectroscopically derived surface gravity.

Based on the spectroscopic surface gravity, we get a consistent solution for an sdB mass of  $0.3 - 0.64 M_\odot$ . All possible solutions fit the light curve data nearly equally well; thus, we cannot claim a unique solution without additional data (e.g., velocity measurements from the dM). The most probable solution is the one with an sdB mass consistent with the canonical mass of  $0.47 M_\odot$ . The adopted best-fitting light curve solution and all relevant parameters are given in Table 2.1, and both of these best-fit models are shown together with their respective observations and residuals in Figure 2.5. All possible solutions are given in Table 2.3 of the Appendix.

We compute the binary mass function for *Gaia* DR2 6097540197980557440 using the expression

$$f = \frac{K_{\text{sdb}}^3 P}{2\pi G} = \frac{M_{\text{sdb}} q^3 \sin^3 i}{(1+q)^2}, \quad (2.1)$$

finding  $f = 0.0132 \pm 0.0008 M_\odot$  using the period and sdB velocity semi-amplitude. Combining this with the adopted mass ratio derived before, we find the sdB and dM masses to be  $M_{\text{sdb}} = 0.47 \pm 0.03 M_\odot$  and  $M_{\text{dM}} = 0.18 \pm 0.01 M_\odot$ , respectively. Using

Kepler’s third law, we then find the orbital separation to be  $a = 0.921 \pm 0.018 R_{\odot}$ . We also find  $R_{\text{sdb}} = 0.199 \pm 0.004 R_{\odot}$  and  $R_{\text{dm}} = 0.222 \pm 0.004 R_{\odot}$ . Table 2.2 gives an overview of the adopted parameters for *Gaia* DR2 6097540197980557440.

In Figure 2.7, we show each set of parameters for the companion and the theoretical mass-radius relations for low-mass main sequence stars from Baraffe et al. (2015) as an additional check. It is clear that each solution yields a companion radius that is inflated relative to what is predicted by theory, which is a trend commonly seen in close binaries with M dwarf components (Parsons et al., 2018). For our most probable solution we get a companion inflation of about  $\sim 13\%$ .

## 2.6 DISCUSSION

Our analysis of *Gaia* DR2 6097540197980557440 represents the first EREBOS case study following the Schaffenroth et al. (2019) report of newly discovered sdb+dm systems. With each additional system that is solved, EREBOS comes one step closer to achieving one of its goals to make statistical statements about a homogeneously selected population of close sdb systems. While one new system by itself might not push the boundaries of key parameters in these studies, each system provides self-consistent feedback about the methodology used to study the overall population. It is only through these self-consistent measures that EREBOS can eventually make statements regarding the effects stellar and sub-stellar companions have on the late stages of stellar evolution.

Our light curve and atmospheric modeling solutions imply *Gaia* DR2 6097540197980557440 is a fairly typical sdb+dm system, aside from the chance alignment of its orbital plane nearly perfectly along our line-of-sight. The peak of the EREBOS orbital period distribution for both new and previously-published systems from Schaffenroth et al. (2019) is at  $P = 0.1$  d, meaning that *Gaia* DR2 6097540197980557440 falls at the

Table 2.2: Overview of derived parameters for *Gaia* DR2 6097540197980557440 that represent the most probable solution from the set of potential solutions.

Parameter	Value	Unit
Basic Information		
$\alpha^{a,b}$	213.577775581303	deg
$\delta^{a,b}$	-43.552249057309	deg
$G^a$	16.358994	mag
$G_{\text{bp}} - G_{\text{rp}}^a$	-0.27529526	mag
System Properties		
$T_0$	$2458898.85724 \pm 0.00003$	BJD
$P$	$0.127037 \pm 0.000001$	d
$i$	$90_{-0.3}^{+0.0}$	$^\circ$
$q$	$0.375 \pm 0.003$	
$a$	$0.921 \pm 0.018$	$R_\odot$
sdB Properties		
$M_{\text{sdB}}$	$0.47 \pm 0.03$	$M_\odot$
$R_{\text{sdB}}$	$0.199 \pm 0.004$	$R_\odot$
$T_{\text{eff}}$	$26100 \pm 400$	K
$\log(g)$	$5.50 \pm 0.07$	
$\log(y)$	$-2.32 \pm 0.10$	
$K_{\text{sdB}}$	$100.0 \pm 2.0$	$\text{km s}^{-1}$
dM Properties		
$M_{\text{dM}}$	$0.177 \pm 0.010$	$M_\odot$
$R_{\text{dM}}$	$0.222 \pm 0.004$	$R_\odot$
$T_{\text{eff}}$	$3000 \pm 500$	K

<sup>a</sup> From *Gaia* DR2 (Gaia Collaboration et al., 2018)<sup>b</sup> Epoch J2015.5.

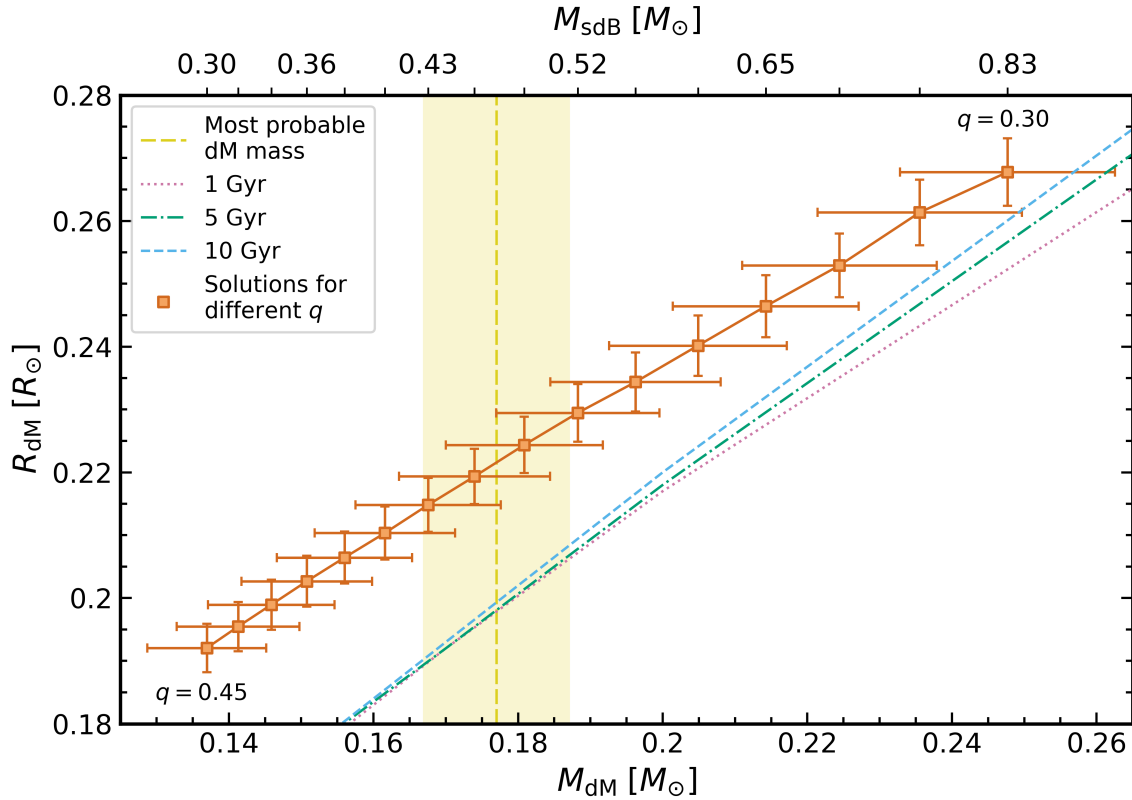


Figure 2.7: Mass–radius diagram for the dM companion illustrating the degeneracy in model solutions (orange squares). Theoretical mass–radius relations of low–mass stars (Baraffe et al., 2015) for a 1 Gyr (dashed blue line), 5 Gyr (dash–dotted green line), and 10 Gyr (dotted pink line) are also included. The vertical yellow line and shaded region represent the most probable dM mass and  $1\text{-}\sigma$  error, respectively, associated with the adopted  $0.47 M_{\odot}$  sdB solution.

typical period for HW Virs. The most probable solution is a sdB with a mass of the canonical mass  $M_{\text{sdb}} = 0.47 \pm 0.03 M_{\odot}$ . Additionally, our derived  $\log(g)$  and  $\log(y)$  values are also fairly typical of sdBs in HW Virs, but it is worth noting that our  $T_{\text{eff}}$  value is slightly lower than is typically found (for comparison, see Fig. 6 in Schaffenroth et al., 2019).

There are also noteworthy aspects of the system that are somewhat atypical among HW Virs, namely the derived companion mass and sdB velocity semi–amplitude. The companion mass is tied for the most massive in an HW Vir binary, along with that

of Konkoly J064029.1+385652.2 – also a deeply-eclipsing HW Vir-type (sdO+dM) binary. *Gaia* DR2 6097540197980557440 has an orbital period that is  $\sim 1.5$  hr shorter than Konkoly J064029.1+385652.2 and will one day evolve into a more rapid analog of Konkoly J064029.1+385652.2 when the sdB evolves into an sdO after the He in the core is exhausted and then, inevitably, into a WD. The sdB semi-amplitude we derive from the two sets of RV data make *Gaia* DR2 6097540197980557440 the fastest line-of-sight sdB velocity semi-amplitude reported to date for an HW Vir binary.

The most striking aspect of *Gaia* DR2 6097540197980557440 is the total eclipse of the sdB by its companion. Due to this system being relatively bright ( $G \sim 16.4$  mag), a large eclipse depth means future eclipse timing (O–C) analyses to search for changes in the orbital period ( $\dot{P}$ ) and even Rømer delay studies should be possible using telescopes with a variety of aperture sizes (e.g., Barlow et al., 2012). Additionally, *Gaia* DR2 6097540197980557440 will be observed at 2-min cadence in Sector 38 of TESS Cycle 3 through the Guest Investigator program (proposal #G03221), providing space-quality data spanning 27 d of observations. This is a unique opportunity to explore a relatively novel parameter space with one of the most accurate astrophysical clocks known (e.g., Kilkenney, 2014).

## 2.7 SUMMARY

We have presented photometric and spectroscopic observations of the first known deeply eclipsing sdB+dM binary, *Gaia* DR2 6097540197980557440. Other than the remarkably striking nature of the eclipse, the system is a rather typical sdB+dM system. We find an orbital period of  $P = 0.127037$  d and an sdB velocity semi-amplitude of  $K_{\text{sdB}} = 100.0 \text{ km s}^{-1}$  which combined with the most probable light curve solution yields masses of  $M_{\text{sdB}} = 0.47 M_{\odot}$  and  $M_{\text{dM}} = 0.18 M_{\odot}$ , respectively. This gives a radius of  $R_{\text{dM}} = 0.222 R_{\odot}$  for the companion, which is slightly inflated relative

to theoretical mass–radius relationships of low-mass main sequence stars. *Gaia* DR2 6097540197980557440 represents the first HW Vir solved as part of the EREBOS project. Eventual solutions for the more than 100 new HW Vir binaries uncovered by EREBOS will help improve our understanding of the common envelope channel leading to sdBs, and help determine the effects nearby low-mass stellar and substellar objects can have on stars climbing the giant branch.

## 2.8 APPENDIX

Shown in Figures 2.8 and 2.9 are the corner plots for the SOAR/Goodman *B* and *R* light curve solutions, respectively, using the Python package `corner` (Foreman-Mackey, 2016) for visualization. Also, we give the full set of possible solutions from the light curve modeling in Table 2.3.

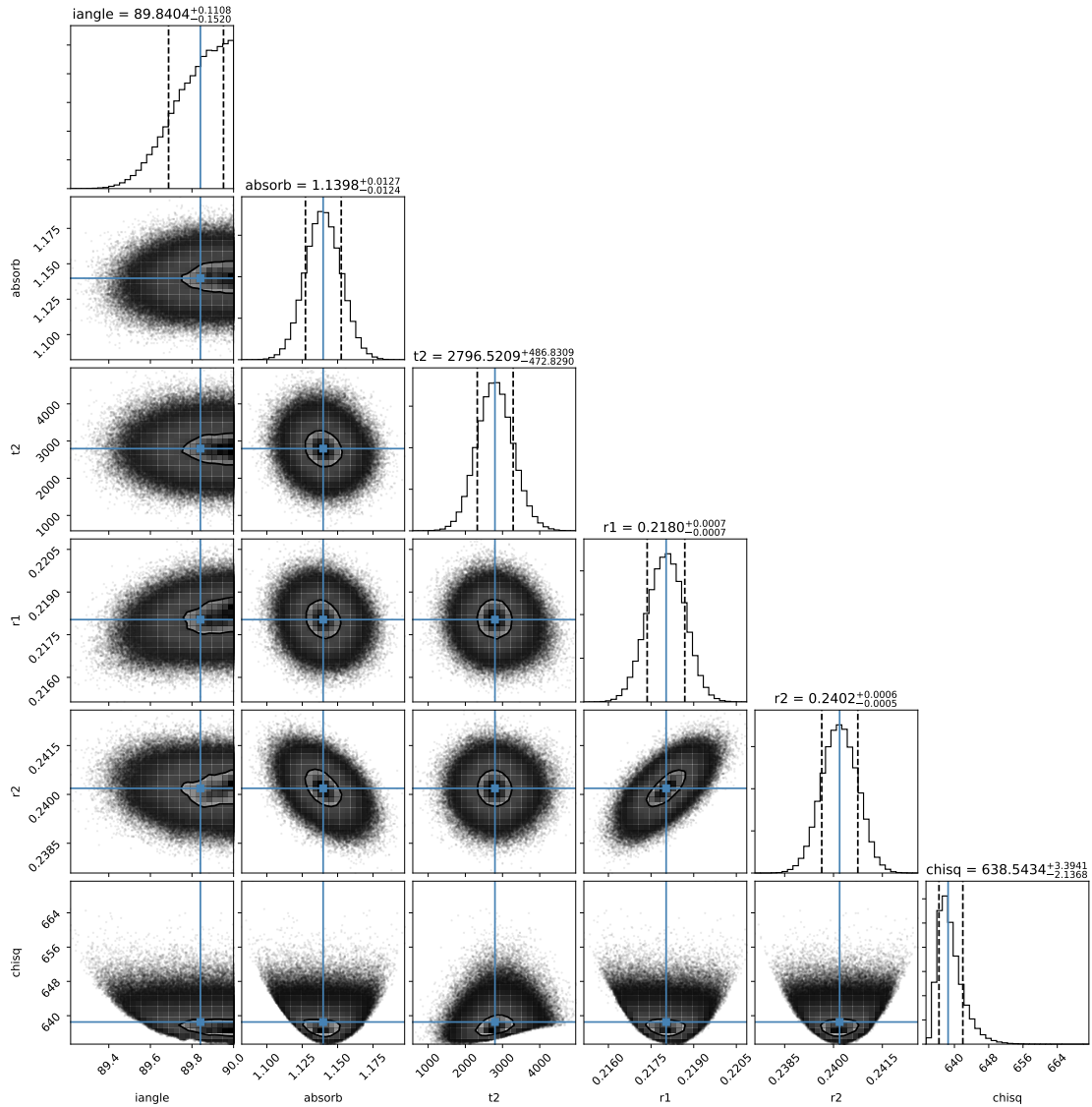


Figure 2.8: Corner plot of the most probable light curve solution for the SOAR/Goodman – *B* data. The quantities shown are the inclination angle (*iangl*), companion albedo (*absorb*), companion temperature (*t2*), primary radius (*r1*), companion radius (*r2*), and  $\chi^2$  (*chisq*).

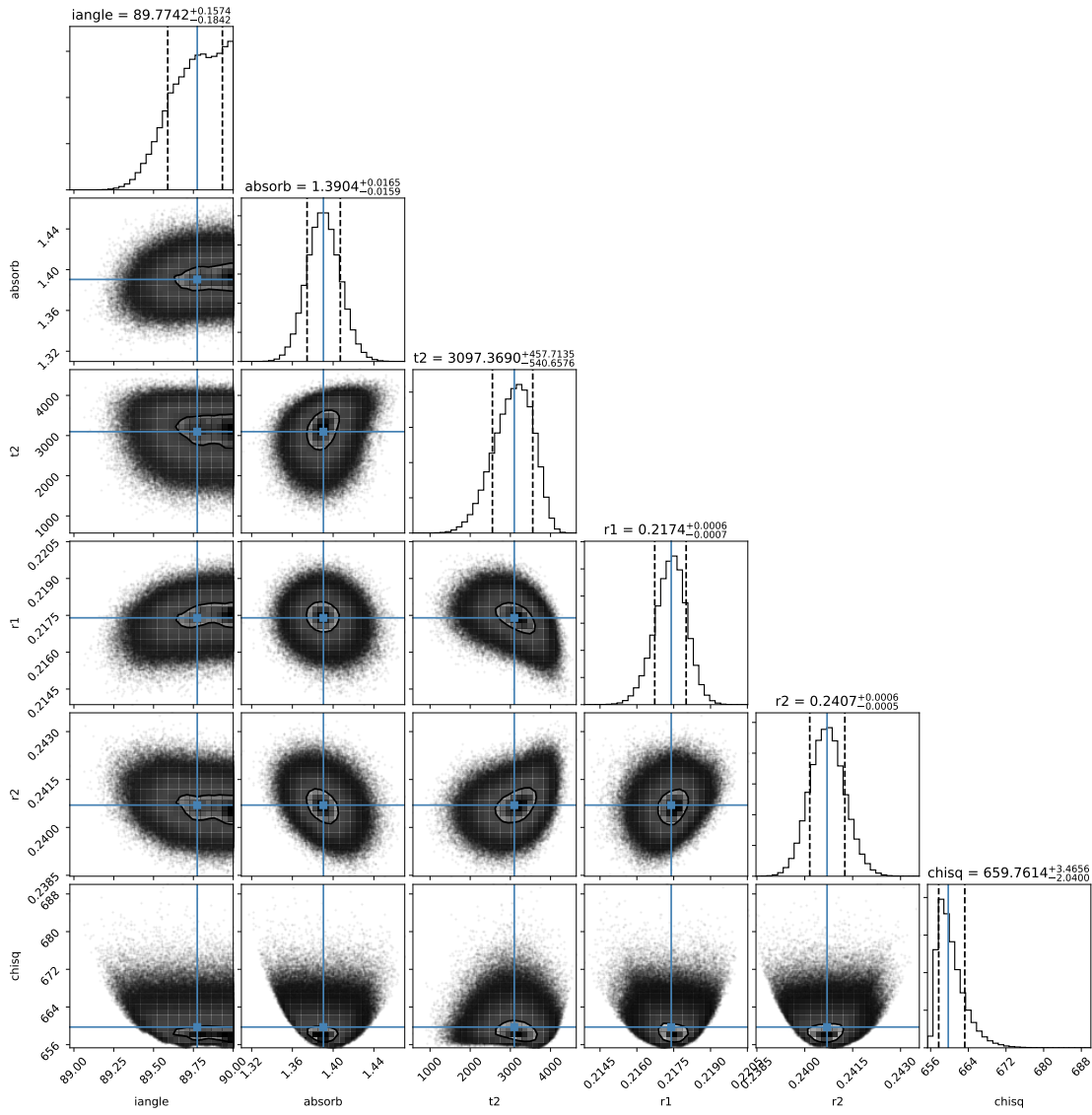


Figure 2.9: As in Figure 2.8 but for the SOAR/Goodman -  $R$  data.

Table 2.3: All of the possible light curve solutions output by LCURVE.

$q$	$a$ [ $R_{\odot}$ ]	$M_{\text{sdb}}$ [ $M_{\odot}$ ]	$M_{\text{dm}}$ [ $M_{\odot}$ ]	$R_{\text{sdb}}$ [ $R_{\odot}$ ]	$R_{\text{dm}}$ [ $R_{\odot}$ ]	$\log(g)$
0.30	$1.090 \pm 0.022$	$0.826 \pm 0.050$	$0.248 \pm 0.015$	$0.234 \pm 0.005$	$0.268 \pm 0.005$	$5.616 \pm 0.009$
0.31	$1.063 \pm 0.021$	$0.760 \pm 0.046$	$0.236 \pm 0.014$	$0.231 \pm 0.005$	$0.261 \pm 0.005$	$5.591 \pm 0.009$
0.32	$1.038 \pm 0.021$	$0.701 \pm 0.042$	$0.224 \pm 0.013$	$0.224 \pm 0.004$	$0.253 \pm 0.005$	$5.585 \pm 0.009$
0.33	$1.014 \pm 0.020$	$0.649 \pm 0.039$	$0.214 \pm 0.013$	$0.219 \pm 0.004$	$0.246 \pm 0.005$	$5.571 \pm 0.009$
0.34	$0.992 \pm 0.020$	$0.603 \pm 0.036$	$0.205 \pm 0.012$	$0.214 \pm 0.004$	$0.240 \pm 0.005$	$5.558 \pm 0.009$
0.35	$0.971 \pm 0.019$	$0.561 \pm 0.034$	$0.196 \pm 0.012$	$0.209 \pm 0.004$	$0.234 \pm 0.005$	$5.547 \pm 0.009$
0.36	$0.951 \pm 0.019$	$0.523 \pm 0.031$	$0.188 \pm 0.011$	$0.205 \pm 0.004$	$0.229 \pm 0.005$	$5.531 \pm 0.009$
0.37	$0.932 \pm 0.019$	$0.489 \pm 0.029$	$0.181 \pm 0.011$	$0.201 \pm 0.004$	$0.224 \pm 0.004$	$5.521 \pm 0.009$
0.38 <sup>†</sup>	$0.914 \pm 0.018$	$0.458 \pm 0.027$	$0.174 \pm 0.010$	$0.197 \pm 0.004$	$0.219 \pm 0.004$	$5.509 \pm 0.009$
0.39	$0.897 \pm 0.018$	$0.430 \pm 0.026$	$0.168 \pm 0.010$	$0.194 \pm 0.004$	$0.215 \pm 0.004$	$5.497 \pm 0.009$
0.40	$0.881 \pm 0.018$	$0.404 \pm 0.024$	$0.162 \pm 0.010$	$0.190 \pm 0.004$	$0.210 \pm 0.004$	$5.486 \pm 0.009$
0.41	$0.865 \pm 0.017$	$0.380 \pm 0.023$	$0.156 \pm 0.009$	$0.187 \pm 0.004$	$0.206 \pm 0.004$	$5.473 \pm 0.009$
0.42	$0.851 \pm 0.017$	$0.359 \pm 0.022$	$0.151 \pm 0.009$	$0.184 \pm 0.004$	$0.203 \pm 0.004$	$5.464 \pm 0.009$
0.43	$0.837 \pm 0.017$	$0.339 \pm 0.020$	$0.146 \pm 0.009$	$0.181 \pm 0.004$	$0.199 \pm 0.004$	$5.453 \pm 0.009$
0.44	$0.824 \pm 0.016$	$0.321 \pm 0.019$	$0.141 \pm 0.008$	$0.178 \pm 0.004$	$0.195 \pm 0.004$	$5.443 \pm 0.009$
0.45	$0.811 \pm 0.016$	$0.304 \pm 0.018$	$0.137 \pm 0.008$	$0.175 \pm 0.004$	$0.192 \pm 0.004$	$5.433 \pm 0.009$

<sup>†</sup> Most probable solution as outlined in the text



## CHAPTER 3

# ANALYSIS OF PREVIOUSLY CLASSIFIED WHITE DWARF-MAIN SEQUENCE BINARIES

This chapter was originally published as Corcoran et al. (2021b).

### 3.1 INTRODUCTION

White dwarf stars are the endpoint of stellar evolution for almost every main sequence star. Because most main sequence stars exist in binary systems (Duquennoy & Mayor, 1991; Raghavan et al., 2010; Yuan et al., 2015), it is common for the more massive star to evolve into a white dwarf, leading to a detached white dwarf-main sequence (WDMS) binary. The way in which the more massive star evolves is dictated by its separation from the progenitor binary, but there are two main formation scenarios followed by these systems. For a majority ( $\sim 75\%$ ) the separation is sufficient for the stars to evolve independently of one another, resulting in a wide binary (Willems & Kolb, 2004). The remaining fraction ( $\sim 25\%$ ) of systems can

undergo a stage of common envelope (CE) evolution, which causes the orbit to shrink significantly. Orbital energy can then be deposited into the envelope, which is ejected from the system, leaving behind a close, post-CE (PCE) binary (Webbink, 2008).

The two populations of WDMS binaries also yield a bimodal distribution in their orbital periods. This was shown in population synthesis studies (e.g., Willems & Kolb, 2004; Camacho et al., 2014; Cojocaru et al., 2017), which predict that wide WDMS binaries should have orbital periods of  $P > 100$  days. For instance, Farihi et al. (2010), using high-resolution imaging of 90 white dwarfs with known or suspected low-mass stellar and substellar companions, confirmed observationally that these systems exhibit a bimodal distribution in projected separation; further, they predict that all spatially unresolved, low-mass stellar and substellar companions in their survey will be found to be in short-period orbits. Indeed, observations of close PCE WDMS binaries show a distribution peaking at  $\sim 8$  hours (Miszalski et al., 2009; Nebot Gómez-Morán et al., 2011). It is worth noting, however, that five self-lensing PCE WDMS binaries with early-type companions and larger than typical separations have been found, and four of these have orbital periods of  $P > 400$  days (Kawahara et al., 2018; Masuda et al., 2019). While still PCE WDMS binaries, these may represent a population with a distinct formation pathway from the typical, more-compact PCE systems.

Apart from the normal migration from intermediate to short periods occurring in the course of normal CE evolution, PCE systems can evolve to even shorter orbital periods through angular momentum loss due to magnetic braking and/or gravitational wave emission. As is outlined in Ren et al. (2018) and references therein, it is possible for the PCE system to undergo a second CE stage, eventually producing double-degenerate WDs, cataclysmic variables, or super-soft X-ray sources. However, a complete understanding of the variety of these late evolutionary pathways must rest on a better foundational picture of the CE phase, which itself is still relatively

poorly understood (e.g., Ivanova et al., 2013). To guide these theoretical studies, more well-characterized systems at all phases of CE and PCE evolution are needed to place firm observational constraints. However, identifying systems in the CE phase is challenging, and most efforts are pointed at categorizing and characterizing PCE systems, which are then used to infer the parameters (e.g., envelope ejection efficiencies, angular momentum loss, envelope binding energy) of the more “hidden” CE phase (e.g., Ivanova et al., 2013). Of the different kinds of PCE systems (e.g., hot subdwarf B stars, extremely low mass white dwarfs, etc.), PCE WDMS are arguably the most common. Thus, PCE WDMS systems can play a crucial role in the study of CE evolution (Zorotovic et al., 2011), and are fundamental tools for understanding the range of astrophysically interesting endpoints of that evolution — e.g., from Type Ia supernovae to gravitational wave sources (e.g., Toloza et al., 2019).

Significant progress has been made in recent years to identify WDMS binaries using large area spectroscopic sky surveys at optical wavelengths, such as the Sloan Digital Sky Survey (SDSS; York et al., 2000; Stoughton et al., 2002) and the Large sky Area Multi-Object fiber Spectroscopic Telescope (LAMOST) survey (Zhao et al., 2012). These systems are identified in the optical through a variety of different methods, such as through  $\chi^2$ -fits of WDMS template spectra covering a vast range of temperatures, gravities, and companion spectral types (see Rebassa-Mansergas et al., 2010), through application of a wavelet transform (Chui, 1992) that efficiently identifies WDMS spectral features (see Ren et al., 2014), and through color-color cuts such as those in Rebassa-Mansergas et al. (2013). Presently, the most up-to-date catalog of spectroscopically-confirmed WDMS systems identified using SDSS, that by Rebassa-Mansergas et al. (2016a), contains 3294 WDMS binaries. The photometrically selected catalog of WDMS candidates identified using SDSS from Rebassa-Mansergas et al. (2013) contains 3419 systems. Meanwhile, Ren et al. (2018) created

a catalog with an additional 876 WDMS binaries identified using LAMOST spectra, 793 of which are claimed to be genuine WDMS systems. From these and other works (such as the White Dwarf Binary Pathways Survey — Parsons et al. 2016; Rebassa-Mansergas et al. 2017), the total number of systems classified as PCE WDMS binaries stands at  $\sim 300$  systems, while only  $\sim 120$  of these have derived orbital periods.

Fortunately, that number can be increased through a serendipitous channel. The Apache Point Observatory Galactic Evolution Experiment (APOGEE; Majewski et al., 2017) is a high resolution ( $R \sim 22,500$ ) infrared ( $1.5 - 1.7 \mu\text{m}$ ) spectroscopic survey that primarily targets red giant stars to study stellar populations across the Milky Way. However, because of the simple, photometrically-based selection criteria used for APOGEE targeting (Zasowski et al., 2013, 2017), some WDMS systems have received APOGEE observations by chance. Because of APOGEE’s multi-epoch observing strategy, most of these systems have high-quality time series radial velocity (RV) information for at least three, and, in some cases, as many as 50 “visits” (i.e., epochs). For systems with 6 or more visits, these data can be used to constrain or derive orbital parameters for these binary systems.

Here we present the 45 systems previously classified as WDMS binaries or candidate WDMS binaries via optical SDSS and LAMOST studies that have also been observed by APOGEE as of November 2019. Although this is a relatively small subsample drawn from these optical catalogs, the high quality APOGEE data — which include not only time series RVs, but also the spectroscopically-derived stellar atmospheric parameters and chemistry of the primaries — not only permit some glimpses into various sources of contamination in these previous, optical WDMS catalogs, but also contribute to the small, but growing census of WDMS systems having detailed characterization of their individual stellar constituents and orbital geometries. In particular, of the 21 systems that are confirmed here using APOGEE stellar parameters

to have MS primaries, twelve have sufficient RV visit information (6+ visits) from APOGEE to allow us to derive, or place limits on, the Keplerian orbital parameters. The remaining nine systems have more than two visits, which allows us to attempt to place limits on the orbital parameters. This pilot APOGEE assessment of the specific set of previously known WDMS systems also lends insights into the potential of the greater APOGEE database for not only the identification of previously unknown WDMS and PCE binaries, but to contribute in a major way to the relatively small number of such systems having well characterized system architectures.

## 3.2 THE APOGEE SURVEY

The SDSS-III APOGEE (Majewski et al., 2017) and SDSS-IV (Blanton et al., 2017) APOGEE-2 (Majewski et al., in prep.) surveys are now in their ninth year of observations with the 2.5-m Sloan Telescope (Gunn et al., 2006) at Apache Point Observatory in the Northern Hemisphere and their third year of observations with the 2.5-m du Pont Telescope at Las Campanas Observatory in the Southern Hemisphere. The combined survey databases now encompass more than 2 million spectra of nearly 600,000 distinct stars. The vast majority of APOGEE targets receive at least three visits, to build up signal-to-noise (S/N) and with the intent that RV variations can be used to identify stars in binary or higher multiplicity systems. Fainter stars will receive more visits as a means to build up signal sufficient to enable precision chemical abundance analysis on the combined spectra; however, the individual visits, even for faint stars, typically accumulate sufficient flux that good RVs can be derived for more extensive time series exploration. At the other extreme, a small fraction of APOGEE targets have only one visit for various reasons, but primarily because many of these were obtained as “bonus” targets through APOGEE-2 co-observing with the dark time SDSS-IV MaNGA project (Bundy et al., 2015).

The APOGEE reduction software (Nidever et al., 2015) derives RVs for each star using a two-step process. First, each visit spectrum is cross-correlated against a grid of synthetic spectra. This provides an “estimated RV” for each visit which is then used to correct the visit spectra to a common velocity needed for combination to a single, higher S/N spectrum for each source. The latter can then serve as an intermediate template against which the relative velocity of each visit spectrum can be rederived, and the whole process repeated in an iterative fashion to arrive at the best combined spectrum as well as a set of relative RVs. In principle, these well-matching, intermediate cross-correlation template spectra created from the combination of individual visits to a star should yield more precise RVs for that same star than if a synthetic template or the spectrum of another star were employed. Moreover, this method does not require fore-knowledge of the spectral type of the star to obtain high quality RVs. On the other hand, it is the case that for some stars (typically the fainter ones) this procedure does not improve on results obtained using synthetic cross-correlation templates, and so the reduction pipeline chooses the better result from the two methods at each iteration in the visit combination/relative RV determination stage of the data processing.

Due to the intrinsic resolution of the APOGEE spectrographs and the fact that they are bench-mounted in tightly controlled vacuum and cryogenic environments (Wilson et al., 2019), the median visit RV precision for APOGEE main survey stars is around  $100 \text{ m s}^{-1}$  (Nidever et al., 2015). This is better than is usually employed for the study of stellar binaries, and enables the detection of more subtle RV variability induced by more widely separated and/or lower mass companions (e.g., Troup et al., 2016; Price-Whelan et al., 2020).

After determination of the per-epoch RVs, the APOGEE reduction pipeline collates the spectra from all epochs after shifting them each to the rest frame velocity.

The final, coadded spectra are then run through the APOGEE Spectral Parameters and Chemical Abundances Pipeline (ASPCAP; García Pérez et al., 2016; Jönsson et al., 2020) to derive exquisite information on the effective temperatures ( $T_{\text{eff}}$ ), gravities ( $\log g$ ), and metallicities of each APOGEE target (e.g., Holtzman et al., 2015, 2018). Majewski et al. (2017) presents many example spectra of stars spanning large ranges in spectral type and metallicity to showcase the quality of APOGEE spectra, and the publicly available APOGEE spectra can be viewed along with their ASPCAP fits on a per-target basis via the SDSS website.<sup>1</sup> The ASPCAP results for the luminous primaries of the WDMS candidates presented here are included in Table 3.1 (see columns 6-8), which also gives the 2MASS names for the sources (column 1), the survey in which each system was first identified as a WDMS candidate (LAMOST or SDSS, column 2), the Gaia magnitude (column 3), and the 2MASS  $H$  magnitude and  $(J - K)$  color (columns 4 and 5, respectively). We use these data to make an initial global assessment of these 45 systems in Section 3.3, aided in part by ancillary information provided by previous studies. That ancillary information is summarized in the final column of Table 3.1.

### 3.3 GLOBAL ASSESSMENT OF THE PREVIOUSLY IDENTIFIED WDMS SYSTEMS

As is to be expected, we find here some fraction of contaminants among systems previously identified as WDMS candidates, based on optical spectroscopic and photometric surveys. In this section we identify some categories of contamination, made evident by exploration of the observed global properties of the systems in Table 3.1.

Figure 3.1 shows both the *Gaia*-based  $H$ -band absolute magnitude and the ASPCAP-

---

<sup>1</sup><https://dr16.sdss.org/infrared/spectrum/search>

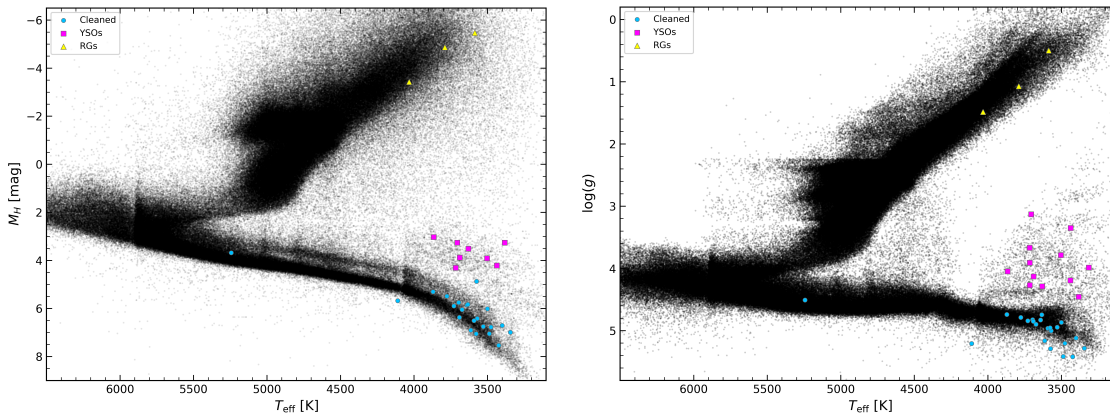


Figure 3.1: Confirmed or candidate WDMS systems shown against all of APOGEE. Note that not all of the 45 systems are shown due to either missing parallaxes (left) or ASPCAP parameters (right). We highlight in both plots the RG (yellow triangles) and YSO (magenta squares) contaminants as well as the remaining, cleaned sample with MS primaries (blue circles). *Left:* *Gaia*-based *H*-band absolute magnitude as a function of the ASPCAP  $T_{\text{eff}}$ . *Right:* Kiel diagram with the ASPCAP  $\log(g)$  as a function of ASPCAP  $T_{\text{eff}}$ .

based spectroscopic gravities  $\log g$  as a function of ASPCAP effective temperature,  $T_{\text{eff}}$ . The full sample of APOGEE DR16 stars are shown in black and the 45 WDMS candidates as the larger colored dots. The WDMS candidates cluster in three general locations in these observational planes. The majority of the candidates do indeed lie on the main sequence, as one would hope for WDMS candidates. Among those systems with MS primaries, the vast majority are at temperatures typical of M dwarfs; only one (2M18454771+4431148) is at a hotter temperature ( $T_{\text{eff}} \sim 5240$  K), a temperature typical of a late G type star. All of these WDMS candidates on the lower MS have spectroscopically-derived metallicities that are near-solar (within 0.4 dex), consistent with their locations in Figure 3.1.

However, one of the systems in the “lower MS” group, (2M14244053+4929580), actually lies *below* the MS at  $T_{\text{eff}} \sim 4110$  K in both panels of Figure 3.1. This “subdwarf” location is consistent with the ASPCAP derived metallicity for this star

( $[\text{Fe}/\text{H}] = -1.42$ ), which shows it to be a rare (see Figure 3.8, below), metal-poor WDMS candidate. This metallicity is near the mean value of the Galactic halo (Beers et al., 2005), suggesting that this WDMS system belongs to this population. Nevertheless, surprisingly, an analysis of the kinematics of this star (Sec. 3.6) shows this binary to actually have a disk-like orbit.

Yet another star in our sample, 2M05303840–0525436, has a derived ASPCAP metallicity that is relatively low ( $[\text{Fe}/\text{H}] = -0.8$ ), but in this case we believe that this metallicity is likely incorrect, because this star is likely a pre-main sequence, young stellar object (YSO; see below). In addition, the spectrum of this star has been flagged by ASPCAP as having potential problems due to cross-talk from a bright neighboring spectrum, as well as landing in parts of the APOGEE detectors that have been identified to have problems with persistence (see Wilson et al., 2019, for an explanation). We discuss the subdwarf 2M14244053+4929580 and the overall metallicity distribution function of the cleaned WDMS sample in more detail in Section 3.6.

Three other stars in Table 3.1 (2M01090044+5203369, 2M19202987+4000013, and 2M22145972–0820200) have both absolute magnitudes and spectroscopically-derived gravities indicating that the primaries are, in fact, on the red giant branch. LAMOST had classified 2M01090044+5203369 and 2M22145972–0820200 as confirmed WDMS binaries, while 2M19202987+4000013 was reported as a candidate WDMS system. Recently, Frasca et al. (2016), as part of their analysis of the stellar parameters of targets in the *Kepler* field, also identified the system 2M19202987+4000013 to have a red giant primary. These three systems, while not WDMS, are still potentially interesting as potential symbiotic star candidates (e.g., Lewis et al., 2020).

A third group of systems that can be seen in Figure 3.1 are those with low  $T_{\text{eff}}$ , but both higher luminosities and lower surface gravities as compared to normal MS stars

of the same temperature. The properties of these systems are consistent with young stellar objects (YSOs). All twelve of these stars are located either in the youngest (1–3 Myr) regions of the Orion Complex (Kounkel et al., 2018), or in NGC 2264, which is another  $\sim 3$  Myr massive cluster (Dahm, 2008). Moreover, all twelve of these systems are designated as YSOs in the SIMBAD database (Wenger et al., 2000). Two additional systems in Table 3.1 that do not have derived ASPCAP parameters (due to insufficient S/N or other problems) and therefore do not appear in Figure 3.1, 2M05343005–0449506 and 2M06402564+0959597, are also identified in SIMBAD to be YSOs. Given their extreme youth, it is very unlikely that any of these systems have white dwarf companions.

All fourteen of the YSO contaminants were found in the catalog derived from SDSS photometric data, for which the WDMS candidates were selected on the basis of several color–color selections. However, none of these stars are among those SDSS candidates having previous spectroscopic confirmation by Rebassa-Mansergas et al. (2016a). Clearly the original optical photometric selection used to select WDMS candidates is also sensitive to YSOs, as evidenced by their prominence in our sample. The main signature of accreting young stars (i.e., Classical T Tauri stars) is strong  $H\alpha$  emission, with a 10% width of the line in excess of  $200 \text{ km s}^{-1}$ , and with equivalent widths that can reach as high as  $200 \text{ \AA}$ . Weak-Lined T Tauri stars (WTTS, i.e., YSOs that have already stopped accreting and likely have depleted their protoplanetary disks) also can have an  $H\alpha$  equivalent width as high as  $40 \text{ \AA}$  in late M stars (e.g., White & Basri, 2003). Apparently such strong Balmer emission, particularly  $H\alpha$ , confounds the various automated WDMS candidate finding algorithms previously employed.

Meanwhile, at shorter wavelengths, an excess of flux in YSOs can also be a signature of magnetospheric accretion (e.g., Calvet & Gullbring, 1998; Ingleby et al.,

2013), produced by the accretion shocks heating up small spots on the photosphere to temperatures as high as 90,000 K immediately after the shock. Even WTTS systems have NUV luminosities three times higher than what is observed for MS stars of the same spectral type. Given their propensity for UV emission, it is understandable how photometric selection criteria that search for WDMS systems might also recover some YSOs. Ultimately, it seems that a check of other WDMS candidate properties, such as detection of Li I absorption, placement on the HR diagram, and/or a Galactic position consistent with nearby star forming regions, is needed to identify YSO contaminants from these optically-based WDMS candidate catalogs. It is also worth noting that while WDMS are multiple systems by definition, comparable photometric or spectroscopic signals could originate from single YSOs without any binary companions.

That about a third of our sample of WDMS candidates turn out to be YSOs may seem surprising, but this should not be interpreted as implying that the SDSS-based (or even the LAMOST-based) WDMS catalog is similarly fractionally contaminated by YSOs. Both the SDSS-based WDMS catalog as well as the APOGEE survey have numerous strong selection biases that complicate interpretation of contamination fractions. For example, the SDSS survey by and large avoided observations of the Galactic midplane, where YSOs are most concentrated. On the other hand, APOGEE observations are highly biased *towards* the Galactic plane, and, to further amplify that bias toward finding YSOs, the APOGEE survey included a specific focus on star forming regions as part of its targeting, in particular through several APOGEE Ancillary Science projects (Zasowski et al., 2013, 2017; Cottaar et al., 2014; Cottle et al., 2018). These competing biases make it difficult to interpret the 27% YSO contamination of our initial sample, except as a strong alert to this false positive class.

A similar comment may be made regarding the fraction of misidentified giant stars among the WDMS candidates: The  $\sim 6\%$  fraction of giant star systems in our sample, which all come from the LAMOST-based WDMS search, may be inflated by the strong focus on giant stars in APOGEE targeting. Again, the primary relevant conclusion to be drawn is that the prior WDMS candidate catalogs contain some contamination by misidentified systems with red giant primaries.

Table 3.1: General information on the 45 WDMS systems/candidates observed by APOGEE.

APOGEE ID	Source Survey	$G^a$ [mag]	$H^b$ [mag]	$(J - K)^b$ [mag]	$T_{\text{eff}}^b$ [K]	$\log(g)^b$ [cgs]	[Fe/H] <sup>b</sup>	Notes <sup>c</sup>
2M01090044+5203369	LAMOST	11.692	8.290±0.018	1.098±0.032	4033±65	1.486±0.047	0.254±0.007	RG
2M01575656-0244460	SDSS <sup>d</sup>	15.041	12.103±0.024	0.829±0.035	3871±86	4.739±0.103	0.114±0.016	
2M03160020+0009462	LAMOST	15.363	12.069±0.024	0.797±0.037	3574±77	5.290±0.111	0.017±0.019	
2M03452349+2451029	LAMOST <sup>d</sup>	14.476	11.201±0.030	0.880±0.034	3776±64	4.789±0.110	0.048±0.011	
2M04322373+1745026	LAMOST	13.362	10.161±0.019	0.840±0.027	3344±64	5.283±0.110	0.187±0.017	
2M05242983+0023460	SDSS <sup>d</sup>	15.836	12.016±0.023	0.974±0.035	3439±67	4.193±0.122	-0.204±0.020	TTau
2M05285461+0305035	SDSS <sup>d</sup>	14.681	11.141±0.026	0.960±0.038	3630±62	4.288±0.109	0.123±0.012	RSCVn
2M05303840-0525436	SDSS <sup>d</sup>	14.818	11.398±0.024	0.991±0.031	3706±84	3.130±0.057	-0.813±0.030	Orion V
2M05321483-0620547	SDSS <sup>d</sup>	15.038	11.778±0.026	0.923±0.033	3503±76	3.785±0.044	-0.230±0.023	Orion V
2M05325045-0035422	SDSS <sup>d</sup>	15.736	12.057±0.022	0.975±0.036	3383±66	4.456±0.124	-0.211±0.021	YSO
2M05343005-0449506	SDSS <sup>d</sup>	14.427	11.265±0.032	1.042±0.031				Orion V
2M05355349-0123044	SDSS <sup>d</sup>	16.066	11.894±0.031	1.217±0.034	3313±63	3.986±0.044	-0.261±0.022	YSO
2M05361475-0613169	SDSS <sup>d</sup>	15.106	11.737±0.032	0.973±0.028	3689±73	4.130±0.118	-0.185±0.017	Orion V
2M05393524-0436145	SDSS <sup>d</sup>	15.867	12.148±0.024	1.244±0.033	3437±70	3.350±0.047	-0.476±0.024	YSO
2M06393441+0954512	SDSS <sup>d</sup>	15.585	12.215±0.023	1.059±0.033	3715±78	3.910±0.047	-0.214±0.018	Orion V
2M06402564+0959597	SDSS <sup>d</sup>	17.083	13.130±0.026	1.275±0.042				TTau
2M06404600+0917582	SDSS <sup>d</sup>	15.999	12.701±0.026	0.881±0.042	3714±77	4.267±0.112	-0.017±0.017	TTau
2M06411837+0939411	SDSS <sup>d</sup>	16.031	12.649±0.025	0.947±0.040	3716±88	3.669±0.045	-0.204±0.023	Orion V
2M06412562+0934429	SDSS <sup>d</sup>	15.521	12.391±0.022	0.960±0.036	3866±84	4.048±0.116	-0.204±0.018	TTau
2M08094855+3221223	SDSS <sup>d</sup>	16.604	13.085±0.020	0.922±0.035	3529±68	4.946±0.113	-0.016±0.017	
2M08424235+5128575	SDSS <sup>d</sup>	13.937	10.399±0.027	0.885±0.030				
2M08531787+1147595	SDSS/LAMOST	14.454	11.544±0.028	0.743±0.029				
2M09463250+3903015	SDSS <sup>d</sup>	15.155	11.948±0.022	0.859±0.030	3696±73	4.825±0.107	0.091±0.015	
2M10243847+1624582	SDSS	17.822	14.454±0.054	0.771±0.068	3400±78	5.119±0.113	0.063±0.024	
2M10552625+4729228	SDSS	16.664	13.227±0.027	0.881±0.042	3500±74	4.868±0.107	0.169±0.018	
2M11241545+4558412	SDSS <sup>d</sup>	14.603	11.396±0.032	0.863±0.030	3691±71	4.849±0.110	0.025±0.014	
2M11463394+0055104	SDSS <sup>d</sup> /LAMOST <sup>d</sup>	16.741	13.397±0.023	0.924±0.042	3476±76	5.204±0.116	-0.045±0.022	
2M12154411+5231013	LAMOST	12.581	9.340±0.027	0.946±0.030	3487±56	5.414±0.114	0.028±0.012	
2M12333939+1359439	SDSS <sup>d</sup> /LAMOST <sup>d</sup>	16.679	13.486±0.030	0.922±0.036				
2M12423245-0646077	SDSS	16.065	12.968±0.027	0.915±0.037	3728±78	4.842±0.112	-0.059±0.017	
2M13054173+3037005	SDSS <sup>d</sup>	16.237	12.761±0.022	0.803±0.033	3424±72	5.420±0.119	-0.113±0.022	
2M13090450+1411351	SDSS <sup>d</sup> /LAMOST <sup>d</sup>	15.308	12.229±0.023	0.845±0.033	3570±73	5.003±0.117	-0.142±0.019	
2M13115337+1549147	SDSS <sup>d</sup>	16.825	13.353±0.031	0.927±0.048				
2M13463968-0031549	SDSS <sup>d</sup>	16.427	13.382±0.035	0.823±0.046				
2M14244053+4929580	SDSS	15.694	13.542±0.031	0.631±0.052	4111±111	5.208±0.160	-1.415±0.038	
2M14544500+4626456	LAMOST <sup>d</sup>	14.531	11.278±0.032	0.925±0.035	3673±71	4.898±0.106	0.148±0.014	
2M14551261+3810342	LAMOST	14.400	11.279±0.022	0.802±0.029	3641±84	4.829±0.122	-0.308±0.024	
2M15041191+3658150	LAMOST	17.034	13.722±0.036	0.873±0.043	3592±71	4.962±0.117	-0.130±0.017	
2M15104562+4048271	SDSS/LAMOST	14.671	11.374±0.019	0.796±0.028	3577±78	4.954±0.127	-0.372±0.023	
2M15150334+3628203	SDSS <sup>d</sup>	14.941	11.652±0.022	0.906±0.029	3634±65	4.744±0.104	0.240±0.012	
2M18454771+4431148	LAMOST	13.742	12.075±0.020	0.445±0.025	5243±131	4.509±0.085	0.093±0.012	
2M19202987+4000013	LAMOST <sup>d</sup>	12.856	9.345±0.021	1.084±0.025	3789±61	1.071±0.046	0.135±0.009	RG
2M19274650+3841111	LAMOST	12.006	7.951±0.016	1.208±0.038	3586±60	0.497±0.050	-0.326±0.013	RG
2M22145972-0820200	SDSS	17.427	14.189±0.043	0.894±0.069				
2M22200576-0418445	LAMOST	15.387	12.405±0.023	0.792±0.026	3613±86	5.161±0.122	-0.306±0.026	

<sup>a</sup> From Gaia Collaboration et al. (2018)

<sup>b</sup> From APOGEE

<sup>c</sup> Descriptions follow the condensed object descriptions from SIMBAD

<sup>d</sup> SDSS photometric candidate or LAMOST spectroscopic candidate

### 3.4 ANALYSIS OF SYSTEM ARCHITECTURES

After removing the YSO and red giant systems from the initial set of 45 previously identified WDMS systems, we are left with 28 remaining as candidate WDMS systems. Of these, 21 have two or more epochs of RV data, which allow either limits on or solutions to the system orbital parameters.

#### 3.4.1 *The Joker* Orbital Analysis of the Radial Velocities

Analysis of the multi-epoch RVs was performed using *The Joker* (Price-Whelan et al., 2017, 2020), a custom Monte Carlo sampler that uses a given set of input RV measurements to produce independent posterior samples in Keplerian orbital parameters. In particular, the code was designed to excel at fitting orbits for targets with sparse RV data and/or low S/N RV measurements. Here we provide a brief description of the fitting procedure for clarity, but a more thorough and technical prescription can be found in Price-Whelan et al. (2017, 2020). First,  $2^{24}$  samples are drawn from a prior probability density function covering the full Keplerian orbit parameter space, allowing rejection sampling over a dense set of potential solutions. For systems that have a large number of surviving samples (in this work, 256 samples) that are not unimodal, we recompute the rejection sampling with 512 requested samples in an attempt to discover groupings of possible solutions in the period distribution and period versus eccentricity diagram that can place limits on the orbital parameters (see Sec. 3.5.6 and 3.5.7 for further details). If the number of surviving samples is fewer than 256 samples, however, these surviving samples are used to initialize a Markov chain Monte Carlo (MCMC) run. This procedure typically returns a unimodal set of samples that represent the best fitting solution for a system.

To limit our analysis to only RVs derived from high-quality spectra, we remove

any visit-level APOGEE data that have the following `STARFLAGS`<sup>2</sup> set: `LOW_SNR` (visit-S/N < 5), `VERY_BRIGHT_NEIGHBOR` (indicates that a star with a spectrum adjacent to that of the target star on the spectrograph detector is more than 100 times brighter and therefore a source of potential contaminating flux), `PERSIST_HIGH` (evidence that the spectrum crosses detector pixels that show super-persistence), `PERSIST_JUMP_POS`, or `PERSIST_JUMP_NEG` (the last two flags indicate an obvious and artificial positive or negative decrease, or “jump”, in spectral continuum in two of the spectrograph detectors — with one sampling from 1.585 to 1.644  $\mu\text{m}$  and the other from 1.514 to 1.581  $\mu\text{m}$ ). These flags correspond to bitmask values: 3, 4, 9, 12, 13.

Because the APOGEE visit-level RV uncertainties (`VRELERR` in the `allVisit` file) are known to be underestimated (e.g., Badenes et al., 2018), for the systems surviving the above target flag pruning we apply the expression presented in Lewis et al. (2022)

$$\sigma_{\text{RV}}^2 = (3.5(\text{VRELERR})^{1.2})^2 + (0.072 \text{ km s}^{-1})^2, \quad (3.1)$$

where  $\sigma_{\text{RV}}$  is the total, inflated visit velocity error for a given visit. This asymptotes to a 0.072  $\text{km s}^{-1}$  minimum for the visit-level RV uncertainties.

For systems with  $\gtrsim 8$  visits that are well distributed in orbital phase, *The Joker* generally converges to a single, unimodal period solution. This is because *The Joker* fits six orbital elements, i.e., has 6 degrees of freedom. Of the 21 WDMS binary candidates having at least two APOGEE RV visits, eight have at least eight visits, and thus are good candidates for full Keplerian orbit fitting with *The Joker*, although not all will return satisfactory solutions because of undetectable orbital amplitudes in the cases of wide binaries. The four systems with six or seven RV visits often converge to a single solution, but not universally. In cases where no single solution is

---

<sup>2</sup>[https://www.sdss.org/dr16/algorithms/bitmasks/#APOGEE\\_STARFLAG](https://www.sdss.org/dr16/algorithms/bitmasks/#APOGEE_STARFLAG)

reached (i.e., those with multimodal period solutions), only limits can be placed on the period of the system. This is typical for the nine systems with two to five visits.

In the end, we report full orbital solutions for five short period (relative to the APOGEE temporal baseline) systems. In all five cases, these are the first solutions ever presented for these systems, including RV variations that warrant a PCE classification. We discuss these five systems in more detail in Sections 3.5.1-3.5.5. For another seven systems that are sampled reasonably to very well by APOGEE (i.e.,  $\geq 6$  RV epochs) no good solution converges because the period of the WDMS binary may be longer than their APOGEE time series data; therefore we report them as “wide binary” systems and provide lower limits on the orbital period and the main sequence star velocity amplitude. These systems are discussed in Section 3.5.6. For an additional nine systems having 2-5 visits, we also provide upper and lower limits to the orbital period (Sec. 3.5.7), and among these are two well known PCE systems and two newly discovered systems that have RV variations warranting a PCE classification. A few of the WDMS systems observed by APOGEE are left with 1 or 0 useful visits after imposition of the quality cuts described in Section 3.4.1, and we briefly mention these in Section 3.5.8.

### 3.4.2 Estimating the Stellar Masses

Along with the orbital parameters provided by *The Joker*, we can estimate the primary star masses via the empirically-derived Torres et al. (2010) relation for main sequence stars:

$$\begin{aligned} \log M_{\star} = & a_1 + a_2X + a_3X^2 + a_4X^3 + a_5(\log g)^2 \\ & + a_6(\log g)^3 + a_7[\text{Fe}/\text{H}], \end{aligned} \tag{3.2}$$

which has a relatively small scatter ( $\sigma_{M_\star} = 0.064M_\star$ ) for stars down to  $\sim 0.5 M_\odot$ . Here,  $X = \log T_{\text{eff}} - 4.1$  and the coefficients,  $a_i$ , are given in Torres et al. (2010). For the systems with unimodal samples returned by *The Joker*, we additionally calculate the minimum masses of the secondary (i.e., the WD companions),  $m \sin i$  using the calculated primary masses. In Table 3.2, we report the masses for all the MS stars in our clean sample that have ASPCAP parameters, and we report the minimum masses of the WD stars and derived orbital parameters in systems with well-constrained orbital periods.

## 3.5 DESCRIPTIONS OF INDIVIDUAL SYSTEMS

### 3.5.1 2M10243847+1624582

High-quality APOGEE observations of the spectroscopically-confirmed WDMS system 2M10243847+1624582 exist for 28 epochs spanning just over a year, from 2015 February to 2016 February. APOGEE spectroscopic analysis reveals the cool ( $T_{\text{eff}} = 3400$  K) M dwarf primary to be approximately solar metallicity ( $[\text{Fe}/\text{H}] = +0.06$ ). The combined *The Joker* plus MCMC run returned a unimodal solution, and this best-fit solution is presented in Figure 3.2. With an RV semi-amplitude of  $146 \text{ km s}^{-1}$  and an orbital period of just over 12 hours, this system is fairly typical for a PCE WDMS system. Schreiber et al. (2010) identified this system as a PCE candidate, and our solution confirms this classification. The lower limit on the WD mass of  $m \sin i = 0.537 \pm 0.013 M_\odot$  is consistent with typical masses reported by both Rebassa-Mansergas et al. (2016a) for all SDSS systems and Ren et al. (2018) for all LAMOST systems. In this case, however, the mass derived from SDSS with combined atmospheric parameters and cooling track fitting is  $M_{WD} = 0.830 \pm 0.063 M_\odot$ , which is well above our derived mass limit, possibly indicating a slightly inclined orbit.

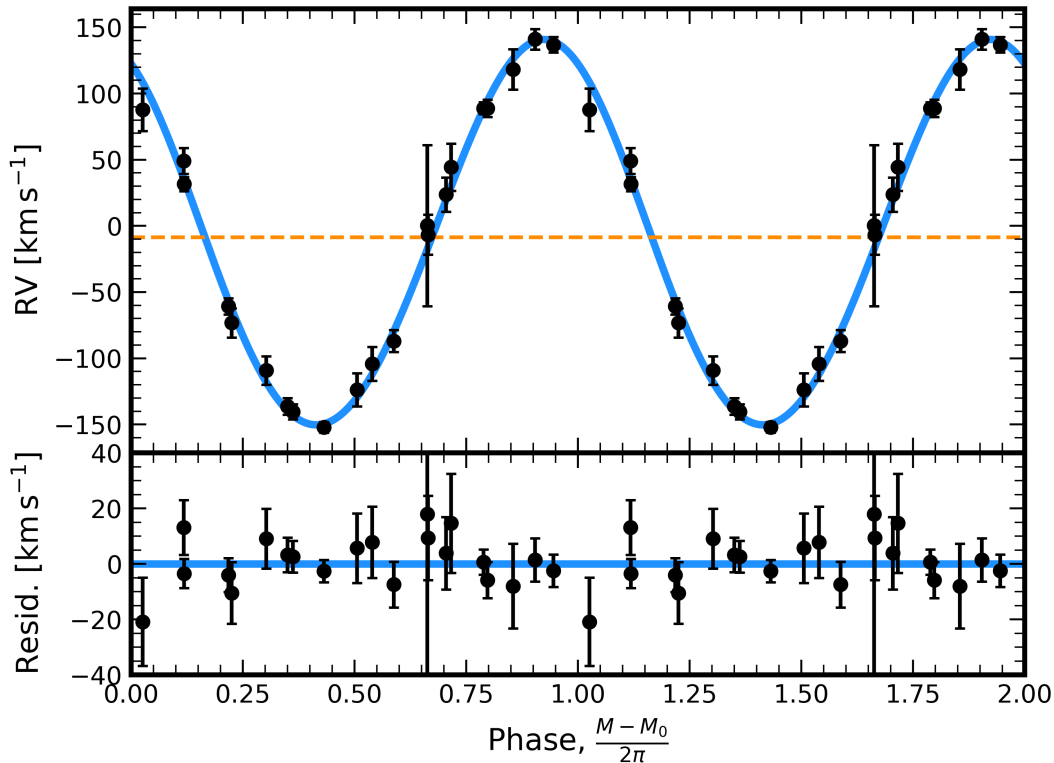


Figure 3.2: *Upper panel:* The best fitting RV curve derived from the orbital solution to the 28 phase-folded APOGEE RVs for the WDMS system 2M10243847+1624582. Two periods are shown for clarity. *Lower panel:* The residuals to the fit shown in the upper panel.

### 3.5.2 2M10552625+4729228

The WDMS system 2M10552625+4729228 was observed with high S/N eleven times over 277 days from 2017 May to 2018 February. APOGEE spectroscopic analysis again reveals a cool ( $T_{\text{eff}} = 3500$  K) M dwarf primary, this one with a super-solar metallicity ( $[\text{Fe}/\text{H}] = +0.17$ ). Our analysis with *The Joker* yields a unimodal solution to the RV variations of the M dwarf primary, shown in Figure 3.3. The solution reveals this binary to be another PCE system; with a derived period of a little more than 2 days, though slightly longer than the 8 hour average for PCE WDMS systems, the

system is still in a much shorter period orbit than the longest known for PCE binaries. Schreiber et al. (2010) also identified this system as a PCE candidate, and our solution confirms this classification. The lower limit on the WD mass of  $m \sin i = 0.476 \pm 0.009 M_{\odot}$  is similar to that of 2M10243847+1624582, which again could indicate a slightly inclined orbit since it is well below the SDSS mass of  $M_{WD} = 0.790 \pm 0.081 M_{\odot}$ . This value is, however, consistent with typical SDSS and LAMOST WD masses.

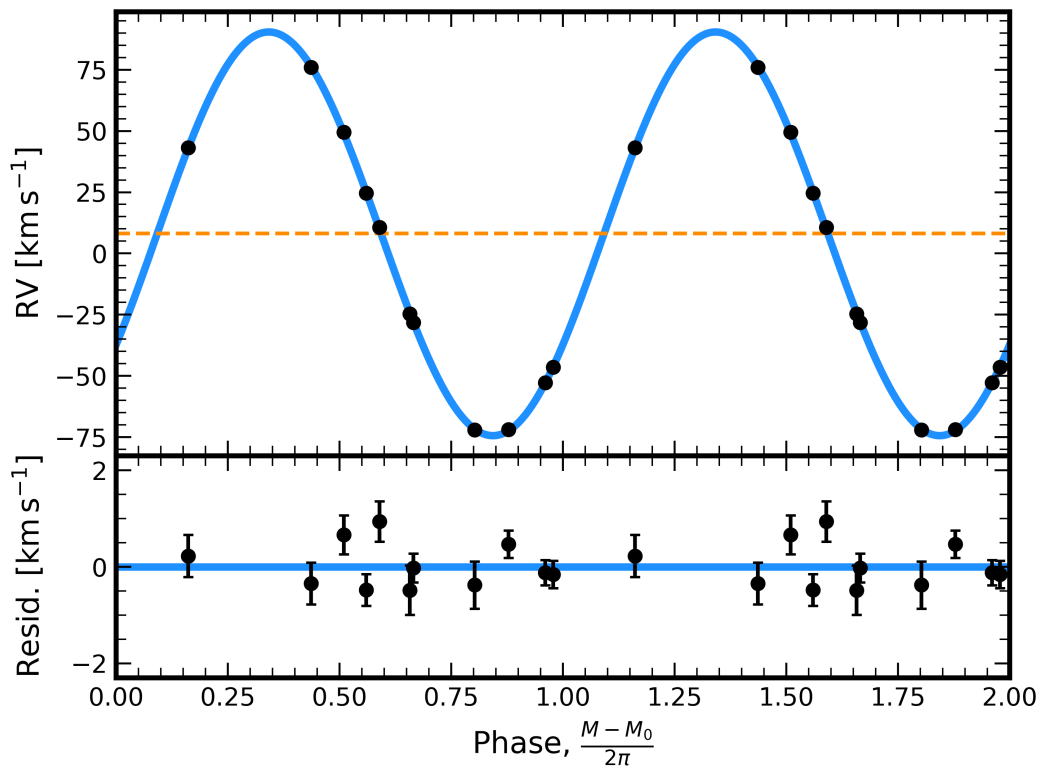


Figure 3.3: The same as Figure 3.2 but for the eleven APOGEE RV epochs for 2M10552625+4729228. The error bars are smaller than the plotted points in the upper panel.

### 3.5.3 2M11463394+0055104

The target 2M11463394+0055104, determined by APOGEE spectroscopic analysis to be another approximately solar metallicity M dwarf ( $[\text{Fe}/\text{H}]=-0.05$ ), received 33 high-quality visits spanning just over 4 years from 2012 February to 2016 March. With such extensive coverage, it is not surprising that a unimodal solution was achieved for this system; the best-fit solution is shown in Figure 3.4. A roughly 9 hour orbital period places this system just above the typical 8 hour period for PCE WDMS systems. LAMOST flagged this system as a candidate WDMS binary based on their spectra, and, combined with our derived orbital solution, we confirm this system to be another PCE WDMS binary. The derived lower limit to the WD mass of  $0.717 \pm 0.014 M_{\odot}$  places this companion near the upper end of the mass distributions reported by both SDSS and LAMOST. While this is not atypical nor the most massive WD by far, this larger mass is worth pointing out, since it is in contrast to the mass limits of the other systems with unimodal solutions.

### 3.5.4 2M13054173+3037005

This target received only six high-quality visits spanning just over a month from 2018 April 24 to 2018 May 31. To compensate for the smaller number of RV epochs, we decrease the number of degrees of freedom in the solution by setting the eccentricity of all attempted fits to  $e = 0$  (as we do not have sufficient data to prefer an eccentric orbit over a circular one at this time). We then performed runs with *The Joker* using a succession of minimum periods starting with 0.055, 0.1, 0.23, 0.3, 0.64, 0.73, and 1.1 days and a maximum period of 7.0 days; that maximum period was selected because the first four RVs collected looked like they formed a possible full orbital period of that length. After running *The Joker* on this system multiple times, it was evident that

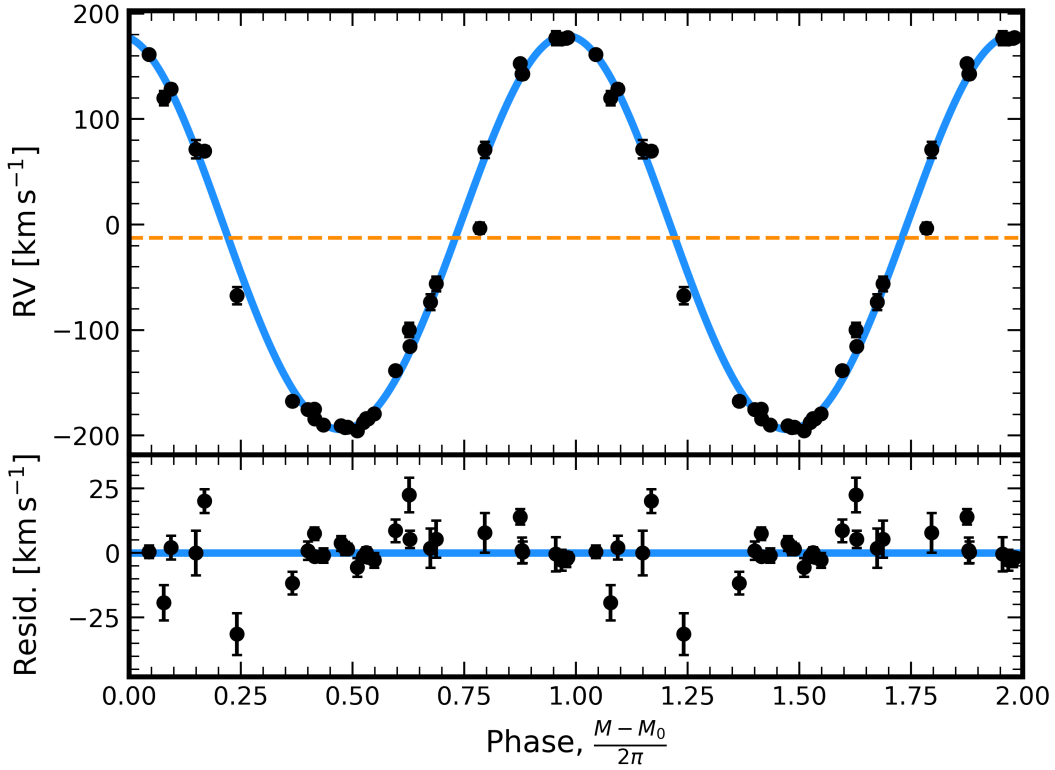


Figure 3.4: The same as Figure 3.3 but for the 33 APOGEE RV epochs for 2M11463394+0055104.

there were multiple solutions that fit the data even though any individual run could return a single solution depending on the specified minimum orbital periods. With only six data points, the phase coverage and RV spread ( $RV_{\max} - RV_{\min} = \Delta RV_{\max}$ , as in Table 3.2) for all solutions in one *The Joker* run of a given set lower period limit were inconsistent with one another, and not all of the runs returned realistic solutions. The solution we report was selected because it contains the most-well-sampled phase coverage over one proposed orbital period while also aligning well with the current RV spread; however, it is important to stress that is only one of many potential solutions to the data. This solution shows an orbital period of  $P = 0.22$

days with the eccentricity fixed to  $e = 0$ , which is a reasonable assumption for such a short orbital period, given that we do not have any reason to believe that such a small orbit would not be circularized. There were shorter period solutions when *The Joker* was given a shorter minimum period parameter, but the current RV spread appeared far too small to warrant these solutions as they require the  $\Delta RV_{\max}$  to be  $\sim 30\text{--}40 \text{ km s}^{-1}$  larger than observed. There are also longer period solutions that one can achieve by imposing a larger minimum orbital period; however, these solutions generally depended on the observations being poorly distributed in orbital phase, and, in some case, bunch the observations in such a way as to also, ironically, result in  $\Delta RV_{\max}$  that are  $\sim 30\text{--}40 \text{ km s}^{-1}$  larger than observed. The period and  $m \sin i$  from our adopted solution are likely lower limits, and clearly additional data are required to fully constrain the orbital parameters for this system. This system comes from the Rebassa-Mansergas et al. (2013) catalog of photometrically selected WDMS candidates, and we keep this classification and update it to be a PCE candidate given our updated contributions to the RV variation.

### 3.5.5 2M14544500+4626456

APOGEE observed this target with seven high-quality APOGEE visits spanning almost four years from 2013 March to 2017 March. APOGEE spectroscopic analysis again reveals an M dwarf primary with super-solar metallicity ( $[\text{Fe}/\text{H}] = +0.15$ ). *The Joker* returned a unimodal solution for this system, and an MCMC run confirmed that result shown in Figure 3.6. Similarly to the situation with 2M13054173+3037005, we fix the eccentricity to be  $e = 0$  to limit the degrees of freedom as we do not currently have sufficient data to prefer an eccentric orbit at this time. As with 2M11463394+0055104, our solution yields a minimum WD mass of  $m \sin i = 0.693 \pm 0.001 M_{\odot}$ , which places the mass near the upper end of the SDSS and LAMOST dis-

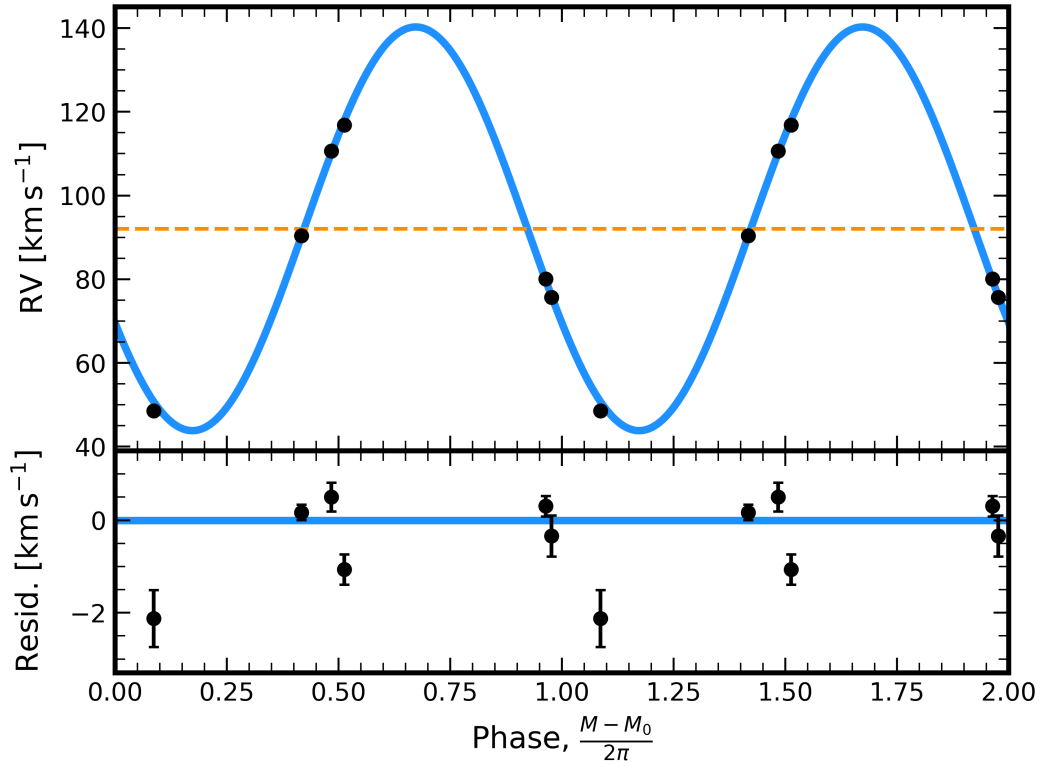


Figure 3.5: The same as Figure 3.3 but for the six APOGEE RV epochs for 2M13054173+3037005 and assuming a circular orbit. While the number of epochs is small, their phase coverage is very good *for this adopted solution*, while the RV amplitude is very large, which results in a solution that converges to a tight match with the data.

tributions. The orbital period corresponding to this solution is  $P = 15.10$  days, which would make this system second longest known orbital periods for the typical, compact PCE WDMS systems, behind the five self-lensing systems ( $P \sim 88 - 683$  days; Kruse & Agol, 2014; Kawahara et al., 2018; Masuda et al., 2019) as well as IK Peg ( $P = 21.72$  days; Vennes et al., 1998) and just above SDSS J222108.45+002927.7 and SDSS J121130.94-024954.4 ( $P = 9.59$  days and  $P = 7.82$  days, respectively; Rebassa-Mansergas et al., 2012). With the given number of visits, the phase sampling could be such that this solution is not an accurate model for the system. Additional

64

RV data will be necessary to adjust or falsify this model in the future; however, we report the best-fit solution we derived as the most likely estimate for the period given the APOGEE data. As this system was flagged as a candidate WDMS system by LAMOST, this classification will need to be confirmed. If the WDMS classification and our orbital solution is confirmed, 2M14544500+4626456 will be a useful PCE system for applying the methods in Rebassa-Mansergas et al. (2012) to explore the earlier phases of such systems and the energy budget of CE evolution.

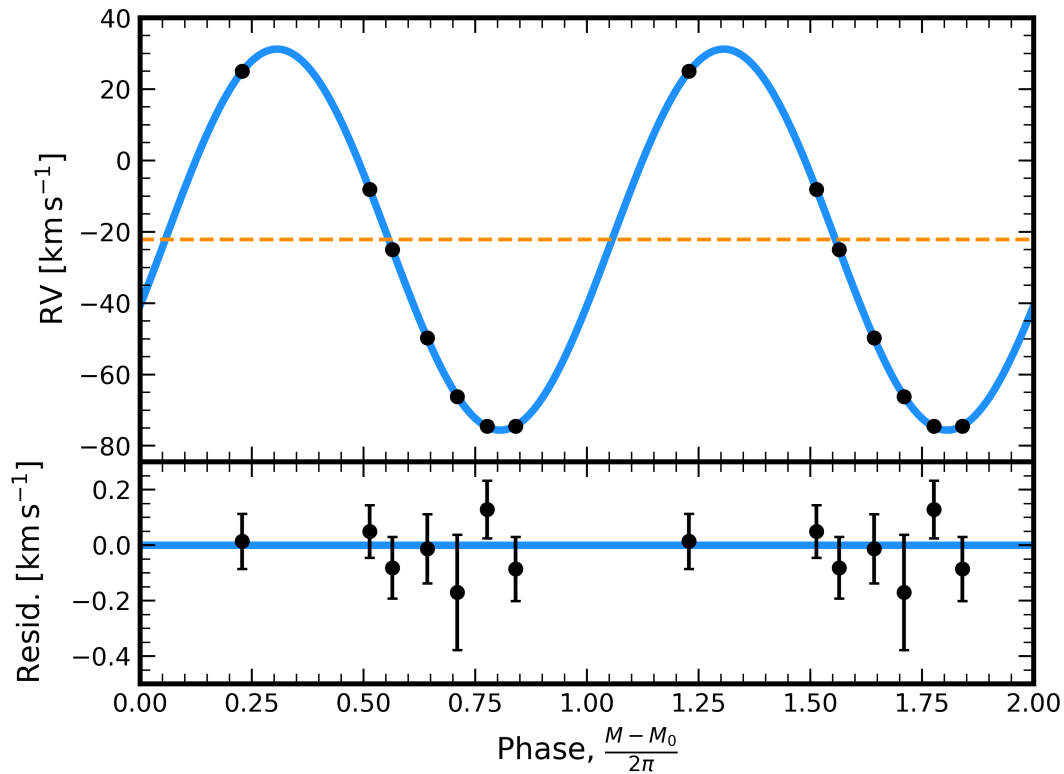


Figure 3.6: The same as Figure 3.3 but for the seven APOGEE RV epochs for 2M14544500+4626456. While the number of epochs is relatively small, the combination of very good phase coverage and a large RV amplitude means that a very good solution is possible, under the assumption of a circular orbit.

### 3.5.6 Wide Binaries

There are seven systems with 6+ high quality epochs that have a small ( $\Delta RV_{\max} < 10 - 20 \text{ km s}^{-1}$ ) RV spread that may correspond to  $K_{\text{MS}} < 5 - 10 \text{ km s}^{-1}$ . This low RV spread could be due to a lower inclination angle, which would make detecting shifts in the radial velocity more difficult. As we cannot place limits on this inclination given the present data, we proceed under the assumption that these relatively small shifts are a by-product of a system with a large orbital separation and long orbital period. Indeed, Willems & Kolb (2004) showed that wide-WDMS binaries should typically have small RV shifts ( $K_{\text{MS}} \sim 1 - 5 \text{ km s}^{-1}$  at  $i = 60^\circ$ ) at longer orbital periods ( $P > 100$  days). For this reason, we classify these seven systems as wide binaries, with the understanding that lower inclination angles could mean that we simply cannot detect more massive systems, even if they were compact, PCE systems.

Additionally, we perform a separate rejection sampling with *The Joker* with a higher than normal number (512 as opposed to 256) requested samples for these systems. By analyzing the period distribution and a period versus eccentricity diagram for the potential solutions for these systems (examples shown in Figure 3.7), we attempted to find groupings of possible solutions that are indicative of limits to the orbital period of the system. In the case of WBs, this would be a lower limit based on the smaller RV spread. This exercise sometimes does not yield conclusive results; therefore, we present lower limits on the orbital period for these WB systems in Column 3 of Table 3.2, but we advise caution in interpreting these results as they may not be indicative of the true solution. The  $\Delta RV_{\max}$  value presented in Column 2 similarly act as a rough limit of twice the potential velocity semi-amplitude for each system based on the current data.

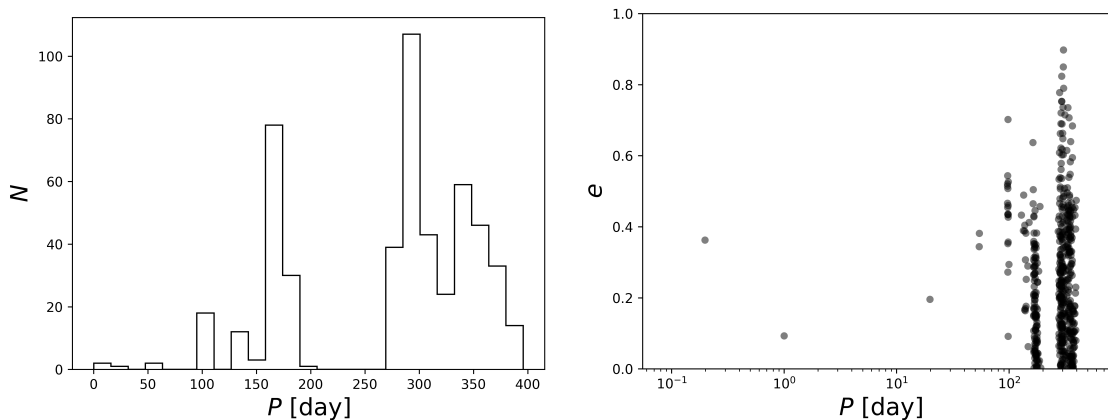


Figure 3.7: Plots used to place limits on the orbital periods of WBs and two PCE systems. In this example for 2M12423245–0646077, two predominant groupings are found in the period versus eccentricity diagram (right) for the 512 possible solutions. We then place the cautious lower limit of  $P = 150$  d as the period distribution (left) clearly shows that a majority of the solutions fall at longer orbital periods. For some systems, there are more random solutions amongst the groupings. The limits on the two PCE systems were evaluated with the eccentricity fixed to  $e = 0$  and with upper rather than lower limits.

### 3.5.7 Targets with 2-5 RV Visits

There are ten systems that have from two to five high-quality visits in APOGEE. Two of these systems (2M01575656–0244460 and 2M15150334+3628203) have an RV spread of  $\Delta RV_{\max} > 60 \text{ km s}^{-1}$ , which is sufficiently large to classify them safely as PCE systems, despite the fact that there is insufficient data to derive a full orbital solution. These two systems were identified as candidate WDMS systems from the SDSS photometric catalog, and we again update the classification to a PCE WDMS candidate; however, 2M01575656–0244460 shows a significantly blue GALEX (Bianchi et al., 2017) FUV-NUV color (-0.26 mag) which is likely indicative of a WD companion. Additionally, there are two other systems that are well known PCE WDMS systems (2M04322373+1745026 and 2M12154411+5231013; HZ 9 and EG UMa; see Rios-Venegas et al. 2020 and Bleach et al. 2000 and references therein, respectively)

that were observed. We do not attempt to add to the previous orbital studies of EG UMa and HZ 9 as we have only have two and three data points, respectively, that are temporally close to one other; however, we do still report the MS star mass derived from our ASPCAP parameters for each. The mass we derive for EG UMa's MS component is consistent with previous studies, and the mass for HZ 9 is only slightly higher than those shown in Rios-Venegas et al. (2020) and references therein. Using similar reasoning to that in Section 3.5.6, we provisionally classify the remaining six systems as candidate wide-WDMS binaries.

Additional RV epochs will be necessary for the candidates to confirm these classifications because, for a variety of reasons, the current data are not sufficient to reveal their true nature. Similar to what was done in Section 3.5.6, though, we view period distributions and period eccentricity diagrams in an attempt to place limits on the periods of these systems. For the WB candidates, we again set cautious lower limits on the period. For the two PCE candidates, we first fix the eccentricity to  $e = 0$  (under the same reasoning employed in Sec. 3.5.4 and 3.5.5) and then place a cautious upper limit to the current data. As the RV spread on these systems is significantly larger than the WB candidates, this limit is more robust than the lower limits on the WBs; however, the number of data points is still small and, therefore, abundant caution should still be exercised in adopting these values until additional data can test the significance of each limit.

Table 3.2: Orbital parameters derived using *The Joker* for systems with more than one RV visit. For WB systems, the period reported is a cautious lower limit on the period. For two of the marked PCE systems, the period reported corresponds to a cautious upper limit based on the small number of data point; the other marked PCE system has entries that represent one of many possible solutions. Here  $m \sin i$  refers to the WD as the MS star ( $M_*$ ) is the star being fit by the RV template. Here  $\Delta RV_{\max}$  serves as a rough limit of twice the velocity semi-amplitude ( $K$ ). 2M22145972–0820200 does not have ASPCAP parameters and, therefore, no mass can be derived.

APOGEE ID	$\Delta RV_{\max}$ [ $\text{km s}^{-1}$ ]	$P$ [days]	$e$	$K$ [ $\text{km s}^{-1}$ ]	$\gamma$ [ $\text{km s}^{-1}$ ]	$M_*$ [ $M_{\odot}$ ]	$m \sin i$ [ $M_{\odot}$ ]	$T_{\text{eff,WD}}^{\dagger}$ [K]
PCE Systems								
2M01575656–0244460 <sup>a,e</sup>	75.13 ± 0.07	3.5	0	-	-	0.534 ± 0.034	-	-
2M04322373+1745026	-	-	-	-	-	0.440 ± 0.028	-	29727 ± 691
2M10243847+1624582	293.19 ± 11.63	0.5258733 ± 0.0000056	0.0295660 ± 0.0143324	145.6 ± 2.3	-8.5 ± 1.7	0.423 ± 0.027	0.537 ± 0.013	15246 ± 482
2M10552625+4729228	148.07 ± 0.08	2.1866303 ± 0.0023683	0.0033047 ± 0.0157235	82.4 ± 1.0	8.2 ± 0.9	0.446 ± 0.029	0.476 ± 0.009	26801 ± 113
2M11463394+0055104	373.00 ± 2.07	0.4087104 ± 0.0000114	0.0272674 ± 0.0135032	186.8 ± 2.1	-12.5 ± 2.8	0.440 ± 0.028	0.717 ± 0.014	-
2M12154411+5231013	-	-	-	-	-	0.485 ± 0.031	-	15601 ± 586
2M13054173+3037005 <sup>b,e</sup>	68.26 ± 0.15	0.2165179 ± 0.0000015	0	48.2 ± 0.4	92.0 ± 0.2	0.453 ± 0.029	0.091 ± 0.001	-
2M14544500+4626456 <sup>c</sup>	99.53 ± 0.04	15.0957084 ± 0.0000698	0	53.41 ± 0.06	-22.20 ± 0.05	0.488 ± 0.031	0.693 ± 0.001	-
2M15150334+3628203 <sup>a,e</sup>	228.08 ± 0.11	13.5	0	-	-	0.489 ± 0.031	-	-
WB Systems								
2M03160020+0009462 <sup>c,e</sup>	0.87 ± 0.02	-	-	-	-	0.483 ± 0.031	-	19416 ± 1144
2M03452349+2451029	1.08 ± 0.01	20.0	-	-	-	0.502 ± 0.032	-	-
2M08094855+3221223	0.91 ± 0.05	200.0	-	-	-	0.436 ± 0.028	-	-
2M09463250+3903015 <sup>c</sup>	0.37 ± 0.08	-	-	-	-	0.486 ± 0.031	-	-
2M12423245–0646077 <sup>e</sup>	2.58 ± 0.07	150.0	-	-	-	0.478 ± 0.031	-	-
2M13115337+1549147	1.01 ± 0.12	100.0	-	-	-	0.436 ± 0.028	-	-
2M14244053+4929580	3.52 ± 0.59	100.0	-	-	-	0.438 ± 0.028	-	36572 ± 475
2M14551261+3810342 <sup>d,e</sup>	0.43 ± 0.01	-	-	-	-	0.431 ± 0.028	-	14728 ± 2041
2M15041191+3658150	1.03 ± 0.06	100.0	-	-	-	0.440 ± 0.028	-	-
2M18454771+4431148 <sup>c</sup>	0.43 ± 0.00	400.0	-	-	-	0.913 ± 0.058	-	33740 ± 3576
2M22145972–0820200 <sup>c,e</sup>	0.04 ± 0.01	-	-	-	-	-	-	-
2M22200576–0418445 <sup>c,e</sup>	0.11 ± 0.00	-	-	-	-	0.442 ± 0.028	-	-

<sup>†</sup> Estimate from the system's respective catalog

<sup>a</sup> Here  $P$  refers to a cautious upper limit with an eccentricity fixed to  $e = 0$

<sup>b</sup> Here the entries are for one of many possible solutions

<sup>c</sup> Here there are only two RVs that are too close temporally to place accurate limits

<sup>d</sup> Here the data produced incommensurate potential solutions such that no limit can be placed on the period

<sup>e</sup> Labelled as candidate WDMS system in the respective catalog

### 3.5.8 Targets with a Single Visit

There are seven of the remaining 28 systems that only received one high-quality visit throughout the course of the APOGEE survey and two that were targeted by APOGEE, but for which the data were insufficient for either the derivation of a radial velocity and/or ASPCAP parameters. No RV variations for these systems can be determined in this work, and it is unlikely that these systems will receive additional APOGEE visits in the future; however, the RV measurement (when present) for each system is included in Appendix 3.8 for completeness. In the future, these measurements can be combined with those from dedicated follow-up studies or other spectroscopic sky surveys. Available APOGEE measurements for these systems are listed in Table 3.3 in Appendix 3.8.

## 3.6 METALLICITY DISTRIBUTION OF WDMS SYSTEMS

The APOGEE database, featuring chemical abundances derived from high resolution spectroscopy and multi-epoch radial velocities, provides a unique opportunity to explore correlations between stellar chemistry and binary star architectures (e.g., Mazzola et al., 2020). The metallicities of M dwarfs, which constitute most of the MS companions in the present sample, are notoriously difficult to measure (e.g., Newton et al., 2014), however Souto et al. (2020) show that ASPCAP is sufficient to measure metallicities for these low-mass stars within about 0.1 – 0.2 dex. The ASPCAP fits do not take into account irradiation effects from the WD or tidal distortion effects in determining stellar parameters, but, based on available temperature estimates for the WDs in our sample, we do not expect these to significantly affect the metallicities of the M dwarfs in our sample. We therefore exploit these ASPCAP parameters

here to explore the metallicity distribution of our vetted and cleaned WDMS sample, which is a parameter space not often explored for these systems, but one that has been questioned as potentially correlated to other system characteristics. For example, among the few studies looking at WDMS metallicities, Rebassa-Mansergas et al. (2016b) explored the age-metallicity relation for a dataset of 23 WDMS systems and found no significant correlation between the MS star’s  $[\text{Fe}/\text{H}]$  value and the WD’s age. Meanwhile, Parsons et al. (2018) measured metallicities for thirteen eclipsing, PCE WDMS systems and did not find clear evidence for the metallicity to be the cause of over-inflation in the radii of their M dwarf sample.

Figure 3.8 shows the metallicity distribution of our 21 systems, separated into their respective classifications of WB or PCE systems. As discussed in Section 3.3, there is one system (2M14244053+4929580), found here to be a WB, that is extremely metal-poor ( $[\text{Fe}/\text{H}] = -1.4$ ) compared to all other systems in this paper. In fact, this  $[\text{Fe}/\text{H}]$  is  $\sim 0.6$  dex more metal poor than that for the most metal-poor system from Rebassa-Mansergas et al. (2016b). Recently, however, Rebassa-Mansergas et al. (2019) studied another eclipsing, PCE WDMS system, SDSS J235524.29+044855.7, a short period binary containing a halo subdwarf with  $[\text{Fe}/\text{H}] = -1.55 \pm 0.25$ , which then relegates 2M14244053+4929580 to the second most metal-poor WDMS system reported to date. As in the case of the former system, a metallicity this low is typically indicative of a star system that belongs to the Milky Way halo population; however, a kinematical analysis does not support that assumption. We used the `astro-gala` (Price-Whelan, 2017) Python package along with the combined APOGEE RV and *Gaia* parallax and proper motion to calculate the system’s orbit. The result, shown in Figure 3.9, reveals the system to have a rather prototypical (old) disk star orbit, with a maximum excursion from the disk of only 0.48 kpc over a radial variation ranging from 3 to 10 kpc. The juxtaposition of this rather planar orbit with such

a low metallicity makes 2M14244053+4929580 a somewhat unusual system (even ignoring that it is also a WDMS binary). Because it seems an outlier, in the following analyses we consider statistics that both include and exclude this unusual system.

At the other end of the MDF, four of the PCE systems, and many WBs, appear to have super-solar  $[\text{Fe}/\text{H}]$  values. However, the overall metallicity distribution of PCE systems seems to be significantly higher than that for WB systems. This is born out by the medians and dispersions of the two groups, which are 0.114 dex with  $\sigma = 0.109$  dex for the PCE, but  $-0.059$  dex with  $\sigma = 0.409$  dex ( $-0.037$  dex and  $\sigma = 0.141$  dex excluding the subdwarf) for the WBs. The latter group have a metallicity distribution function similar to that for the full APOGEE sample of MS stars with similar effective temperatures and surface gravities to those of the WDMS sample (shown for comparison in Figure 3.8). These values demonstrate that the median metallicities of the two systems are separated by  $\sim 1\sigma$ .

A Kolomogorov-Smirnov (KS) test<sup>3</sup> of the two distributions with the hypothesis that the WB and PCE systems derive from the same parent distribution yields a KS statistic of  $D = 0.556$  (see Fig. 3.8, bottom panel) and a  $p$ -value of  $p = 0.058$ , meaning the hypothesis can be rejected at the 90% confidence level. Because KS tests are not always sensitive enough to determine whether two distributions are independent, we also perform an Anderson-Darling (AD) test, which is more sensitive to a distribution’s wings and yields a standardized test statistic of  $T = 3.598$ . This value allows us to firmly reject our hypothesis at the 97.5% confidence level. Repeating these tests with the metal-poor WB removed does not change the KS  $D$  statistic, and, with only a slight change in sample size, yields similar results: a KS  $p$ -value of 0.084, implying a rejection of the null hypothesis at the 90% confidence level, and an AD

---

<sup>3</sup>All statistical tests here make use of the `scipy.stats` (Virtanen et al., 2020b) Python module.

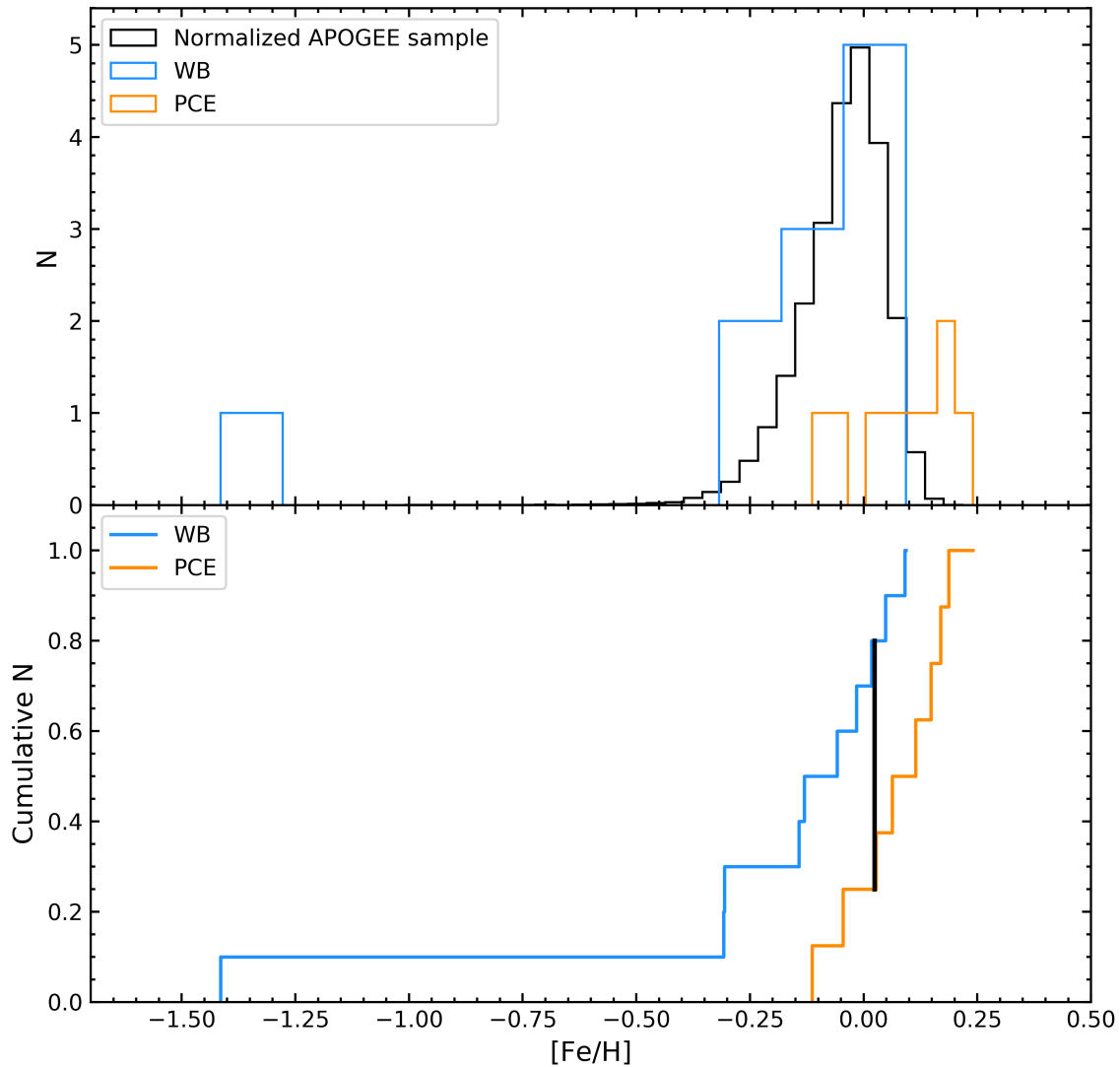


Figure 3.8: *Top*: The metallicity distribution of the WB and PCE systems listed in Table 3.2 shown in blue and orange, respectively. For comparison we also show in black the distribution of APOGEE MS stars sharing similar effective temperatures and surface gravities as the MS primaries in the WB and PCE samples. *Bottom*: Cumulative distribution for the WB and PCE in blue and orange, respectively. The thick, black, vertical line shows the KS  $D$ -statistic, the maximum distance between the two distributions.

test with  $T = 2.988$ , rejecting the null hypothesis firmly at the 97.5% confidence level. Meanwhile, in contrast, a KS test comparing the WBs and the APOGEE MS star sample show them to be essentially indistinguishable.

The difference in the  $[\text{Fe}/\text{H}]$  distribution of WB and PCE systems could speculatively point to some sort of alteration of a system's surface chemistry during the CE phase. However, Hjellming & Taam (1991) showed that CEs have much higher specific entropies than the surface of the secondary star, meaning the companion should be thermally isolated from the CE and, as a result, almost no accretion takes place. Thus, it would seem that the M dwarfs would not be polluted by metals during the CE phase. The previously discussed results of Parsons et al. (2018) that M dwarf radii in PCE systems were indistinguishable from the radii of field M dwarfs would also support this hypothesis; however, it is worth noting that some M dwarfs in PCE systems in the center of planetary nebulas are substantially inflated (e.g., Jones et al., 2015). This may be evidence that the companions are actually slightly altered by the CE phase, but only affected for a short while. Could a possible explanation for the observed metallicity difference be that the effects of close binarity alter the metallicities? Could rapid rotation in close systems affect the metallicities? Of course, the results here must be considered tentative given the overall small WDMS sample, especially given selection biases in the parent samples (see Section 3.3). Nevertheless, the metallicity differences seen here between the PCE and WB groups offer a tantalizing incentive for further studies of the chemistry of WDMS systems. A significant contribution in this direction can be expected from the APOGEE survey itself, where a large number of newly discovered WDMS candidates have been found (Anguiano et al., 2020, 2022). Moreover, not only do the majority of these systems have well characterized metallicities by APOGEE, but more detailed chemical abundance patterns as well, a unique opportunity for WDMS surveys to gain key insights into the

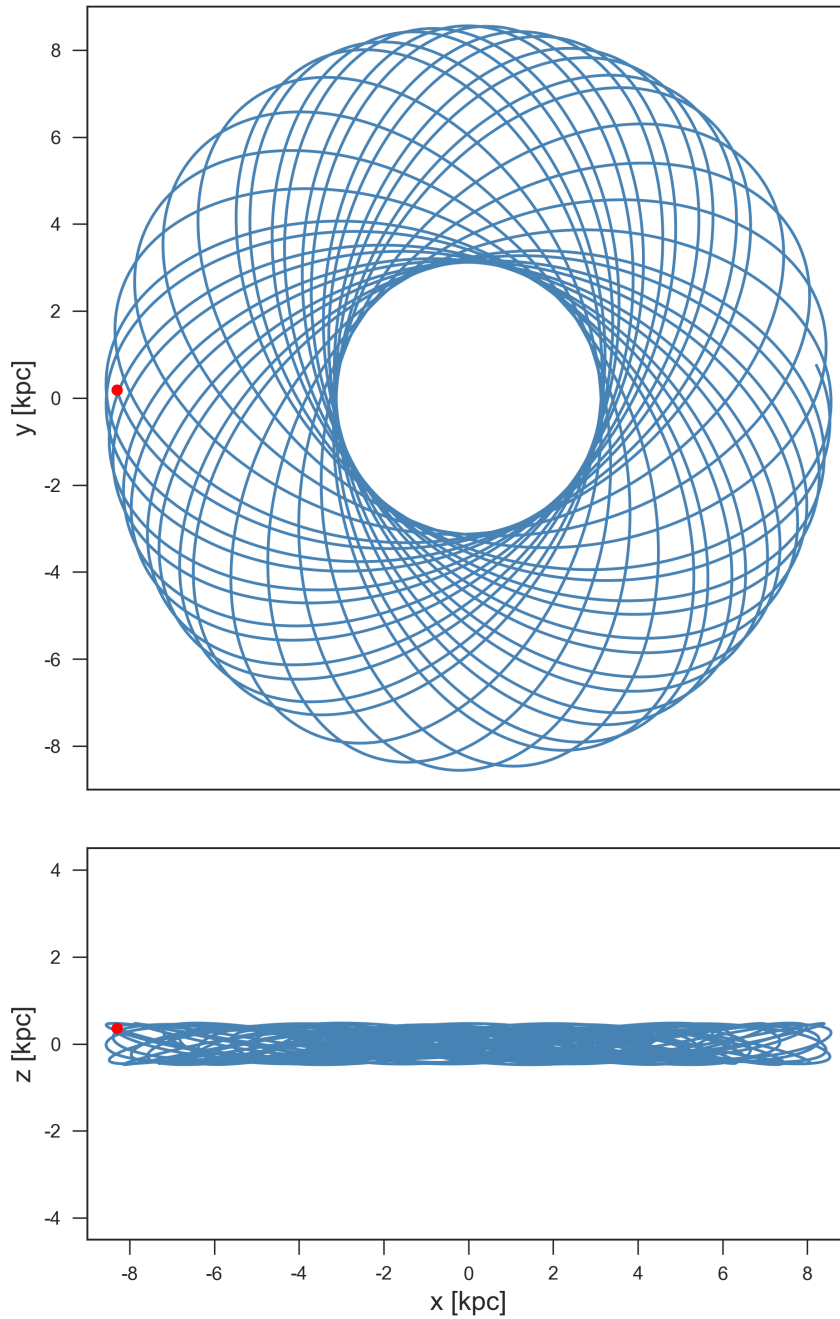


Figure 3.9: The calculated orbit for 2M14244053+4929580 aged 5 Gyr backwards from the present day, shown in the Galactic Cartesian coordinate system with a 1:1 aspect ratio in both projections to emphasize the planar nature of the orbit. The red dot marks the system’s current location. It is clear that this system has a very disk-like orbit despite being having a metallicity ( $[Fe/H] \sim -1.4$ ) rather typical of the Galactic halo.

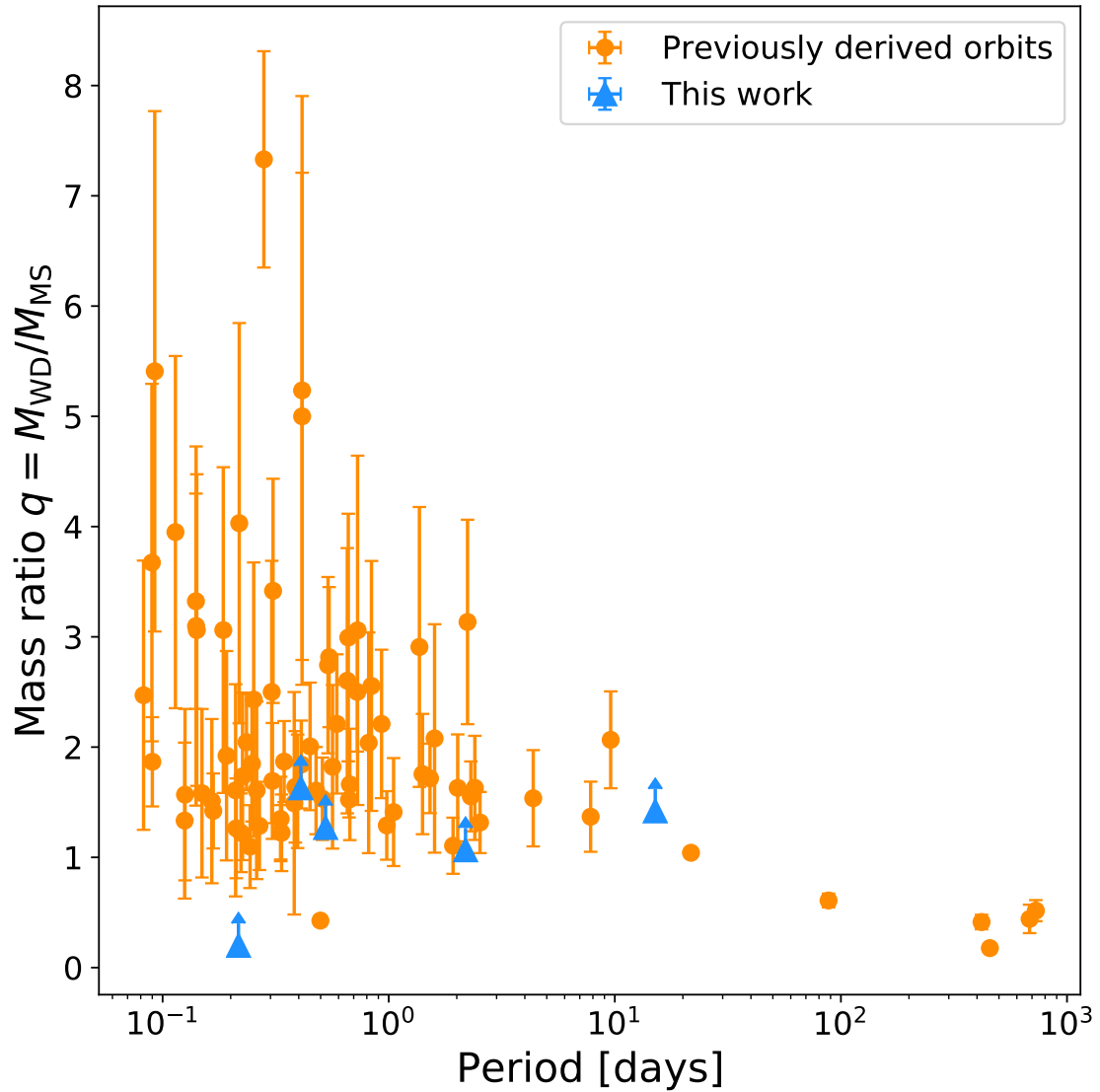


Figure 3.10: Mass ratio,  $q$ , versus period for PCE systems with previously derived orbital parameters and component masses (orange). The five systems with orbital parameters derived in this work are also shown (blue). The mass ratios for the latter represent lower limits on  $q$  because we derive the minimum WD mass from the Keplerian orbital parameters.

role of chemical composition in the evolution of WDMS systems.

### 3.7 SUMMARY

We have presented an analysis of the 45 candidate or confirmed WDMS systems identified by SDSS and LAMOST that also lie in the APOGEE survey. The results of our investigation of these systems are as follows:

- By examining the APOGEE-derived stellar parameters for the putative MS star in each system (Fig. 3.1a), APOGEE identifies three to be RG contaminants and 14 to be YSO contaminants of the 45 stars in the parent sample (Sec. 3.3). We propose various reasons why YSOs may have a high contamination rate within photometrically-selected WDMS catalogs and have thereby come to constitute almost a third of our starting sample.
- After imposing quality cuts on acceptable APOGEE RV measurements, we used *The Joker* to derive or place limits on the orbital parameters for 14 of the WDMS systems having more than two visits (Sec. 3.4.1). In addition, using the Torres et al. (2010) relations and the APOGEE stellar parameters, we derive the MS star mass for each system, when that is possible (Sec. 3.4.2).
- A key result of our orbital analysis is the confirmation of nine previously confirmed or candidate PCE systems: two that are well known (Sec. 3.5.7), three that are newly confirmed (Sec. 3.5.1-3.5.3), and four that are newly discovered (Sec. 3.5.4-3.5.5, 3.5.7). For three of these systems we present robust orbital solutions (Sec. 3.5.1-3.5.3), while a reasonable solution is given for another (Sec. 3.5.5) and a lower-limit solution for the remaining one (Sec. 3.5.4), thereby adding to the relatively small ( $\sim 90$ ; e.g., Nebot Gómez-Morán et al., 2011; Rebassa-Mansergas et al., 2016a; Parsons et al., 2015) number of PCE

systems having derived orbital parameters<sup>4</sup> and the  $\sim 120$  having at least spectroscopically or photometrically defined orbital periods (e.g., Ren et al., 2018).

- Though the mass ratios derived in this work (shown in Figure 3.10) represent lower-limits for  $q$ , they tend to imply low mass ratios (with  $1 \lesssim q \lesssim 2$ ), which is similar to what has been found for a majority of previous solutions for other systems.
- While the three systems for which we derive robust solutions have orbital periods typical of most PCE systems, our solution for 2M14544500+4626456, if confirmed to be a WDMS, would make it a PCE WDMS binary with the second longest period known for typical, compact systems (Sec. 3.5.5). We also have contributed 12 tentative WB classifications (Sec. 3.5.6), however, these may, of course, change with additional RV data in the future.
- We report 2M14244053+4929580 to be by far one of the most metal-poor WDMS systems known to date, with an  $[\text{Fe}/\text{H}]$  near the mean for the Galactic halo, of which we initially suspected it to be a member (Sec. 3.3, 3.6). However, an analysis of the orbit of this binary (Fig. 3.9) shows it to have an orbit more characteristic of a Galactic disk star (Sec. 3.6).
- The WB stars in our sample have an MDF that is significantly skewed to lower metallicities than the PCE stars (Fig. 3.8). We speculate on reasons for this MDF difference, but also caution that the analysis is based on a relatively small sample (Sec. 3.6).

The results of the present exploration of previously known WDMS systems demonstrate the efficacy of APOGEE data for not only characterizing the orbital properties

---

<sup>4</sup>Orbital parameters and component masses for 90 PCE systems are available at <https://www.sdss-wdms.org/>.

of such systems, but also for identifying new WDMS candidates by their RV variability, in particular, those sources with short period solutions that can add to the known number of PCE WDMS binaries having derived orbital parameters. In fact, (Anguiano et al., 2022) extended the analysis of this work to a larger sample of WDMS systems selected from APOGEE more broadly spanning the Hertzsprung-Russell diagram. Their analysis also shows a WB sample skewed toward lower metallicities than the sample of PCE systems. They also showed that binaries with MS companions in their sample have larger RV spreads than the overall sample of APOGEE DR17, implying these WDMS systems have shorter periods. Future work with these systems using APOGEE’s chemical and orbital information could likely yield insights into the observed differences seen in short-period WDMS binaries.

### 3.8 APPENDIX: SYSTEMS WITH ONE OR LESS HIGH-QUALITY VISITS

Table 3.3: Data for APOGEE systems in the cleaned sample with zero or one quality visit.

Ref. ID	JD	RV [km s <sup>-1</sup> ]	$M_*^a$ [ $M_\odot$ ]
2M08424235+5128575	2457046.86882	38.93282 ± 18.471933	
2M08531787+1147595	2458183.56201	80.99747 ± 0.09029441	0.463 ± 0.030
2M11241545+4558412	2457151.67308	8.04085 ± 0.0831778	0.478 ± 0.031
2M12333939+1359439	2458617.65376	85.52377 ± 1.351955	
2M13090450+1411351 <sup>b</sup>			
2M13463968-0031549 <sup>b</sup>			
2M15104562+4048271	2457898.68379	-22.661102 ± 0.1061763	0.413 ± 0.026

<sup>a</sup> If MS star with ASPCAP parameters available

<sup>b</sup> Received no high-quality visits

The seven systems shown in Table 3.3 were targeted by APOGEE, but, in the end, received zero or one quality visit over the duration of the survey. These systems

are not likely to receive additional visits in the APOGEE-2 survey, but obviously would benefit from additional data. The table summarizes what is known about these systems from the current APOGEE data in hand.



## CHAPTER 4

# LONG-TERM TIMING OF REDBACK MILLISECOND PULSARS IN GLOBULAR CLUSTERS

This chapter is in preparation to be submitted to *The Astrophysical Journal*.

## 4.1 INTRODUCTION

Millisecond pulsars (MSPs) with binary companions are an interesting class of radio pulsar and unique laboratories for various tests of fundamental physics. These neutron stars have been spun up via accretion of material from a close binary companion (Alpar et al., 1982), and we most commonly observe the resultant system in a relatively wide orbit with a low-mass, white dwarf companion (Manchester et al., 2005; Tauris & van den Heuvel, 2006). A portion of systems with other companion types, though, can evolve to much more compact orbits, and one such sub-class is called Redbacks (RBs). These MSPs are members of the “spider” pulsar family and have H-rich, non-degenerate companions that have masses typically between

$0.1M_{\odot} < M_c < 0.9M_{\odot}$  (Roberts, 2013; Strader et al., 2019). RBs typically have orbital periods of only a few hours, and their neutron star masses are generally found to exceed the canonical value of  $1.4 M_{\odot}$  (Strader et al., 2019). Additionally, RBs are exceptional producers of multi-wavelength emission, producing features such as radio pulsations,  $\gamma$ -ray pulsations (Deneva et al., 2021; Thongmeearkom et al., 2024), and optical light-curve variations (Bellm et al., 2016; Yap et al., 2023).

Due to their compact nature, binary interactions play a large role in the evolution and observed properties of RBs. The intense pulsar wind ablates material from the companion, creating circumbinary, ionized material. This material can cause radio eclipses – most likely caused by synchrotron absorption (Polzin et al., 2018) – that can shroud radio pulsations for significant portions of the orbit (Nice et al., 1990) around superior conjunction. These eclipses can be highly irregular, though, and dependencies on observing frequency can further impact the duration and appearance of any one eclipse (e.g., Nice et al., 1990; You et al., 2018). Additional eclipse-like events due to material at other orbital phases can also mask pulsations (e.g., Bilous et al., 2019), and infalling material almost certainly plays a role in the observed pulse properties of the MSP. Additionally, the long-term behavior of the binary orbit in RBs has been observed to wander drastically (Prager, 2017; Clark et al., 2021; Thongmeearkom et al., 2024), limiting the accuracy of binary models to describe the system over time.

Timing studies of MSPs in binaries given sufficient baselines can yield insights into interesting physics in areas such as general relativity (Jacoby et al., 2006) and the neutron star equation of state (Cromartie et al., 2020); however, the barrage of impediments listed above means RBs are often excluded from consideration for long-term timing efforts in the radio. Obtaining successive detections – let alone detections over short to long baselines – of the MSP can be difficult, and linking observations

together in a way that yields insights into the physical characteristics of these systems is also non-trivial, too. While the binary interactions in RBs may not make them ideal test beds for probing the most impactful binary physics, accurate measurements of physical properties derived from long-baseline timing still would yield important limits for use in modeling of the companion’s interior and binary evolution modeling that can inform a variety of interesting cases. The majority of published radio-timing solutions for RBs, however, only cover a baseline of a few years (Archibald et al., 2013; Prager, 2017; Miraval Zanon et al., 2018; Deneva et al., 2021; Padmanabh et al., 2024; Ghosh et al., 2024; Thongmeearkom et al., 2024), although Thongmeearkom et al. (2024) achieved  $\gamma$ -ray timing using *Fermi* data spanning 15 years from their shorter radio solution. However, Nice et al. (2000) presented a radio-timing solution for around a decade of targeted observations of B1744-24A. Targeted observations or even archival data spanning this duration or longer for individual RBs are also not generally available, making these long-term studies further difficult to conduct.

Globular clusters (GCs) present an opportunity to provide long-term baselines for RBs by exploiting observations of the cluster aimed at the pulsar population. Pulsar studies have long targeted GCs as they are effective factories for producing binary stars and by extension binaries containing pulsars (Ransom, 2008; Freire, 2013). Continued observations of these environments allow for increased sensitivity to discover new pulsars, to measure various characteristics of the known pulsars, and to disentangle the dynamics of the cluster from the astrophysical sources observed within them (Prager et al., 2017). This is especially true of GCs that contain a large population of pulsars.

Terzan 5 (hereafter Ter5) has the largest known population of pulsars in any GC (49; Padmanabh et al., 2024) with over half being in binaries – four of which are RBs. Ter5A is the first ever RB discovered (Lyne et al., 1990; Nice et al., 1990)

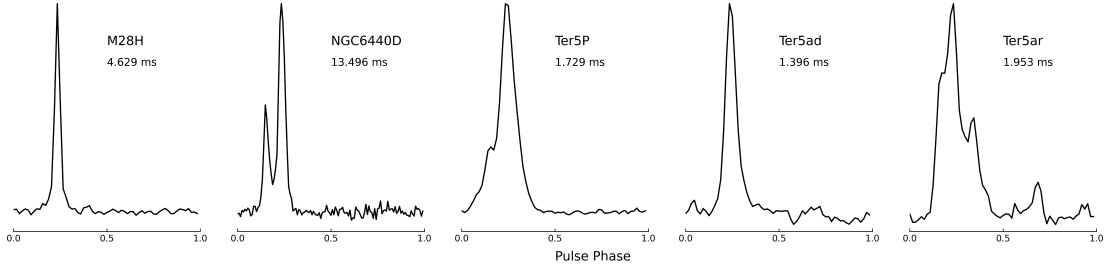


Figure 4.1: Summed pulse profiles from coherently dedispersed 2 GHz observations for each of the five RBs analyzed in this work.

and one of the most compact RBs known; Ter5ad is the record holder for the fastest spinning MSP ( $P \sim 1.39$  ms; Hessels et al., 2006); Ter5P is also rapidly spinning ( $P \sim 1.72$  ms), has the second largest mass fraction for RBs due to its more massive companion ( $M_{c,\min} \sim 0.38 M_{\odot}$ ), and is thought to be the product of pair exchange (where the star that spun up the pulsar is ejected and replaced with a more massive star; Ransom et al., 2005; Prager, 2017); and Ter5ar is a newly discovered, rapidly rotating ( $P \sim 1.95$  ms) RB with a larger mass companion ( $M_{c,\min} \sim 0.34 M_{\odot}$ ) as well (Padmanabh et al., 2024). A smaller population of binary pulsars is found in M28, and it, too, contains RBs – M28I, which is a transitional MSP (switches between a radio pulsar state and a low-mass X-ray binary state), and M28H, which is another RB thought to be the product of pair exchange (Pallanca et al., 2010; Bogdanov et al., 2011). NGC 6440, which has the smallest binary population of the three clusters mentioned here, also hosts a RB, NGC 6440D (Freire et al., 2008), that exhibits relatively stable orbital variations (Ransom et al., in prep). These three GCs have been actively monitored for nearly the past 20 years through observations at various frequencies using the Green Bank Telescope (GBT), making them unique vehicles to test RB timing methods on a longer scale than has previously been possible.

Here we present our long-term timing analysis of five RBs in GCs – Ter5P, Ter5ad, Ter5ar, M28H, and NGC 6440D – and our methods for achieving these solutions. In

§4.2 we briefly describe the roughly 20 years of archival data from the GBT. In §4.3 we present our technique for “isolating” the MSP from the orbital effects of the binary companion, allowing us to time the underlying, highly accurate clock. In §4.4 we present our fully phase-connected timing solutions, the long-term orbital variations that were removed to create them, and pulse profiles for each system. We then discuss the results from our technique and how they compare to those of conventional timing methods, the quasi-periodic oscillations seen in Ter5P, and a correlation between orbital variations and spin frequency in §4.5. Finally, we summarize our work in §4.6.

## 4.2 OBSERVATIONS

We used archival data for each cluster from observations with the GBT spanning roughly 20 years. A majority of our data were taken using S-band (1600-2400 MHz) and L-band (1100-1900 MHz) receivers with  $\sim 600$ -700 MHz of useable bandwidth in each case. Additionally, a smaller fraction of data were taken at 820 MHz. In our data, the GBT Pulsar SPIGOT (Kaplan et al., 2005) backend was used for all observations prior to MJD 55000, the GUPPI (DuPlain et al., 2008) backend was then used for observations up until MJD 58933, and that same day the VEGAS (Prestage et al., 2015) backend was switched onto the GBT<sup>1</sup>. The SPIGOT data were taken using incoherent dedispersion, and detailed information about the observations for Ter5, which were obtained in a consistent manner to the observations for M28H and NGC 6440, can be found in Ransom et al. (2005). Prior to MJD 55422, observations using GUPPI (only a few scans for each system) were also obtained with incoherent dedispersion; the remaining GUPPI and VEGAS observations were taken using coherent dedispersion, and detailed information about the observations for Ter5 can be found in Martsen et al. (2022). As with SPIGOT, the GUPPI and VEGAS observa-

---

<sup>1</sup>Consequently, we acquired observation with both GUPPI and VEGAS on this MJD.

tions were obtained in a consistent manner to those for M28H and NGC 6440, with the obvious exception of the dispersion measure (DM) where the coherent data are dedispersed.

### 4.3 TIMING METHODOLOGY

In the text that follows we introduce the prescription for and our workflow implementation of the Ransom-O’Neill Isolation (ROI)<sup>2</sup> technique. To briefly outline the process, we achieve ROI by breaking up the pulse times of arrival (TOAs) into binary-piecewise groups (O’Neill et al., in prep) to determine local solutions of the orbit at many points over the span of our baseline. We then remove the orbital timing delays from the TOAs in each group, allowing us to mitigate the strong, observation-to-observation variations present in each system. Thus, we effectively “isolate” the underlying MSP clock, which provides us the stability needed to track the rotations of the MSP over the entire baseline (phase-connect) and derive long-term timing solutions for its spin behavior.

#### 4.3.1 Detections and Initial $T_{0,x}$ Measurements

We used a code called SPIDER\_TWISTER<sup>3</sup>, which performs searches in orbital phase to return the most probable  $T_0$  – the time of passage through periastron, which for our circular ( $e = 0$ ) models is when the MSP crosses the plane of the sky moving away from the observer, called the time of the ascending node – value for a given observation, to obtain detections of the pulses for each system in our observations. As our data span roughly 20 years, we automated our searches by allowing SPIDER\_TWISTER to search  $\pm 10\%$  in orbital phase in the time-series for each observation from its asso-

---

<sup>2</sup>So initialized by K.A.C. as the upfront work to determine accurate  $T_{0,x}$  measurements yields a significant return on investment.

<sup>3</sup>[https://github.com/alex88ridolfi/SPIDER\\_TWISTER](https://github.com/alex88ridolfi/SPIDER_TWISTER)

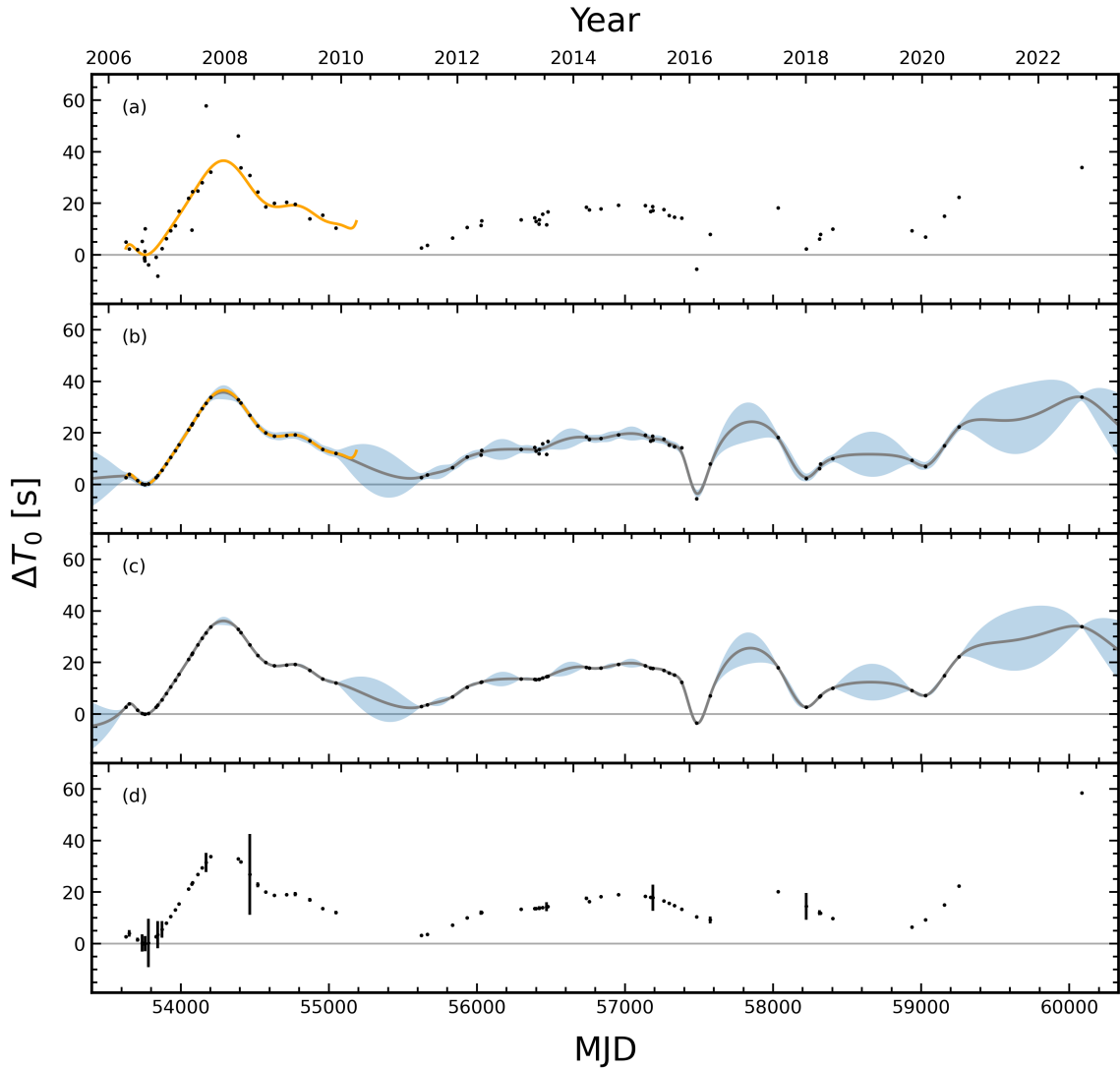


Figure 4.2: Each panel shows different measurements of time of periastron passage ( $T_0$ ) deviations over time for M28H as black points. In panel (a), we show the  $\Delta T_0$  values derived from the SPIDER\_TWISTER values described in §4.3.1, and we overlay in orange the predicted values from the phase-connected, BTX model described in §4.3.6. In panel (b), we show the  $\Delta T_0$  values accounting for BTX predictions, as well as a Gaussian process regression (GPR) to interpolate between the BTX-informed,  $T_0$  values and the remaining SPIDER\_TWISTER measurements. In panel (c), we show the remaining values set to those GPR predictions, as well as a new regression to describe the updated measurements. This process still benefits from manual improvement to ensure  $\Delta T_0$  is relatively smooth with time, and we show the resultant values and their errors in panel (d).

ciated  $T_0$  predicted by an initial set of parameters for each system. Even for systems with significant orbital wander, we found this search setup to be effective in finding all available detections in its dataset. We inspected the output plots of each time-series folded at the returned  $T_0$  value<sup>4</sup> ( $T_{0,x}$ ) and noted non-detections to discard for subsequent steps. At this stage, the  $T_{0,x}$  measurements are not necessarily the most accurate value for achieving ROI; however, these measurements are precise enough for obtaining TOAs from each observation. These measurements thus served as an initial set of values that we refined throughout the process (see panel (a) in Figure 4.2).

### 4.3.2 Producing TOAs

We folded the time-series data, using the `prepfold` routine from PRESTO<sup>5</sup> (Ransom, 2001, 2011), for each detection of each MSP using its predicted spin period, DM value, long-term average orbital parameters, and the  $T_{0,x}$  measurement for each observation obtained from SPIDER\_TWISTER. For Ter5P, Ter5ad, Ter5ar, and M28H, we then integrated over set intervals (10 min for Ter5P and M28H & 30 min for Ter5ad and Ter5ar) to obtain TOAs for each system. Due to the extremely rapid spin periods of Ter5ad and Ter5P, we used separate pulse templates for data obtained in incoherent and coherent dedispersion modes, allowing us to mitigate the effects of smearing for these systems. We visually inspected each fold and noted areas to avoid where there was no pulse (e.g., from both regular and irregular eclipses) as well as areas that may produce erroneous TOAs (e.g., when strong interference was present). We then used PRESTO's `get_TOAs.py` routine to extract TOAs for each observation in the areas where a signal was present. Finally, we discarded TOAs with errors larger

---

<sup>4</sup>We note that  $T_{0,x}$  here refers to  $T_0$  for each observation. Herein we generally use this to refer to the  $T_0$  value associated with an arbitrary, binary-piecewise group,  $x$ .

<sup>5</sup><https://github.com/scottransom/presto>

than  $30 \mu\text{s}$ .

In the case of NGC 6440D, we used the TOAs from Ransom et al. (in prep) with errors less than  $30 \mu\text{s}$ . These are produced by determining the number of TOAs that could be obtained with sufficient S/N in each observation and integrating over intervals that yield this number of TOAs (roughly 4-15 min integrations). We chose to maintain this slight difference in methodology rather than re-integrating at a set interval to keep the TOAs consistent between both analyses, allowing us to directly compare results obtained via traditional timing techniques to those obtained using the ROI technique.

### 4.3.3 Updating Orbital Properties

To ensure that our long-term description of the binary orbital properties was accurate, we used the  $T_{0,x}$  values from SPIDER\_TWISTER to determine the average orbital period of each system. For all systems except Ter5P and NGC 6440D, we assumed that the period of a circular orbit was constant over the baseline of our observations. We also assumed for all systems that the semi-major axis was constant (see Appendix 4.7 for more discussion on these assumptions). We then computed the difference between our measured  $T_{0,x}$  value and the value that would be predicted by a constant orbital period and its associated reference epoch  $T_{0,\text{ref}}$ . With a constant orbital period, these  $\Delta T_0$  values over time will show long-term, linear trends if an adjustment to  $P_b$  was necessary. We fit a linear trend in these cases as:

$$\frac{\Delta T_0}{t P_b} = \frac{\Delta T_0 f_b}{t} = \frac{\Delta \phi_b}{t}, \quad (4.1)$$

which describes the change in phase ( $T_0$  in this case) over time, which we used to update the period by computing the change to the orbital frequency via

$$f_{b,\text{new}} = f_{b,\text{old}} + \frac{\Delta T_0}{t} f_{b,\text{old}} \quad (4.2)$$

and then using

$$P_{b,\text{new}} = \frac{1}{f_{b,\text{new}}}. \quad (4.3)$$

In the cases of Ter5P and NGC 6440D, the dominant  $\Delta T_0$  trend was a quadratic; therefore, we fit both a quadratic and linear term to correct the  $P_b$  measurement.

### 4.3.4 Constructing Piecewise-Continuous Groups & Parameter Files

For RBs, it is sometimes possible to use a piecewise-discontinuous model to time the system over long baselines, wherein individual chunks of overlapping TOAs spanning some time frame can be strung together with fits using independent models with constant orbital parameters (e.g., Blandford & Teukolsky, 1976) to achieve a connected, long-term timing solution (see Rosenthal et al., 2024). A piecewise-continuous, binary model, though, allows for computation of timing residuals for all TOAs over the duration of the baseline with a proper and changing orbit without need for independent fits of other parameters. This process is particularly useful in cases where orbital variations make connecting overlapping chunks difficult. As such, we opted to use the `BT_piecewise` model (see O’Neill et al., in prep for full details on this model) inside the pulsar timing package, `PINT`<sup>6</sup> (Luo et al., 2021) in isolating the TOAs for each system. While this is not necessary for removing the timing delays described in §4.3.7, it is useful in predicting how the isolated timing residuals will

---

<sup>6</sup><https://github.com/nanograv/PINT>

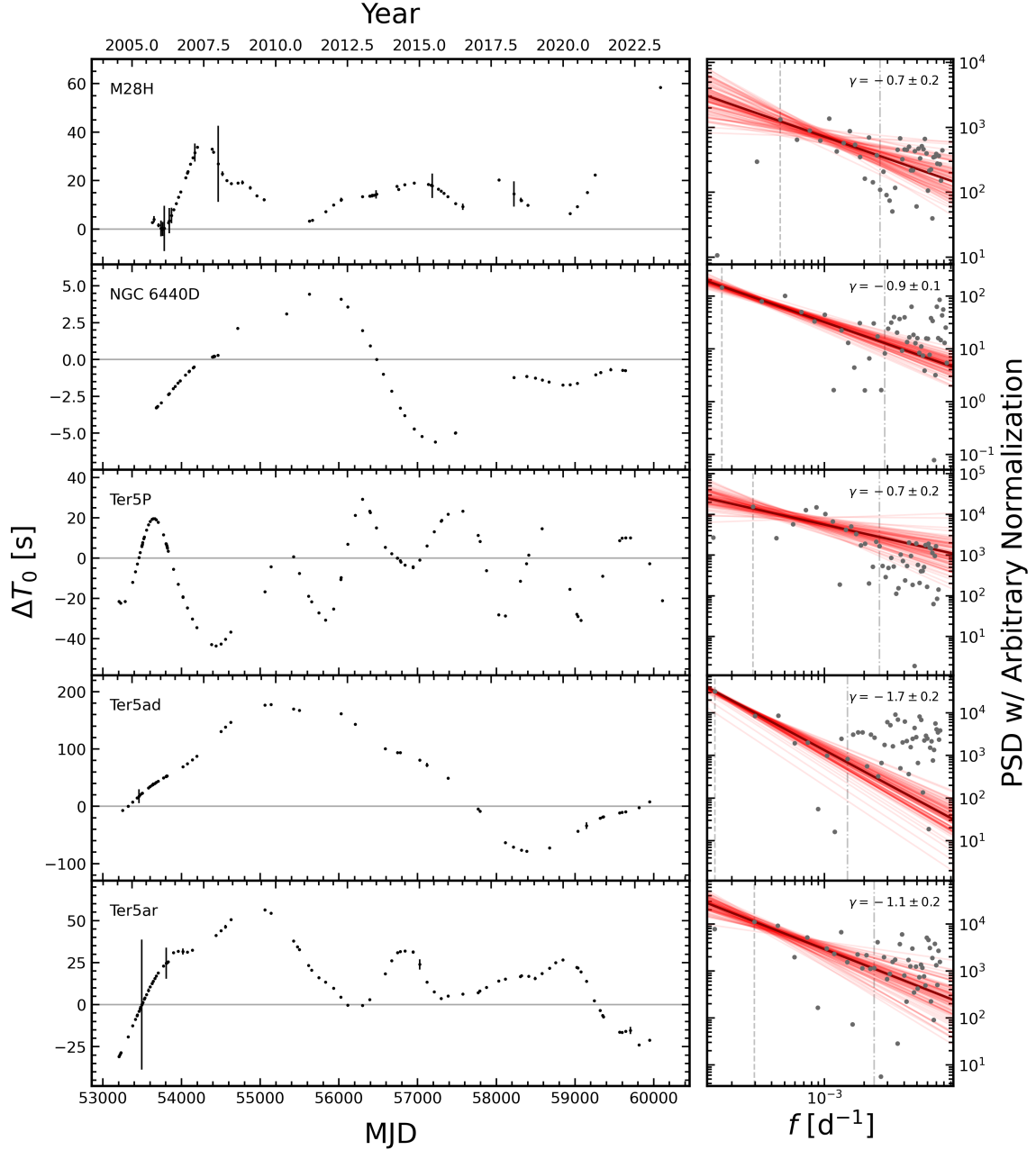


Figure 4.3: *Left:* As in Figure 4.2, phase variations ( $\Delta T_0$ ) for each system over time using their final  $T_{0,x}$  values. Note that NGC 6440D and Ter5P are shown with their respective  $P_b$ 's removed. *Right:* Power Spectral Densities (PSD; grey points) of the  $\Delta T_0$ s for each system from a Lomb-Scargle periodogram with an arbitrary normalization. In dark red we show the best fit power-law to the frequencies between the dashed and dash-dotted lines. The  $\gamma$  values and their error for this fit are given in the upper right of each plot. In red, we show a multi-variate gaussian sampling representing the error region of our fit.

look with those delays removed.

Using the TOAs from §4.3.2, we constructed an initial set of piecewise-continuous groups of similar TOAs for each system. We used the `TOAs.get_clusters` method inside `PINT`, to identify groups of temporally related TOAs over a specified gap limit. As our datasets contain varying sizes of gaps between observations, we tested a number of different gap limit values using TOAs from Ter5P and Ter5ar by iteratively refining the piecewise groups and  $T_{0,x}$  measurements. Ultimately, we found that a gap limit of 0.5 d worked well for most systems to group observations temporally very close together (e.g., two scans on the same day) while not creating groups too temporally large to get an accurate picture of the local solution. Due to the nature of how NGC 6440D’s TOAs were constructed, we used a gap limit of only 0.04166 d to create its piecewise groups as larger gap limit values created some groups with TOAs too sparse to describe the local orbital variations. Once all of the TOAs were assigned a group number, we generated four values for each group that the binary-piecewise model uses to describe local solutions: `XR1`, `XR2`, `A1X`, and `TOX`, which are the start, finish,  $a \sin(i)/c$ , and  $T_{0,x}$  values, respectively. It is important to note again that we assumed the semi-major axis of the binary is constant over our baseline for these systems

We then created three different parameter files (or par files) that describe each system – one that describes the local, binary solution of the piecewise groups, another the long-term, binary solution, and finally the isolated, spin behavior. To successfully track the rotations of the pulsar (phase connect) over the full timing baseline, it is helpful (although not strictly necessary) that these three par files be derived from a solution that has some portion of the data phase connected. We initially started with right ascension, declination, the spin frequency and its first derivative from previous short-duration phase connection from Ransom et al. (2005) & Padmanabh

et al. (2024) for Ter5 systems, Bégin (2006) for M28H, and Ransom et al. (in prep) for NGC 6440D. We then assumed simple binary models using the  $P_b$ ,  $\dot{P}_b$  (where applicable), and  $T_{0,x}$  values as determined in §4.3.3 to create the binary-piecewise and long-term binary par files. For the isolated par file, which only describes the MSP’s spin, we simply removed the binary information.

### 4.3.5 Refining $T_{0,x}$ with TEMPO

As previously stated, the initial measurements of  $T_{0,x}$  do not always suffice to accurately describe the behavior of each piecewise group. In general, the processes described in the following section are sufficient for correcting the accuracy of each measurement to proceed with the isolation steps. For Ter5P, as well as Rosenthal et al.’s (2024) work with Ter5A, though, we found that the results of those processes were improved by first refining the  $T_{0,x}$  measurements that are used as inputs by fitting  $T_0$  directly to the measured TOAs. To do this, we used TEMPO<sup>7</sup> and its TRACK capabilities to fit the TOAs for  $T_{0,x}$  in places where the value measured via SPIDER\_TWISTER was not sufficient. In some cases, problematic TOAs that had made it through the initial cleaning stage had caused the initial measurement to be less accurate, while in others, a correction for an improper phase wrap (i.e., pulse count) greatly improved the measurement. The TOX values were then updated in the binary-piecewise par file and used for the final improvement steps.

### 4.3.6 Refining $T_{0,x}$ via BTX Information & Gaussian Process Regression

To obtain  $T_{0,x}$  measurements that were sufficient to describe the local behavior of each group well, we implemented a two-step process to enhance each value’s ac-

---

<sup>7</sup><https://tempo.sourceforge.net/>

curacy. The first was to bring back some of the information that was discarded in creating the simple-binary model. We used the orbital frequency derivatives from the BTX solutions and phases from PINT’s `model_orbital_phase` method to compute the orbital period at the current  $T_{0,x}$  for each group contained in the original phase-connected solution (see panel (a) in Figure 4.2). For systems where we assumed a constant orbital period, which are all but Ter5P and NGC 6440D, this value did not change. These values were the driving force behind the earlier solutions for describing the orbit at all points for that data, so naturally they locally described the TOAs in those portions of our data to a high degree of accuracy. We then updated the  $T_{0,x}$  and  $\Delta T_0$  values for this subset of the data.

The second step was to use our BTX derived  $T_{0,x}$  values, the measured  $T_{0,x}$  values for the remaining groups, and both of their corresponding  $\Delta T_0$  values as inputs to train a Gaussian process regression (GPR; Rasmussen & Williams, 2006). We used the Matérn kernel implemented in the `scikit-learn` package (Pedregosa et al., 2011) with an initial length scale of  $\ell = 20$ , length scale bounds from  $1\text{-}10^4$  d, and a white noise kernel with a noise level of 1.5 s and noise bound from  $10^{-2}\text{-}10^2$  s. We used the GPR kernel to predict the  $T_{0,x}$  values for the groups not set by the BTX model (see panel (b) in Figure 4.2), and we used these values to update each TOX value for the piecewise groups (see panel (c) in Figure 4.2). While these values provided great improvement on the accuracy of the  $T_{0,x}$  measurements, the quality of the initial measurements were not always such that the GPR arrived at a value that properly described the TOAs local behavior. In these cases, we visually inspected  $\Delta T_0$  over time overlaid with the results of the GPR. We exploited the fact that the variation in  $\Delta T_0$  over time should be fairly smooth to determine the adjustments (ranging from only a few fractions of a second up to a few 10s of seconds) to the  $T_{0,x}$  value needed to correct the local behavior of a group’s TOAs (see panel (d) in Figure 4.2).

After iteratively refining the GPR, we updated the TOX values for the binary-piecewise model.

### 4.3.7 Isolating the MSP

With more refined measurements of  $T_{0,x}$ , we removed the short- and long-term characteristics of the binary to place each MSP in ROI. For each group in each RB's binary-piecewise model, we first used PINT to fit the simple-binary model for only  $T_{0,x}$  to get its uncertainty and, in a very small number of cases, updated the  $T_{0,x}$  measurement to further improve its accuracy. Next we removed TOAs with orbital phases coincident with a defined eclipse region as described by the simple-binary model, giving us a set of non-eclipsed TOAs,  $t_i$ . We then computed the Roemer delays ( $\Delta_R$ ) at  $t_i$  based on the simple-binary model, and we created an identical set of TOAs,  $t_{\Delta_R,i}$ , from which we then remove the Roemer delay. We also needed to apply barycentric to topocentric corrections ( $\beta_i$ ) to the predicted Roemer delays, which requires corrections to  $\Delta_R$  for both  $t_i$  and  $t_{\Delta_R,i}$  to properly describe an isolated state. To do this we used the simple binary model to compute corrections for the  $\Delta_R$  corresponding to  $t_i$ ,  $\beta_t$ , and we used the isolated model to compute corrections for the  $\Delta_R$  corresponding to  $t_{\Delta_R,i}$ ,  $\beta_{\Delta_R}$ , as these TOAs are now in a form of isolation. Using these two terms and  $\Delta_R$ , we then computed a first-order correction that describes the barycentering effects needed to remove the orbital timing delays from each group, defined as:

$$\beta_i = (\beta_t - \beta_{\Delta_R}) - \Delta_R. \quad (4.4)$$

We finally removed  $\Delta_R$  and  $\beta_i$  from  $t_i$ . The full sets of TOAs including all of the above corrections then represent the MSP in a state of ROI described by the isolated par file. Tests using simulated binary TOAs reveal that we are able to remove orbital effects to better than 100 ns using this technique.

### 4.3.8 Fitting & Inflating Uncertainties

We performed our fitting for long-term timing parameters like the pulsar spin frequency, frequency derivative, position and proper motion, using PINT. Initially, we use `pintk` – a GUI-based implementation of PINT– with a Downhill weighted least-squares fitter (Susobhanan et al., 2024) to get a preliminary, long-term fit as `pintk` allows for quick changes of various fitting parameters and TOA grouping. We included positions, proper motion in right ascension, DM, frequency, and various numbers of spin frequency derivatives in these fits. Susobhanan et al. (2024) performed various noise parameter tests that show the measured uncertainties on TOAs via fitting algorithms are likely underestimated on their own. They also added noise parameters to the PINT Downhill fitter that can be used to inflate the uncertainties to better describe the measured physical quantities in the fit. We therefore added two fitted error factors (EFACs) to our models – one for the incoherent data and the other for the coherent data – to inflate the errors from our initial fits. This inflation helps to compensate for the systematics due to un-measured and un-modeled DM effects caused by perturbations in the TOAs from the ionized gas in these systems. We chose not to include a fit for errors added in quadrature (e.g., EQUAD) as it may not properly describe the white noise of the isolated TOAs since the initial datasets are dominated by systematics. We then used PINT to perform the final fitting for each system, and we centered the epoch for our measurement of the spin period and the positions along our baseline.

## 4.4 RESULTS

### 4.4.1 Pulse Profiles

With the exception of Ter5ar, which is newly discovered (see Figure 3 in Padmanabh et al., 2024), the previously published pulse profiles for these RBs were only able to make use of the incoherent data available at the time. We therefore include summed pulse profiles derived from our coherent dedispersion observations for each MSP in Figure 4.1. Each profile is a sum of many tens to over 100 hours of S-band, coherent-dedispersion data centered at 2 GHz. Of note, we point out the secondary peak that can be seen in the profile of Ter5P, and we also see a noticeably sharper peak in the profile of Ter5P and Ter5ad than that of their incoherent profile in Ransom et al. (2005) and Hessels et al. (2006).

### 4.4.2 Phase Variations

The orbital variations and wander in RBs are a driving force of the systematics in the long-term solutions of each system. Thus, we show in Figure 4.3 our final measurements of  $T_{0,x}$  for the five RBs and how they compare to the value predicted by each simple-binary model over the baseline of each system. These variations represent a large portion of the orbital information removed by the ROI technique. We also show the same variations for Ter5P and NGC 6440D with the  $\dot{P}_b$  removed in Figure 4.5. In §4.3, we outline how important accurate measurements of  $T_{0,x}$  are to effectively understanding these variations and performing subsequent timing; therefore, we include all of the above measurements of  $T_{0,x}$  in Table 4.1.

We also include the power spectral density (PSD) for the  $T_0$  deviations for each system computed using a Lomb-Scargle periodogram (Scargle, 1982; Astropy Collaboration et al., 2013, 2018, 2022) in Figure 4.3. The slope of these PSDs is the spectral

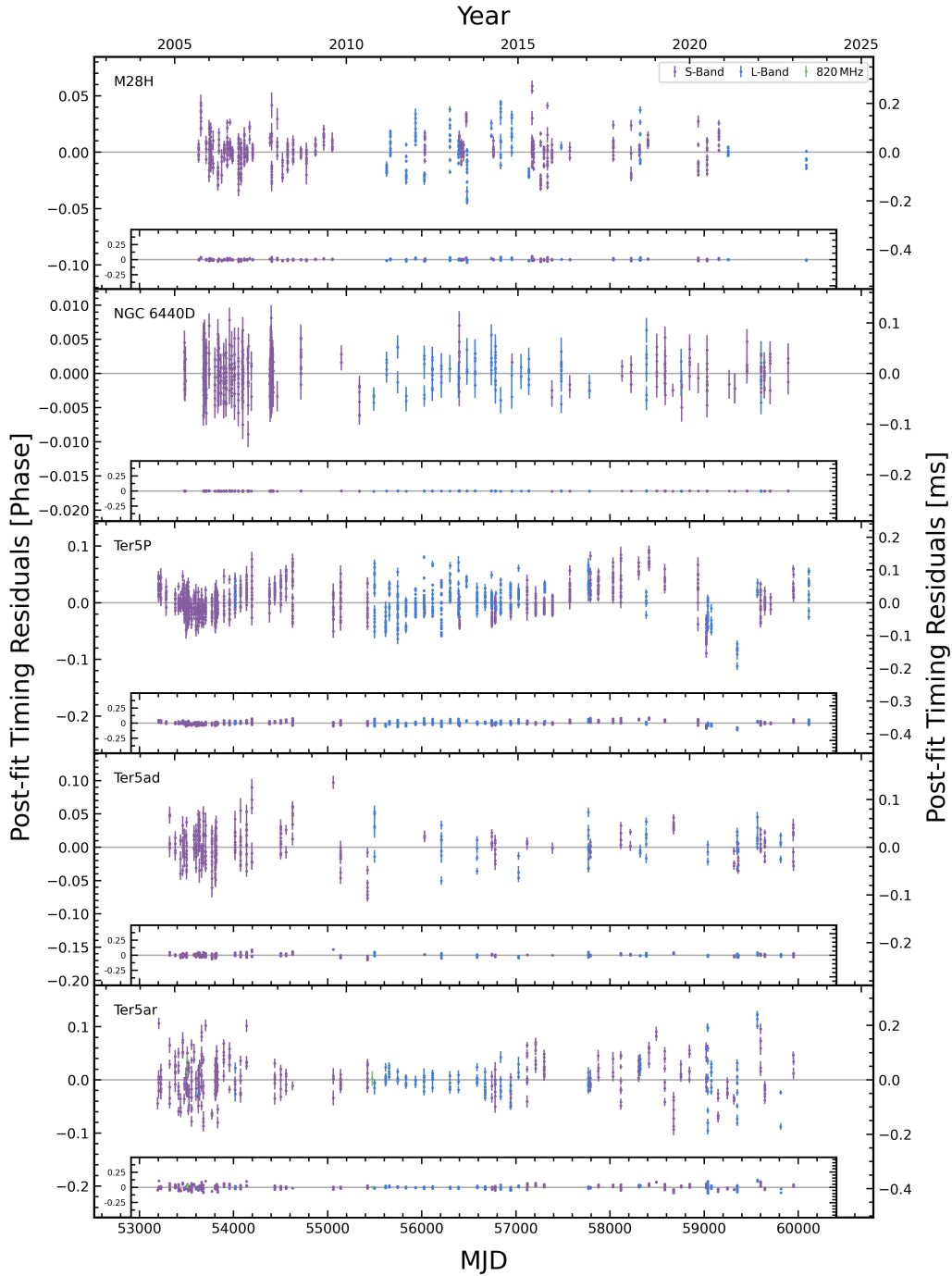


Figure 4.4: Timing residuals for the five RBs described in this work after applying the ROI technique. We note that the errors shown here are our *measured* uncertainties from §4.3.7, not the inflated errors used to measure the spin properties in §4.3.8. Each inset plot shows the same data, but with axes noting  $\pm 0.5$  pulse phase to highlight how close to zero the residuals are.

index,  $\gamma$ , of the orbital phase variations, meaning it may contain information relating to the underlying mechanisms that drive change to the orbital period. Shown are the results of power-law fits to the frequency bins between the bins partially covariant with  $\dot{P}_b$  and the bins associated with white noise. The best-fit  $\gamma$  and its error are shown in the upper right of each plot.

### 4.4.3 Long-term Timing Solutions

Timing residuals from our fully-phase-connected timing solutions for the spin behavior of each RB after performing the ROI technique and fitting are shown in Figure 4.4. The resultant parameters for each system are given in Tables 4.2 & 4.3. Despite the significant systematics posed by the orbit and circumbinary material, we are still able to very accurately measure the spin properties of the MSPs over nearly 20 years.

## 4.5 DISCUSSION

The success of the ROI technique in allowing for long-term descriptions of MSP spin behavior marks a significant step in the pursuit of timing pulsars in RBs with dramatic orbital variations. Even in the presence of large systematics, this novel method allows us to account for each MSP's rotation over nearly 20 years.

### 4.5.1 Applegate Model Applied to Ter5P

The Applegate mechanism (Applegate, 1992) is the most common theory of how variations in a companion star can be used to describe periodic orbital variations in RBs and other compact binaries, and it has been shown to describe at least one eclipsing MSP (e.g., PSR B1957+20, which has a  $\Delta P/P = 1.6 \times 10^{-7}$ ; Arzoumanian et al., 1994; Applegate & Shaham, 1994). In the model, the gravitational quadrupole moment of the companion star can change, perhaps due to magnetic activity, and this can couple with the orbital period and give rise to variations. Examining Figure 4.5a

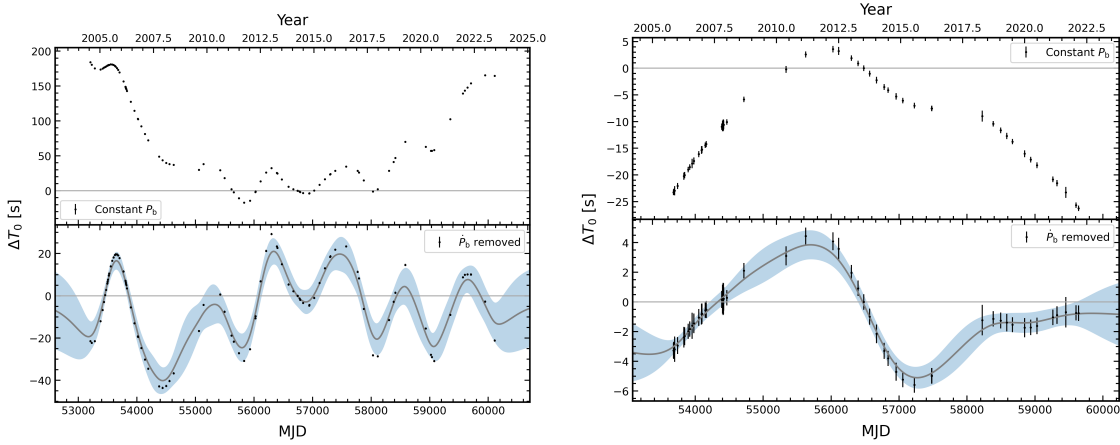


Figure 4.5: Phase variation ( $\Delta T_0$ ) trends over time for Ter5P (left) and NGC 6440D (right) assuming a constant orbital period (upper panels) and after the removal of the best-fit  $\dot{P}_b$  (lower panels). Also shown in the bottom panels are Gaussian process regressions to the measured  $T_{0,x}$  values. The quasi-periodic oscillations described in §4.5.1 for Ter5P are evident.

with the  $\dot{P}_b$  removed, it is possible that quasi-periodic oscillations consistent with the Applegate mechanism might be present in the observed variations of Ter5P. We fit a simple sine wave to the portion of the data above MJD=57500, and from this fit we derive a semi-amplitude of 22.4 s and  $P_{\text{mod}}$  of  $\sim 1033$  d. Using Equation 38 in Applegate (1992), this gives  $\Delta P/P = 1.6 \times 10^{-6}$ . However, it is clear that both the modulation amplitude and period are not constant over the baseline of our observations. It is also plausible that there are additional or even alternative mechanisms (such as the quadrupole moment of the gravity field of the pulsar’s companion; see Appendix 4.7) responsible for the variations that are seen here, especially since we removed a large  $\dot{P}_b$  value to uncover them. In any case, this appears to be the first spider pulsar to show many cycles of a quasi-periodic oscillation.

### 4.5.2 Timing Solutions

The small dispersion in each of the timing residuals in Figure 4.4 shows that the noise in the orbits of these system does not necessarily strongly affect the clock of the MSP’s spin. Our data are well described by solutions containing astrometry, as well as small numbers of frequency derivatives – where derivatives after  $\dot{f}$  are expected due to the accelerations of the cluster (Phinney, 1992, 1993; Freire et al., 2017; Prager et al., 2017). Some of the variations present in the post-fit residuals are almost certainly a manifestation of  $T_{0,x}$  values that are still not yet accurate enough to describe the local solution (e.g., the TOAs around MJD $\sim$ 56600 in M28H). It is important to point out that variations caused by other mechanisms are still present in these systems, though. Small duration eclipses will cause issues with the TOAs by affecting the DM value in that observation. Infalling material can also cause a torque on the MSP’s magnetosphere that will affect the spin. These variations are clear in the timing solution for Ter5P (the most dramatic around MJD $\sim$ 59400), where efforts to further improve the local variations as well as additional frequency derivatives in the timing model failed to remove these sharp features. Similar features are also seen in the long-term timing solution of Ter5A (Rosenthal et al., 2024). A torque from the material would affect the pulsar as a second derivative change in rotational phase:

$$\tau = I \frac{d^2\phi}{dt^2}. \quad (4.5)$$

These torques are likely present at small levels in all of our timing solutions, but the exact magnitude and cause of them likely varies greatly system to system. It is not clear whether the torques would be caused by effects from the companion or nearby stars.

### 4.5.3 Positions and Proper Motions

We fit for right ascension ( $\alpha$ ), declination ( $\delta$ ), and the proper motion only in  $\alpha$  ( $\mu_\alpha$ ) in all analyses of the isolated TOAs (see §4.3.8). Initial assessments of fits allowing proper motion in  $\delta$  ( $\mu_\delta$ ) to vary yield nonsensical measurements, likely due to the low ecliptic latitudes  $|\beta| \lesssim 3^\circ$  of these globular clusters, where pulsar timing has much less power measuring declination; therefore, we include  $\mu_\delta$  as a fixed value of 0 in our fits. The sensitivity to  $\delta$  and by extension  $\mu_\delta$  in fits of long baseline TOAs are inherently less precise than those of  $\alpha$  for these pulsars, and the large systematics imposed by the phase variations compound to make measurements of  $\mu_\delta$  exceedingly difficult. Future work and additional observations could seek to improve upon this.

As a consistency check, we compare our positions to those of both radio and X-ray positions for each system where available. M28H has both radio and X-ray (Vurgun et al., 2022) positions. We cannot draw any conclusions on the consistency with the cited positions as the reported uncertainties are too small to be feasibly correct; however, our  $\alpha$  and  $\delta$  differ from the reported values of  $\alpha = 18:24:31.61052125$  &  $\delta = -24:52:17.2268378$  by only 0.7 and 760 mas, respectively. Our values are consistent within errors with the reported X-ray positions. Freire et al. (2008) reports radio-timing positions of  $\alpha = 17:48:51.64665(7)$  and  $\delta = -20:21:07.414(18)$  for NGC 6440D, and our  $\delta$  value is entirely consistent with that result. Our  $\alpha$  is not consistent within errors, but as was the case with M28H, our value differs by only 0.95 mas. Some of the systems in Ter5 have radio positions from Urquhart et al. (2020). Our measurement of both  $\alpha$  and  $\delta$  for Ter5P and Ter5ar are consistent within errors with the reported values (VLA5 and VLA38, respectively). Ter5P and Ter5ad have X-ray positions from Bogdanov et al. (2021) that are consistent within errors with our measured values. Bahramian et al. (2020) report positions for CXOU J174804.63–244645.2, which

Padmanabh et al. (2024) identified as being consistent with Ter5ar. The positions we measure for Ter5ar are not consistent within error with the reported values of  $\alpha = 17:48:04.63(13)$  and  $\delta = -24:46:45.34(13)$ ; however, the uncertainties are based off of source extraction via centroiding that may not represent the uncertainties of a dedicated measurement of the X-ray position. Given that our measurements differ by only 10 and 530 mas in  $\alpha$  and  $\delta$ , respectively, it is likely these values would be consistent with uncertainties produced with Hong et al.'s (2005) expression for 95% confidence error circles such as those in Bogdanov et al. (2021).

Similarly, we compared our measured  $\mu_\alpha$  to those measured for each GC by Vasiliev & Baumgardt (2021) using *Gaia*. The reported values for M28, NGC 6440D, and Ter5 are  $-0.278 \pm 0.028$ ,  $-1.187 \pm 0.036$ ,  $-1.989 \pm 0.068$  mas yr<sup>-1</sup>, respectively. As shown in Tables 4.2 & 4.3, our measurements for NGC 6440D and Ter5ad are consistent within errors with the reported values, while our measurements for M28H, Ter5P, and Ter5ar are not. These values are relatively reasonable given the proper motions of stars in the cluster within an order of magnitude or two, though, and our measurement for Ter5P only differs by 0.189 mas yr<sup>-1</sup>. As with  $\mu_\delta$ , our measurements of  $\mu_\alpha$  are likely substantially affected by the systematics of the phase variations. The relative closeness of our measurements are a sign that improvements to the ROI technique in the future may yield accurate  $\mu_\alpha$  measurements.

#### 4.5.4 ROI Timing vs. Traditional Timing

In Figure 4.6 we show a comparison of our long-term timing solution for NGC 6440D created via ROI and the long-term timing solution from Ransom et al. (in prep). The latter solution contains nine orbital frequency derivatives conventionally used for timing. NGC 6440D is by many measures the most well-behaved of the systems in our sample, having orbital variations with far less drastic affects on the

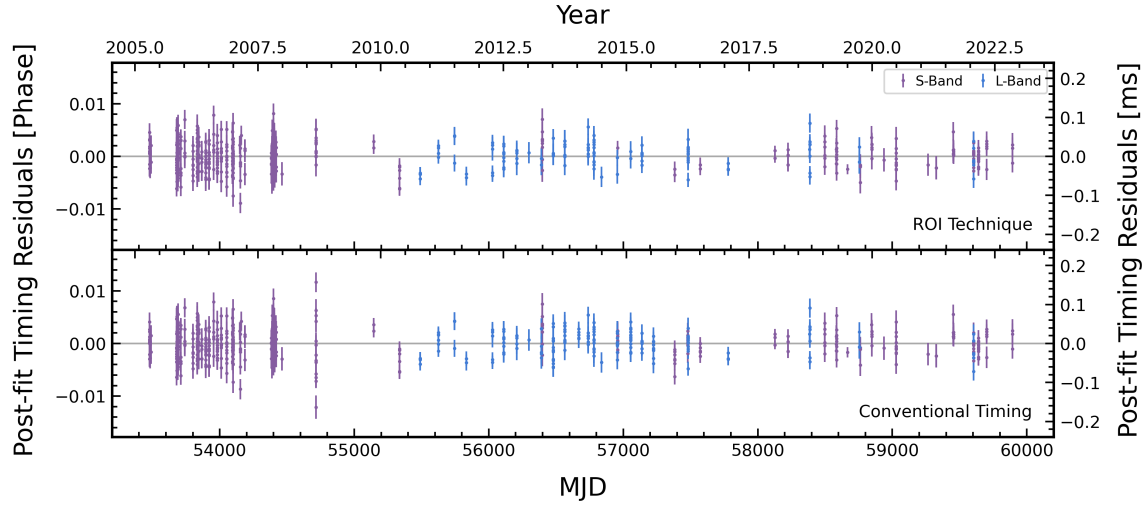


Figure 4.6: Comparison of timing residuals obtained via the ROI technique (top) and those obtained using conventional timing techniques (bottom). It is clear that these two methods yield nearly identical results.

observations. The results of both methods look to be nearly identical, which is a useful check on the efficacy of the ROI technique.

We stress that this is not to say that conventional timing techniques should not be used to derive long-term solutions for RBs. Rather we highlight that for systems with significant orbital variations there are useful benefits that our technique provides over conventional methods. Conventional-timing techniques necessitate  $P_b$  and nine orbital frequency derivatives to describe the binary effects of NGC 6440D and the effects of the cluster, whereas the ROI technique produces nearly identical results with a simple model to remove binary information entirely. Similarly, higher-order, orbital frequency derivatives poorly predict orbital behavior in large gaps between observations, while the stable spin of the MSP – the connecting factor in our method – extrapolates nicely over those same gaps. Thus, the ROI technique produces nearly identical results by trading orbital frequency derivatives for a number of individual, well-measured  $T_{0,x}$  values needed to accurately describe the long-term timing behavior

of the systems.

### 4.5.5 Phase Variation Analyses

We analyze a small set of parameters to search for any potential covariances that could yield insights into the phase variations seen in RBs. First, we inspected our  $\gamma$  values, by comparing them against the spin frequency and period,  $P_b$ , and semi-major axis for each system. We see no evidence of covariance in any of these parameters. However, as shown in the left panel of Figure 4.7, it is of note that our  $\gamma$  values are all greater than those of the three systems presented in Thongmeearkom et al. (2024), which have  $\gamma < -2.4$ ,  $\gamma = -3.81^{+0.32}_{-0.48}$ , and  $\gamma < -5.4$ , but similar to the  $\gamma = -0.9 \pm 0.2$  for Ter5A from Rosenthal et al. (2024). This may simply mean that the observed variations in our systems may not exist in a power-law regime.

We also inspected the standard deviation of the phase variations ( $\sigma_{\Delta T_0}$ ) as a fraction of the orbital period. This experiment was to see if, fractionally, the observed variations were similar or if some systems have higher variations than others. In Figure 4.7, we show the fractional deviation ( $\sigma_{\Delta T_0}/P_b$ ) plotted against spin frequency and period,  $P_b$ , and semi-major axis. Immediately evident was the correlation  $\sigma_{\Delta T_0}/P_b$  has with spin frequency (and inversely with spin period) and potentially with the projected semi-major axis. Although there is more noise in the trend, it is clear that, as the binary distance tightens, the fractional deviation in the phase variations becomes less drastic. The near direct relationship with spin frequency is certainly the most striking.

It is unclear what the physical mechanism for this relationship would be. Younger MSPs that have just been spun up by their binary companion may have the fastest spins and be closer to the point where they overflowed their Roche lobe to contribute the material for spinning up the pulsar. This could mean more material would be

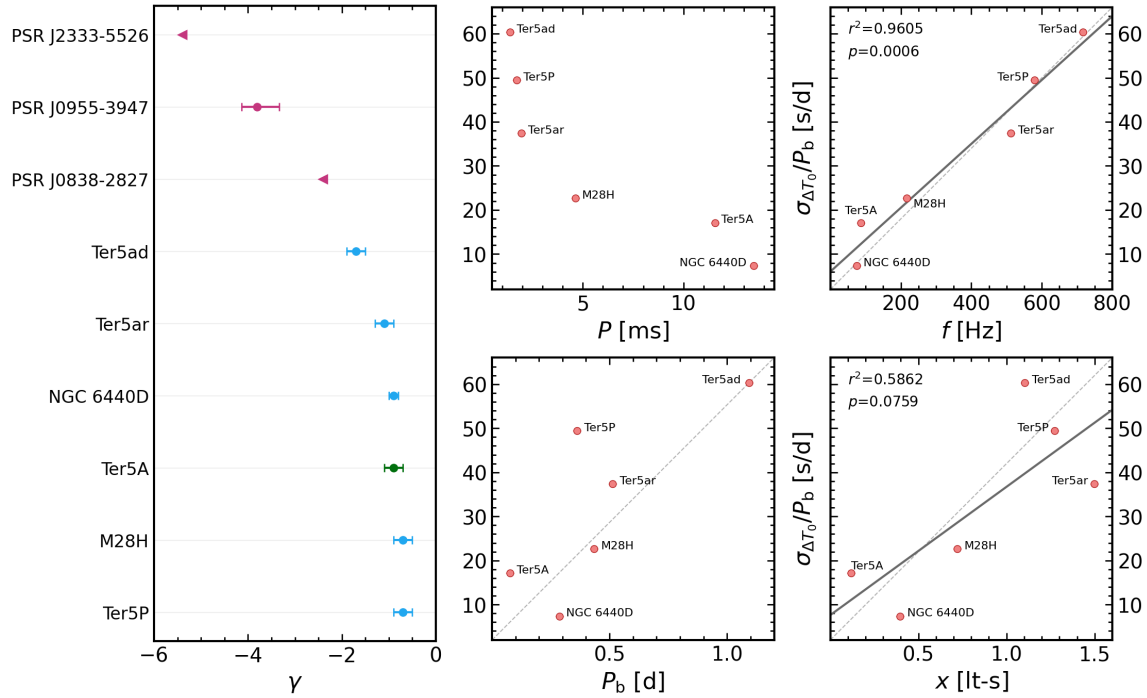


Figure 4.7: *Left*: All currently measured  $\gamma$  values for RBs. Values from this work are shown in blue, the value for Ter5A from Rosenthal et al. (2024) is shown in green, and the three values from Thongmeearkom et al. (2024) are shown in pink. Upper limits are plotted as triangles. *Right*: The fractional deviation of the five RBs described here, as well as Ter5A, plotted against spin period (upper left), spin frequency (upper right), orbital period (bottom left), and projected semi-major axis (bottom right). Values for Ter5A come from analysis presented in Rosenthal et al. (2024). Also plotted as a solid line is a linear regression fit for the strong correlation seen with spin frequency and the weaker one with projected semi-major axis, as well as the regression’s  $r^2$  and  $p$ -values. The light-gray, dashed lines in each plot show the one-to-one line for that variable.

present to perturb the system, more interactions would be taking place as the pulsar finishes its spin up, or both. Older and slower MSPs would be then be farther from this evolutionary stage and more settled, and thus may not be prone to large variations. Owing to the precise nature of the ROI technique, it is possible that this is a manifestation of the sensitivity of our  $T_{0,x}$  measurements, where the more rapidly a system is rotating, the more accurate the values of  $T_{0,x}$  need to be. Future long-term studies of these systems may be able to disentangle the physical reasoning behind these strong trends, assuming they are not byproducts of small statistics.

#### 4.5.6 Mitigating Systematics in the Future

As has been mentioned throughout the text, there are systematics present in these datasets that serve as contaminants. We are able to remove a good portion of them through the ROI technique; however, it is not to be assumed that they are gone at this point. While it is likely not possible to account for every variation caused by the eclipses, gas in the system, or any torques imposed by accreted material, finding more ways to even further improve the  $T_{0,x}$  measurement for a piecewise group can in fact go a long way to mitigate local systematics. One simple addition to the ROI technique for future studies could be to implement a simple routine that finds a  $T_{0,x}$  that both minimizes the dispersion of TOAs in post-fit phase and keeps the group close to a long-term trend line of the isolated TOAs. We also reiterate that our analysis was conducted using time-series data, as it keeps the problem at hand far simpler to address. Future studies will be able to leverage the multi-frequency information of raw data to account for DM variations and delays in certain observations. These variations are likely some of the largest contaminants to measurements of  $T_{0,x}$ , and our analysis of the time-series data only removes a small fraction of them by removing TOAs near the eclipse.

## 4.6 SUMMARY

We have presented a novel technique for “isolating” the underlying MSP clock in binaries with dramatic orbital variations by removing the timing delays from the binary orbit and fitting local variations in the TOAs. This technique allows for phase connection over baselines that far surpass those of the initial solutions containing binary information. We used this technique to get timing solutions for five RB systems found in three GCs spanning almost two decades. The results of our solutions derived from isolated TOAs are consistent with those derived from conventional timing techniques for GC pulsars, meaning this is an effective alternative for systems that show large phase variations. Variations seen in the five systems we investigated show the broad spectrum of systematics present in RBs, ranging from relatively well behaved (e.g., NGC 6440D) to quasi-periodic (e.g, Ter5P) to unpredictable (e.g, M28H & Ter5ar). An analysis of Ter5P shows that it is possible that its oscillations arise from the Applegate mechanism; however, the changing nature of the oscillations may necessitate additional or alternative mechanisms to fully describe the phase variations. A striking correlation exists between the standard deviation of a system’s variations as a fraction of its orbital period and its spin frequency. Whether this is a probe of the MSPs age since being spun up, the inherent susceptibility of an MSP to perturbations based on its spin, or even just a manifestation of the need for duly accurate measurements of phase, it is clear that future studies of RBs will need to continue this investigation. The nature of RB timing is riddled with pervasive systematics that limit our ability to describe these systems in ways other MSP binaries can be over similar baselines. With refinement to the ROI technique, multi-frequency information, and more systems with long baselines, though, it is still possible to investigate interesting physics problems with these unique binaries.

## 4.7 APPENDIX: DYNAMICAL CONSIDERATIONS

In this work, we have assumed that the dominant systematic in our timing analysis is changes to the time of periastron passage (i.e.,  $\Delta T_0$ ). Empirically, this assumption yields good results, and the addition of DM effect modeling in future implementations will further improve the method's performance. However, from a dynamics perspective, it is unclear if  $\Delta T_0$  can be the sole orbital element responsible for observed timing variations. In the text that follows, we outline some dynamical considerations that could be useful in investigating this further. For additional commentary detailing how some equations here relate to studies of MSPs in GCs, see Prager (2017) when they are originally presented.

### 4.7.1 Relating $T_0$ to $P_b$ & $\dot{P}_b$

For investigations of the orbital period, we relate changes in orbital phase to changes in  $T_0$  as follows:

$$\Delta\phi = n\Delta T_0 = \frac{2\pi}{P_b}\Delta T_0, \quad (4.6)$$

where  $n$  is the orbital frequency ( $n = 2\pi/P_b$ ). When considering a changing orbital period, we can similarly express the change in orbital phase in terms of:

$$\Delta\phi = \frac{1}{2}\dot{n}\Delta t^2 = \frac{-\pi\dot{P}_b}{P_b^2}\Delta t^2, \quad (4.7)$$

which relates the characteristic change in  $P_b$  to the observed  $T_0$  wander over the timescale  $\Delta t$  through

$$\frac{\Delta P_b}{P_b} \sim 2\frac{\Delta T_0}{\Delta t}. \quad (4.8)$$

The characteristic orbital period derivative is then:

$$\dot{P}_b \simeq \frac{\Delta P_b}{\Delta t} = 2P_b \frac{\Delta T_0}{\Delta t^2}. \quad (4.9)$$

### 4.7.2 Relating $T_0$ to $x$

For our analyses, we assumed that the semi-major axis is constant over the duration of our baseline, attributing all orbital changes to the time of periastron passage,  $T_0$ . For investigations interested in investigating this assumption, we give a relationship between the  $T_0$  and the projected-semi-major axis,  $x$ . From Kepler's third law, the shrinking of the pulsar orbit by gravitational wave damping relates the change in  $x$  to  $\dot{P}_b$  as:

$$\frac{\dot{x}}{x} = \frac{2 \dot{P}_b}{3 P_b}. \quad (4.10)$$

Replacing  $\dot{P}_b$  with the result of Equation 4.9, this becomes:

$$\dot{x} = \frac{4}{3} x \frac{\Delta T_0}{\Delta t^2}. \quad (4.11)$$

Similarly to  $\dot{P}_b$ , the characteristic change in  $x$  is then:

$$\dot{x} = \frac{4}{3} x \frac{\Delta T_0}{\Delta t^2} \simeq \frac{\Delta x}{\Delta t}. \quad (4.12)$$

Rearranging Equation 4.12, we get the relationship:

$$\Delta T_0 \simeq \frac{3}{4} \frac{\Delta t}{x} \Delta x. \quad (4.13)$$

### 4.7.3 Quadrupole Moments

In §4.5.1, we investigated the viability of the Applegate model to describe the quasi-periodic  $T_0$  oscillations present in Ter5P. As an alternative explanation for the observed variations, we relate the change in  $T_0$  to the quadrupole moment of the gravity field of the pulsar's companion. Beginning with an axisymmetric potential, the field is given by:

$$\Phi = -\frac{GM_c}{r} - GM_c \sum_{l=2}^{\infty} J_l \left( \frac{R_c^l}{r^{l+1}} \right) P_l(\cos \theta), \quad (4.14)$$

where  $J$  is the multipole moment,  $R_c$  is the radius of the companion star, and  $P_l$  is the Legendre polynomial. For  $\cos \theta = 0$ , the force due to the potential is then:

$$\frac{d\Phi}{dr} = \frac{GM_c}{r^2} + \frac{GM_c}{r_c^2} \sum_{l=2}^{\infty} (l+1) J_l \left( \frac{R_c}{r} \right)^l P_l(0). \quad (4.15)$$

We define the orbital frequency to be  $n = 2\pi/P_b$  and, using the assumption that the companion star is filling its Roche lobe by some factor  $\kappa$  with  $R_c = \kappa R_l$ , we simplify Equation 4.15 to be:

$$n^2 r = \frac{GM}{r^2} \left[ 1 + \sum_{l=2}^{\infty} (l+1) J_l \left( \frac{\kappa R_l}{r} \right)^l P_l(0) \right], \quad (4.16)$$

where  $n^2 r = d\Phi/dr$ . Limiting to the contributions of the quadrupolar moment ( $J_2$ ),  $n$  becomes:

$$n = \sqrt{\frac{GM}{r^3}} \left[ 1 - \frac{3}{2} J_2 \left( \frac{\kappa R_l}{r} \right)^2 \right]^{1/2}. \quad (4.17)$$

The angular momentum in an axisymmetric potential must be constant such that

$$l_z = r^2 \frac{d\phi}{dt} = r^2 n \simeq \sqrt{GMr} \left[ 1 - \frac{3}{4} J_2 \left( \frac{\kappa R_l}{r} \right)^2 \right], \quad (4.18)$$

where  $\phi$  is the orbital phase and we have Taylor expanded the orbital frequency out to first order. If we perturb  $r$  by some factor,  $\delta r$ , we have

$$r = \bar{r} + \delta r, \quad (4.19)$$

where  $\bar{r}$  is the average orbital separation. Using this, Equation 4.18 becomes a function of  $\bar{r}$  and  $n$  as:

$$l_z = \bar{r}^2 \bar{n} \simeq \sqrt{GM\bar{r}} \left[ 1 - \frac{3}{4} J_2 \left( \frac{\kappa R_l}{\bar{r}} \right)^2 \right]. \quad (4.20)$$

Now if we allow  $J_2$  to vary, we are left with:

$$0 = \sqrt{GM\bar{r}} \left[ \frac{1}{2} \frac{\delta r}{\bar{r}} - \frac{3}{4} \delta J_2 \left( \frac{\kappa R_l}{\bar{r}} \right)^2 \right]. \quad (4.21)$$

We can then express the fractional change in the orbital separation and the orbital frequency as:

$$\frac{\delta r}{\bar{r}} = \frac{3}{2} \delta J_2 \left( \frac{\kappa R_l}{\bar{r}} \right)^2, \quad (4.22)$$

which gives

$$\frac{\delta n}{\bar{n}} = -2 \frac{\delta r}{\bar{r}} = -3 \delta J_2 \left( \frac{\kappa R_l}{\bar{r}} \right)^2. \quad (4.23)$$

If we use Equation 4.23, we can then express the change in  $T_0$  as a function of  $J_2$ . We first find the integrated change in phase over a period of time,  $t$  due to the perturbed

frequency:

$$\Delta\phi = \int_0^t dt' \delta n(t') = \bar{n} dt' \left[ -3\delta J_2(t') \left( \frac{\kappa R_l}{\bar{r}} \right)^2 \right]. \quad (4.24)$$

Time averaging Equation 4.24 yields

$$\frac{\Delta\phi}{n\Delta t} = -3\delta\bar{J}_2(t) \left( \frac{\kappa R_l}{\bar{r}} \right)^2. \quad (4.25)$$

Combining Equation 4.25 with Equation 4.6 yields a formula relating the observed changes  $T_0$  to  $J_2$  such that:

$$\frac{\Delta T_0}{\Delta t} = 3\delta\bar{J}_2(t) \left( \frac{\kappa R_l}{\bar{r}} \right)^2. \quad (4.26)$$

For our specific case, this equation then becomes

$$\frac{\Delta T_0}{\Delta t} = 3\delta\bar{J}_2(t) \left( \frac{R_c}{\bar{R}} \right)^2, \quad (4.27)$$

where  $\delta\bar{J}_2(t)$  is the average change in the quadrupole moment,  $R_c$  is the companion radius, and  $\bar{R}$  is the separation between the pulsar and the companion star calculated such that:

$$R = x_{p,i} \left( 1 + \frac{M_p}{M_{c,\min}} \right) c. \quad (4.28)$$

## 4.8 APPENDIX: SUPPLEMENTARY TABLES

Included here are tables for data and fits used throughout the text. In Table 4.1 we provide the  $T_{0,x}$  values used for our binary-piecewise groups. These values should be taken as a starting place for future analyses of these systems. In Tables 4.2 and 4.3 we provide all of the binary information used to remove the orbital timing delays from

each system as well as the parameters from our timing models of the spin behaviors.

Table 4.1: The final measurements of  $T_{0,x}$  used in constructing the piecewise-continuous groups for each system.

Group	M28H	NGC 6440D	Ter5P	Ter5ad	Ter5ar
#	$T_0$ [MJD]				
1	53629.9385207(54)	53478.316129(25)	53204.18393645(17)	53252.23546037(89)	53205.2380510(25)
2	53651.254881(15)	53483.179297(65)	53227.39148316(39)	53320.0901308(32)	53206.26472831(87)
3	53707.8084219(91)	53489.47281(14)	53282.1468202(12)	53379.189373(13)	53216.01816206(60)
4	53739.130384(38)	53679.99454845(94)	53378.9659555(14)	53435.005329(14)	53227.3116125(11)
5	53753.9213147(12)	53681.7109605(15)	53415.22782516(67)	53457.98837(14)	53229.3649678(18)
6	53755.66142441(40)	53681.9970292(34)	53439.1606633(14)	53474.404824(18)	53320.22591517(53)
7	53756.9665067(91)	53683.7134413(18)	53459.1046954(14)	53495.1990014(10)	53379.7732062(12)
8	53757.8365616(17)	53685.7159220(16)	53475.0599204(36)	53500.6711532(16)	53414.68023902(50)
9	53759.141644(34)	53687.718403(22)	53493.55347757(39)	53579.4701322(44)	53434.7004489(65)
10	53781.76307(11)	53690.8651583(19)	53496.0918081(11)	53601.3587350(14)	53438.80715862(55)
11	53832.6613151(60)	53696.0143945(81)	53500.44323289(24)	53625.4361957(17)	53458.82736894(93)
12	53844.407066(61)	53709.745691(40)	53506.60775125(21)	53637.474927(36)	53474.227529(17)
13	53872.683875(37)	53709.745691(37)	53520.02464341(23)	53637.474927(18)	53493.73439988(96)
14	53902.26577032(74)	53740.6411085(32)	53526.55177969(20)	53659.3635263(19)	53496.30109(45)
15	53932.28269427(72)	53801.287669(62)	53553.38555898(27)	53679.0632656(20)	53501.43448085(78)
16	53962.2996186(11)	53801.573737(28)	53579.8567112(11)	53703.1407239(22)	53506.5678671(16)
17	53987.96626479(88)	53833.3273607(56)	53601.25119817(40)	53769.9009444(12)	53507.5945451(28)
18	54052.78542310(77)	53833.6134294(31)	53625.18400663(33)	53803.8282678(13)	53526.5880762(13)
19	54074.9718466(11)	53843.3397645(39)	53638.6008805(18)	53804.9226976(22)	53533.77481757(78)
20	54079.75715425(75)	53865.367053(39)	53659.63273154(84)	53806.017127(11)	53554.30836398(40)
21	54114.5593874(23)	53895.11820(34)	53679.57672240(44)	53810.394847(29)	53579.461957(13)
22	54144.57631255(78)	53895.4042642(11)	53703.50950421(20)	53814.7725655(12)	53602.0488562(37)
23	54169.807929(43)	53920.2922392(15)	53769.86854919(16)	54016.1476506(15)	53625.14909317(57)
24	54202.4350143(10)	53955.1926179(84)	53803.59198568(20)	54074.1524401(18)	53625.66243175(64)
25	54386.88664719(84)	53980.9387988(51)	53804.67983887(39)	54138.7238191(21)	53639.0092353(12)
26	54405.1577859(65)	53981.2248674(25)	53805.76769160(20)	54194.5397633(38)	53660.05611565(62)
27	54465.19152(18)	54010.976010(14)	53811.20695520(65)	54500.9803277(11)	53679.04964135(67)
28	54520.004932(11)	54010.97601(16)	53815.19574799(34)	54556.796287(22)	53703.17655098(73)
29	54574.38333165(93)	54050.7395554(32)	53819.54715879(16)	54625.745400(11)	53769.9105473(44)
30	54632.2419688(18)	54093.6498562(58)	53830.78830373(76)	55058.0451269(12)	53804.8175548(19)
31	54715.3322170(31)	54095.6523369(35)	53896.42208417(51)	55136.8440094(81)	53805.3308931(80)
32	54773.1908713(95)	54098.7990923(55)	53957.34184827(28)	55423.5842712(30)	53805.84423(11)
33	54871.0720237(86)	54099.6572983(38)	54016.08591876(19)	55496.9109732(70)	53811.4909528(27)

CHAPTER 4. LONG-TERM TIMING OF REDBACK MILLISECOND PULSARS IN  
GLOBULAR CLUSTERS

116

34	54957.6424492(38)	54099.657298(14)	54018.62424305(94)	56028.803303(13)	53815.59765935(46)
35	55048.5631694(75)	54148.5750408(15)	54074.46738141(38)	56207.1949872(16)	53819.70436542(79)
36	55625.4094764(43)	54153.438208(24)	54138.65073591(29)	56588.0557186(48)	53829.97113088(95)
37	55664.56195259(61)	54160.5899248(34)	54194.49388733(47)	56745.6533882(18)	53897.2184807(26)
38	55833.7876745(14)	54187.480380(34)	54380.15431237(37)	56778.4862517(19)	53957.27904429(98)
39	55932.5389399(19)	54383.723481(18)	54438.53583792(23)	57026.9214416(40)	54016.31291936(65)
40	56026.5048941(99)	54388.872716(97)	54500.90618449(26)	57118.853363(42)	54017.339595(20)
41	56032.5952797(13)	54390.8751970(34)	54557.11203850(57)	57388.0825864(73)	54074.8334548(22)
42	56298.8320989(10)	54398.8851194(28)	54626.37216650(15)	57770.0376157(17)	54139.00072730(58)
43	56390.62289484(77)	54402.0318746(98)	55057.88815504(46)	57791.9261454(15)	54438.7902578(11)
44	56397.5833346(12)	54404.606492(35)	55136.93909113(38)	58113.6875807(49)	54500.9041975(31)
45	56418.4646542(21)	54406.0368357(75)	55423.04502125(36)	58215.469372(10)	54557.371412(14)
46	56421.5098467(85)	54408.897522(11)	55496.65645520(22)	58320.5344765(64)	54627.18543776(44)
47	56443.2612220(43)	54416.907445(11)	55614.50729843(35)	58385.1057517(27)	55058.389480(10)
48	56471.102983(20)	54419.7681312(71)	55653.30743345(13)	58676.2238832(41)	55137.95685828(45)
49	56479.36850580(72)	54463.5366351(17)	55743.23673378(17)	59037.3857265(58)	55423.3726304(14)
50	56738.6449081(70)	54714.9909962(15)	55829.90249209(13)	59146.828722(66)	55473.16638388(77)
51	56759.5262106(42)	55144.666093(59)	55931.435715350(52)	59317.5597674(69)	55496.7799150(69)
52	56837.39614888(80)	55336.3320909(47)	56023.178350109(53)	59351.4870831(14)	55614.8475620(14)
53	56956.1586525(39)	55489.950956(25)	56028.25501932(28)	59362.4313778(11)	55653.3478840(38)
54	57137.5650962(27)	55625.5474924(31)	56113.107928159(62)	59565.9952139(16)	55744.2086697(10)
55	57172.36728814(36)	55743.979907(30)	56206.663658990(57)	59599.9225153(11)	55829.93609672(77)
56	57186.2881646(17)	55833.805455(24)	56299.49408154(13)	59644.7941078(12)	55931.5769912(83)
57	57187.158219(59)	56026.3296321(39)	56389.42339918(15)	59814.4306563(16)	56023.46444506(70)
58	57261.98292717(47)	56111.2920066(65)	56399.21408991(27)	59947.9510930(19)	56112.78521260(35)
59	57297.2201417(17)	56207.697123(23)	56474.2760313(14)		56299.6402657(27)
60	57333.76243713(41)	56298.3808647(18)	56587.77551551(17)		56389.4744682(18)
61	57382.9205236(13)	56390.494948(27)	56671.54035858(18)		56587.62313967(64)
62	57482.97680593(53)	56397.3605938(19)	56742.25094883(10)		56671.29733409(34)
63	57574.332557(16)	56479.1762070(18)	56745.151897270(95)		56745.2180710(28)
64	58034.5917351(20)	56565.8549853(24)	56778.150170296(93)		56778.07171593(69)
65	58224.263641(60)	56668.5536037(44)	56787.2156265(31)		56838.1322731(19)
66	58313.009213(11)	56738.354336(18)	56837.98220724(13)		56941.8265555(32)
67	58320.8397053(16)	56781.2646226(25)	56941.691102344(90)		56943.8799059(11)
68	58401.7547898(19)	56837.0479954(15)	56943.86681720(26)		57026.527250(36)
69	58937.2735506(36)	56955.7664570(40)	57026.54389180(17)		57119.44131923(56)
70	59029.4994048(23)	56957.7689371(31)	57119.37433252(49)		57209.2754125(11)
71	59156.96251753(89)	57055.6043941(16)	57209.30382670(15)		57299.62286626(52)
72	59255.71383447(71)	57137.133943(18)	57299.595923627(66)		57387.4036938(42)

CHAPTER 4. LONG-TERM TIMING OF REDBACK MILLISECOND PULSARS IN  
 GLOBULAR CLUSTERS

73	60084.4415596(26)	57224.0987970(19)	57306.12306245(14)	57573.2320873(19)
74		57382.580804(12)	57387.712290037(85)	57769.32723824(31)
75		57480.4162691(17)	57573.01043610(22)	57791.400786(10)
76		57482.4187494(17)	57769.54961759(21)	57875.0749152(29)
77		57571.958225(19)	57791.66932139(23)	58030.6163945(21)
78		57779.357971(28)	57875.07145397(13)	58113.77717324(39)
79		58127.503465(12)	58030.99724588(19)	58305.2522899(10)
80		58224.480718(10)	58113.67431029(38)	58320.1390987(16)
81		58385.8233995(14)	58305.1372071(12)	58412.5399472(14)
82		58386.9676739(16)	58384.9134355(16)	58491.593995(11)
83		58496.8180077(23)	58412.8351305(14)	58582.45486735(75)
84		58582.352511(19)	58582.1782558(12)	58675.8824303(18)
85		58585.4992656(36)	58933.19292746(61)	58753.9098546(79)
86		58586.357471(23)	59020.94654577(18)	58844.7707124(12)
87		58668.17308301(75)	59036.90176275(19)	59020.84561611(69)
88		58754.851860(46)	59076.06457880(74)	59037.27243050(41)
89		58760.859300(72)	59351.29256505(59)	59075.77276022(81)
90		58846.6798719(48)	59565.6005516(11)	59146.6133467(18)
91		58937.3636098(19)	59599.68674527(20)	59246.71413578(97)
92		59029.1916226(28)	59644.28887715(32)	59317.5547223(18)
93		59264.3399930(18)	59705.2088602(36)	59351.43499999(36)
94		59325.5586680(37)	59947.43818330(32)	59362.2150910(84)
95		59325.5586680(24)	60110.97913770(26)	59565.4968589(40)
96		59454.003456(10)		59599.3771697(16)
97		59604.76158787(98)		59644.55092666(54)
98		59640.5201577(16)		59705.124824(25)
99		59700.308487(29)		59813.9523949(92)
100		59893.976925(16)		59947.4203255(39)

---

Table 4.2: Timing parameters for the RBs in Terzan 5

Parameter	M28H	Ter5ad	Ter5ar
Pulsar Name .....	PSR J1748–2446P	PSR J1748–2446ad	PSR J1748–2446ar
Data Reduction			
Span of Timing Data (MJD) .....	53204–60111	53320–59948	53193–59948
Number of TOAs .....	1536	388	495
RMS TOA Residual ( $\mu$ s) .....	40.7	31.4	66.5
Reduced $\chi^2$ .....	1.01	1.03	1.02
EFAC for incoherent data .....	2.52	2.65	3.47
EFAC for coherent data .....	5.79	4.07	4.86
Timing Parameters			
Right Ascension (RA, J2000) .....	17 <sup>h</sup> 48 <sup>m</sup> 05 <sup>s</sup> 03815(7)	17 <sup>h</sup> 48 <sup>m</sup> 03 <sup>s</sup> 8479(1)	17 <sup>h</sup> 48 <sup>m</sup> 04 <sup>s</sup> 6196(2)
Declination (DEC, J2000) .....	–24° 46′ 41″29(3)	–24° 46′ 41″84(5)	–24° 46′ 45″87(8)
Proper Motion in RA (mas yr <sup>–1</sup> ) ...	–1.8(1)	–2.2(2)	0.3(3)
Pulsar Spin Period (ms) .....	1.72861982757976(9)	1.3959548139683(1)	1.9528106824465(3)
Pulsar Spin Frequency (Hz) .....	578.49619913252(3)	716.35556537627(6)	512.08240972300(8)
Spin Frequency Derivative (Hz s <sup>–1</sup> )	–8.66271(8) × 10 <sup>–14</sup>	1.74117(6) × 10 <sup>–14</sup>	6.76849(7) × 10 <sup>–14</sup>
Frequency 2nd Derivative (Hz s <sup>–2</sup> )	4(2) × 10 <sup>–26</sup>	–4(2) × 10 <sup>–27</sup>	–1.82(3) × 10 <sup>–25</sup>
Frequency 3rd Derivative (Hz s <sup>–3</sup> ) .	–2.5(2) × 10 <sup>–33</sup>	–	–
Frequency 4th Derivative (Hz s <sup>–4</sup> ) .	–4.3(1) × 10 <sup>–41</sup>	–	–
Reference Epoch (PEPOCH, MJD) .	56657.660271337430459	56633.74460856008227	56570.518685778268264
Dispersion Measure (DM, pc cm <sup>–3</sup> )	238.71(1)	235.63(2)	238.66(1)
DM Derivative (pc cm <sup>–3</sup> yr <sup>–1</sup> ) .....	–0.007(1)	–0.009(2)	–0.001(1)
Orbital Parameters			
Orbital Period (days) .....	0.362618545(8)	1.09442881(5)	0.513338066(9)
Orbital Period Derivative .....	1.38(8) × 10 <sup>–10</sup>	0.0(0)	0.0(0)
Projected Semi-Major Axis (lt-s) ...	1.271836(1)	1.102814(3)	1.498546(4)
Ref. Epoch of Periastron ( $T_0$ , MJD)	53800.32842747(6)	53318.995701960084(6)	53495.2744166(2)
Derived Parameters			
Mass Function ( $M_\odot$ ) .....	0.01679872(5)	0.001202305(9)	0.0137115(1)
Min Companion Mass ( $M_\odot$ ) .....	≥ 0.38	≥ 0.14	≥ 0.35

**Notes**

Numbers in parentheses represent 1- $\sigma$  uncertainties in the last digit as determined by TEMPO, PINT, or via standard error propagation. The timing solutions used the DE440 Solar System Ephemeris and times are all in Barycentric Dynamical Time (TDB), referenced to TT(BIPM2021). The eccentricity and longitude of periastron,  $\omega$ , for each of the binaries were each assumed to be zero. Minimum companion masses were calculated assuming a pulsar mass of 1.4  $M_\odot$ .

Table 4.3: Timing parameters for M28H and NGC 6440D

Parameter	M28H	NGC 6440D
Pulsar Name .....	PSR J1824–2452H	PSR J1748–2021D
Data Reduction		
Span of Timing Data (MJD) .....	53629–60084	53478–59894
Number of TOAs .....	866	574
RMS TOA Residual ( $\mu$ s) .....	46.1	31.9
Reduced $\chi^2$ .....	1.01	1.02
EFAC for incoherent data .....	2.75	1.47
EFAC for coherent data .....	7.37	1.32
Timing Parameters		
Right Ascension (RA, J2000) .....	18 <sup>h</sup> 24 <sup>m</sup> 31 <sup>s</sup> .6098(2)	17 <sup>h</sup> 48 <sup>m</sup> 51 <sup>s</sup> .6457(1)
Declination (DEC, J2000) .....	–24° 52′ 17″.15(4)	–20° 21′ 07″.41(2)
Proper Motion in RA ( $\text{mas yr}^{-1}$ ) ...	–1.1(3)	–1.4(2)
Pulsar Spin Period (ms) .....	4.6294137643019(6)	13.4958205400413(8)
Pulsar Spin Frequency (Hz) .....	216.01007188235(3)	74.097013740888(5)
Spin Frequency Derivative ( $\text{Hz s}^{-1}$ )	$-3.6139(2) \times 10^{-15}$	$-3.22033(1) \times 10^{-15}$
Frequency 2nd Derivative ( $\text{Hz s}^{-2}$ ) .	$-8(9) \times 10^{-28}$	$5(2) \times 10^{-28}$
Reference Epoch (PEPOCH, MJD) .	56856.714649097440997	56686.128079588925175
Dispersion Measure (DM, $\text{pc cm}^{-3}$ ) .	121.38(2)	224.999(6)
DM Derivative ( $\text{pc cm}^{-3} \text{yr}^{-1}$ ) .....	0.014(3)	–0.004(1)
Orbital Parameters		
Orbital Period (days) .....	0.43502746(1)	0.2860686141(6)
Orbital Period Derivative .....	0.0(0)	$-1.7(1) \times 10^{-11}$
Projected Semi-Major Axis (lt-s) ...	0.719473(4)	0.397212(1)
Ref. Epoch of Periastron ( $T_0$ , MJD)	53755.2263970(4)	56479.176207(1)
Derived Parameters		
Mass Function ( $M_\odot$ ) .....	0.00211297(3)	0.000822259(9)
Min Companion Mass ( $M_\odot$ ) .....	$\geq 0.17$	$\geq 0.12$

**Notes**

Numbers in parentheses represent 1- $\sigma$  uncertainties in the last digit as determined by TEMPO, PINT, or via standard error propagation. The timing solutions used the DE440 Solar System Ephemeris and times are all in Barycentric Dynamical Time (TDB), referenced to TT(BIPM2021). The eccentricity and longitude of periastron,  $\omega$ , for each of the binaries were each assumed to be zero. Minimum companion masses were calculated assuming a pulsar mass of  $1.4 M_\odot$ .



## CHAPTER 5

# FUTURE WORK

The works presented in the preceding chapters have opened doors for future studies to advance our knowledge of not only individual binary systems, but also particular types of binaries and their underlying physics. In the text that follows, I will briefly review some of the key takeaways from each chapter. I will also comment on future potential studies that can build off the work presented here.

The HW Vir system presented in Chapter 4 provides a useful benchmark for sdB studies going forward. As previously stated, the fortuitous inclination angle of the system sets it apart from the other known systems in the population. Additionally, this system is relatively bright and has an average orbital period, making it accessible to most telescope aperture classes for both photometric and spectroscopic follow-up observations. These facts, paired with the advent of continued data releases from *Gaia*, bode well for the continued study of this system. Using small/mid-aperture telescopes, one could easily continue to photometrically monitor the eclipses of the system to create a long timing baseline for an O-C analysis of the system. As this particular object now has two-minute-cadence, space-based observations from TESS and will be observed through the Legacy Survey of Space and Time on the Vera C.

Rubin Observatory, accurate timing of a system such as this could give useful insights into the orbital evolution of HW Vir binaries. Perhaps the most interesting avenue to explore would be to obtain higher-resolution spectroscopy using a mid/large-aperture telescope to measure a rotational velocity for the sdB. This information could be used to get a more accurate radius for the sdB, which, paired with distance information from *Gaia*, could also provide a more accurate measurement for its mass. A study of this kind would be relatively straightforward and have benefits to the ongoing conversations about the masses of sdBs.

Chapter 3 represented a pilot study into what could be done with WDMS systems using the high-resolution, NIR spectra available through the APOGEE survey. One encouraging result was that the multi-visit nature of APOGEE's targeting strategy allowed for orbital studies of close, PCE WDMS systems. In the future, studies can potentially use APOGEE data to search for periodicity and maybe even derive orbits for candidate WDMS systems. Anguiano et al. (2022) provides an early example of this, extending the analysis to WD binaries with companions across the H-R diagram. The conclusions of both my work in Chapter 3 and those in Anguiano et al. (2022) in regards to WDMS metallicities provide perhaps the most broad impact and natural place for future studies of these binaries. While my work was drawn from a very small sample of systems, Anguiano et al. (2022) reported similar differences between metallicities of WDMS systems in wide and close binaries. Disentangling the physical mechanisms and processes that lead to a more-enriched surface chemistry of companions in tight orbits could yield valuable insights into the processes occurring during CE evolution. Using the individual elemental abundances available through APOGEE for this growing sample could provide clarity in guiding these investigations as mentioned in Anguiano et al. (2022). Indeed, following on my pilot study and Anguiano et al. (2022), Anguiano, Majewski, and collaborators have obtained NSF funding as well

as large allotments of time with the Las Cumbres Observatory as well as the NEID spectrograph on the WIYN 3.5-m telescope to add epochs of radial velocity data to the APOGEE database to solve the orbits of a number of more WDMS systems, with the goal of building a larger statistical sample to approach such questions. Studies making use of targeted, high-resolution observations to derive metallicities for a larger sample could also provide additional key insights. However, selecting such a sample and obtaining the requisite telescope time to perform these analyses are non-trivial tasks.

Many studies and improvements are possible in the future stemming from the work presented in Chapter 4. The ROI technique, while extremely useful in its current state, is by no means complete. As previously mentioned, there are large systematics presently left unmodeled to keep the number of parameters in the problem manageable. A direct continuation of this work would be to leverage the multi-frequency information in observations to account for DM variations and delays on both long-term and even per-observation basis. This process could significantly improve the accuracy of each measurement for the time of periastron passage, leading to better characterization of the changing orbit over the timing baseline. Additionally, we have only applied our methods to a small sample of RBs. Going forward, studies can make use of the ROI technique to create long-term timing solutions for other RBs. This process will likely increase the viability of obtaining continued observations of RBs in the radio, which would certainly help increase our understanding of these systems. While the ROI technique is in principle designed for observations obtained in the radio, it would be interesting to see if the methods presented in Chapter 4 could be extended to long-term timing efforts using high-energy photons from the *Fermi* mission. From a physical standpoint, future studies should continue to investigate the correlation between the fractional deviation of a RB's phase variations and its spin period. Com-

parisons between the phase variations in RBs and those observed in other compact binaries with M dwarf companions, such as those in Parsons et al. (2010b), could potentially give insights into the physical processes driving the variations. Finally, additional investigations of the dynamics in RB orbits as they pertain to changes in the companion star should be carried out, and more long-baseline datasets for other RBs would be useful in facilitating this process.

## REFERENCES

- Alpar, M. A., Cheng, A. F., Ruderman, M. A., & Shaham, J. 1982, *Nature*, 300, 728
- Anguiano, B., Lewis, H. M., Corcoran, K. A., et al. 2020, *Research Notes of the American Astronomical Society*, 4, 127
- Anguiano, B., Majewski, S. R., Stassun, K. G., et al. 2022, *The Astronomical Journal*, 164, 126
- Applegate, J. H. 1992, *The Astrophysical Journal*, 385, 621
- Applegate, J. H., & Shaham, J. 1994, *The Astrophysical Journal*, 436, 312
- Archibald, A. M., Kaspi, V. M., Hessels, J. W. T., et al. 2013, arXiv e-prints, arXiv:1311.5161
- Arzoumanian, Z., Fruchter, A. S., & Taylor, J. H. 1994, *The Astrophysical Journal Letters*, 426, L85
- Astropy Collaboration, Robitaille, T. P., Tollerud, E. J., et al. 2013, *Astronomy and Astrophysics*, 558, A33
- Astropy Collaboration, Price-Whelan, A. M., Sipőcz, B. M., et al. 2018, *The Astronomical Journal*, 156, 123
- Astropy Collaboration, Price-Whelan, A. M., Lim, P. L., et al. 2022, *The Astrophysical Journal*, 935, 167
- Badenes, C., Mazzola, C., Thompson, T. A., et al. 2018, *The Astrophysical Journal*, 854, 147

- Bahramian, A., Strader, J., Miller-Jones, J. C. A., et al. 2020, *The Astrophysical Journal*, 901, 57
- Baraffe, I., Homeier, D., Allard, F., & Chabrier, G. 2015, *Astronomy and Astrophysics*, 577, A42
- Barlow, B. N., Wade, R. A., & Liss, S. E. 2012, *The Astrophysical Journal*, 753, 101
- Barlow, B. N., Corcoran, K. A., Parker, I. M., et al. 2022, *The Astrophysical Journal*, 928, 20
- Beauchamp, A., Wesemael, F., & Bergeron, P. 1997, *The Astrophysical Journal Supplement Series*, 108, 559
- Beers, T. C., Christlieb, N., Norris, J. E., et al. 2005, in *IAU Symposium*, Vol. 228, *From Lithium to Uranium: Elemental Tracers of Early Cosmic Evolution*, ed. V. Hill, P. Francois, & F. Primas, 175–183
- Bégin, S. 2006, Master's thesis, University of British Columbia, Canada
- Bellm, E. C., Kaplan, D. L., Breton, R. P., et al. 2016, *The Astrophysical Journal*, 816, 74
- Bianchi, L., Shiao, B., & Thilker, D. 2017, *The Astrophysical Journal Supplement Series*, 230, 24
- Bilous, A. V., Ransom, S. M., & Demorest, P. 2019, *The Astrophysical Journal*, 877, 125
- Blandford, R., & Teukolsky, S. A. 1976, *The Astrophysical Journal*, 205, 580
- Blanton, M. R., Bershadsky, M. A., Abolfathi, B., et al. 2017, *The Astronomical Journal*, 154, 28
- Bleach, J. N., Wood, J. H., Catalán, M. S., et al. 2000, *Monthly Notices of the Royal Astronomical Society*, 312, 70
- Bogdanov, S., Bahramian, A., Heinke, C. O., et al. 2021, *The Astrophysical Journal*, 912, 124

- Bogdanov, S., van den Berg, M., Servillat, M., et al. 2011, *The Astrophysical Journal*, 730, 81
- Bradley, L., Sipócz, B., Robitaille, T., et al. 2019, *astropy/photutils: v0.6*, , , doi:10.5281/zenodo.2533376
- Brown, A. J., Parsons, S. G., van Roestel, J., et al. 2023, *Monthly Notices of the Royal Astronomical Society*, 521, 1880
- Bundy, K., Bershadsky, M. A., Law, D. R., et al. 2015, *The Astrophysical Journal*, 798, 7
- Burdge, K. B., Coughlin, M. W., Fuller, J., et al. 2019, *Nature*, 571, 528
- Burdge, K. B., Marsh, T. R., Fuller, J., et al. 2022, *Nature*, 605, 41
- Butler, K., & Giddings, J. R. 1985, in *Newsletter of Analysis of Astronomical Spectra*, No. 9 (Univ. London)
- Calvet, N., & Gullbring, E. 1998, *The Astrophysical Journal*, 509, 802
- Camacho, J., Torres, S., García-Berro, E., et al. 2014, *Astronomy and Astrophysics*, 566, A86
- Chen, K., & Ruderman, M. 1993, *The Astrophysical Journal*, 402, 264
- Chui, C. K. 1992, *Wavelets: A tutorial in theory and applications*
- Claret, A., & Bloemen, S. 2011, *Astronomy and Astrophysics*, 529, A75
- Clark, C. J., Nieder, L., Voisin, G., et al. 2021, *Monthly Notices of the Royal Astronomical Society*, 502, 915
- Clemens, J. C., Crain, J. A., & Anderson, R. 2004, in *Society of Photo-Optical Instrumentation Engineers (SPIE) Conference Series*, Vol. 5492, Proc. SPIE, ed. A. F. M. Moorwood & M. Iye, 331–340
- Cojocaru, R., Rebassa-Mansergas, A., Torres, S., & García-Berro, E. 2017, *Monthly Notices of the Royal Astronomical Society*, 470, 1442

- Copperwheat, C. M., Marsh, T. R., Dhillon, V. S., et al. 2010, *Monthly Notices of the Royal Astronomical Society*, 402, 1824
- Corcoran, K. A., Barlow, B. N., Schaffenroth, V., et al. 2021a, *The Astrophysical Journal*, 918, 28
- Corcoran, K. A., Lewis, H. M., Anguiano, B., et al. 2021b, *The Astronomical Journal*, 161, 143
- Cottaar, M., Covey, K. R., Meyer, M. R., et al. 2014, *The Astrophysical Journal*, 794, 125
- Cottle, J., Covey, K. R., Suárez, G., et al. 2018, *The Astrophysical Journal Supplement Series*, 236, 27
- Cromartie, H. T., Fonseca, E., Ransom, S. M., et al. 2020, *Nature Astronomy*, 4, 72
- Culpan, R., Geier, S., Reindl, N., et al. 2022, *Astronomy and Astrophysics*, 662, A40
- Czesla, S., Schröter, S., Schneider, C. P., et al. 2019, *PyA: Python astronomy-related packages*, , , ascl:1906.010
- Dahm, S. E. 2008, *The Young Cluster and Star Forming Region NGC 2264*, ed. B. Reipurth, 966
- Deneva, J. S., Ray, P. S., Camilo, F., et al. 2021, *The Astrophysical Journal*, 909, 6
- Derekas, A., Németh, P., Southworth, J., et al. 2015, *The Astrophysical Journal*, 808, 179
- DuPlain, R., Ransom, S., Demorest, P., et al. 2008, in *Society of Photo-Optical Instrumentation Engineers (SPIE) Conference Series*, Vol. 7019, *Advanced Software and Control for Astronomy II*, ed. A. Bridger & N. M. Radziwill, 70191D
- Duquenois, A., & Mayor, M. 1991, *Astronomy and Astrophysics*, 500, 337
- Farihi, J., Hoard, D. W., & Wachter, S. 2010, *The Astrophysical Journal Supplement Series*, 190, 275
- Foreman-Mackey, D. 2016, *The Journal of Open Source Software*, 1, 24

- Foreman-Mackey, D., Hogg, D. W., Lang, D., & Goodman, J. 2013, *Publications of the Astronomical Society of the Pacific*, 125, 306
- Frasca, A., Molenda-Żakowicz, J., De Cat, P., et al. 2016, *Astronomy and Astrophysics*, 594, A39
- Freire, P. C. C. 2013, in *Neutron Stars and Pulsars: Challenges and Opportunities after 80 years*, ed. J. van Leeuwen, Vol. 291, 243–250
- Freire, P. C. C., Ransom, S. M., Bégin, S., et al. 2008, *The Astrophysical Journal*, 675, 670
- Freire, P. C. C., Ridolfi, A., Kramer, M., et al. 2017, *Monthly Notices of the Royal Astronomical Society*, 471, 857
- Gaia Collaboration, Brown, A. G. A., Vallenari, A., et al. 2018, *Astronomy and Astrophysics*, 616, A1
- García Pérez, A. E., Allende Prieto, C., Holtzman, J. A., et al. 2016, *The Astronomical Journal*, 151, 144
- Geier, S., Raddi, R., Gentile Fusillo, N. P., & Marsh, T. R. 2019, *Astronomy and Astrophysics*, 621, A38
- Ghosh, A., Bhattacharyya, B., Lyne, A., et al. 2024, *The Astrophysical Journal*, 965, 64
- Giddings, J. R. 1981, PhD thesis, Univ. London
- Gold, T. 1968, *Nature*, 218, 731
- Guidry, J. A., Vanderbosch, Z. P., Hermes, J. J., et al. 2020, arXiv e-prints, arXiv:2012.00035
- Gunn, J. E., Siegmund, W. A., Mannery, E. J., et al. 2006, *The Astronomical Journal*, 131, 2332
- Han, Z., Podsiadlowski, P., Maxted, P. F. L., & Marsh, T. R. 2003, *Monthly Notices of the Royal Astronomical Society*, 341, 669

- Han, Z., Podsiadlowski, P., Maxted, P. F. L., Marsh, T. R., & Ivanova, N. 2002, *Monthly Notices of the Royal Astronomical Society*, 336, 449
- Heber, U. 2016, *Publications of the Astronomical Society of the Pacific*, 128, 082001
- Hessels, J. W. T., Ransom, S. M., Stairs, I. H., et al. 2006, *Science*, 311, 1901
- Hjellming, M. S., & Taam, R. E. 1991, *The Astrophysical Journal*, 370, 709
- Holtzman, J. A., Shetrone, M., Johnson, J. A., et al. 2015, *The Astronomical Journal*, 150, 148
- Holtzman, J. A., Hasselquist, S., Shetrone, M., et al. 2018, *The Astronomical Journal*, 156, 125
- Hong, J., van den Berg, M., Schlegel, E. M., et al. 2005, *The Astrophysical Journal*, 635, 907
- Hubeny, I., Hummer, D. G., & Lanz, T. 1994, *Astronomy and Astrophysics*, 282, 151
- Hulse, R. A., & Taylor, J. H. 1975, *The Astrophysical Journal Letters*, 195, L51
- Ingleby, L., Calvet, N., Herczeg, G., et al. 2013, *The Astrophysical Journal*, 767, 112
- Irrgang, A., Kreuzer, S., Heber, U., & Brown, W. 2018, *Astronomy and Astrophysics*, 615, L5
- Ivanova, N., Justham, S., Chen, X., et al. 2013, *A&A Rev.*, 21, 59
- Jacoby, B. A., Cameron, P. B., Jenet, F. A., et al. 2006, *The Astrophysical Journal Letters*, 644, L113
- Jones, D., Boffin, H. M. J., Rodríguez-Gil, P., et al. 2015, *Astronomy and Astrophysics*, 580, A19
- Jönsson, H., Holtzman, J. A., Allende Prieto, C., et al. 2020, arXiv e-prints, arXiv:2007.05537
- Kaplan, D. L., Escoffier, R. P., Lacasse, R. J., et al. 2005, *Publications of the Astronomical Society of the Pacific*, 117, 643

- Kawahara, H., Masuda, K., MacLeod, M., et al. 2018, *The Astronomical Journal*, 155, 144
- Kilkenny, D. 2014, *Monthly Notices of the Royal Astronomical Society*, 445, 4247
- Kilkenny, D., Hilditch, R. W., & Penfold, J. E. 1978, *Monthly Notices of the Royal Astronomical Society*, 183, 523
- Knight, A. H., Ingram, A., van den Eijnden, J., et al. 2023, *Monthly Notices of the Royal Astronomical Society*, 520, 3416
- Kounkel, M., Covey, K., Suárez, G., et al. 2018, *The Astronomical Journal*, 156, 84
- Kruse, E., & Agol, E. 2014, *Science*, 344, 275
- Kupfer, T., Korol, V., Littenberg, T. B., et al. 2024, *The Astrophysical Journal*, 963, 100
- Kurucz, R. L. 1996, in *Model Atmospheres and Spectrum Synthesis*, ed. S. J. Adelman, F. Kupka, & W. W. Weiss (San Francisco: ASP), 160
- Large, M. I., Vaughan, A. E., & Mills, B. Y. 1968, *Nature*, 220, 340
- Lewis, H. M., Anguiano, B., Stassun, K. G., et al. 2020, arXiv e-prints, arXiv:2008.05962
- Lewis, H. M., Anguiano, B., Majewski, S. R., et al. 2022, *Monthly Notices of the Royal Astronomical Society*, 509, 3355
- Lightkurve Collaboration, Cardoso, J. V. d. M., Hedges, C., et al. 2018, *Lightkurve: Kepler and TESS time series analysis in Python*, *Astrophysics Source Code Library*, , ascl:1812.013
- Lucy, L. B. 1967, *ZA*, 65, 89
- Luo, J., Ransom, S., Demorest, P., et al. 2021, *The Astrophysical Journal*, 911, 45
- Lyne, A. G., Manchester, R. N., D'Amico, N., et al. 1990, *Nature*, 347, 650
- Majewski, S. R., Schiavon, R. P., Frinchaboy, P. M., et al. 2017, *The Astronomical Journal*, 154, 94

- Manchester, R. N., Hobbs, G. B., Teoh, A., & Hobbs, M. 2005, *The Astronomical Journal*, 129, 1993
- Martsen, A. R., Ransom, S. M., DeCesar, M. E., et al. 2022, *The Astrophysical Journal*, 941, 22
- Masuda, K., Kawahara, H., Latham, D. W., et al. 2019, *The Astrophysical Journal Letters*, 881, L3
- Maxted, P. F. L., Heber, U., Marsh, T. R., & North, R. C. 2001, *Monthly Notices of the Royal Astronomical Society*, 326, 1391
- Mazzola, C. N., Badenes, C., Moe, M., et al. 2020, arXiv e-prints, arXiv:2007.09059
- Miraval Zanon, A., Burgay, M., Possenti, A., & Ridolfi, A. 2018, in *Journal of Physics Conference Series*, Vol. 956, *Journal of Physics Conference Series (IOP)*, 012004
- Miszalski, B., Acker, A., Moffat, A. F. J., Parker, Q. A., & Udalski, A. 2009, *Astronomy and Astrophysics*, 496, 813
- Napiwotzki, R., Green, P. J., & Saffer, R. A. 1999, *The Astrophysical Journal*, 517, 399
- Naslim, N., Jeffery, C. S., Hibbert, A., & Behara, N. T. 2013, *Monthly Notices of the Royal Astronomical Society*, 434, 1920
- Nebot Gómez-Morán, A., Gänsicke, B. T., Schreiber, M. R., et al. 2011, *Astronomy and Astrophysics*, 536, A43
- Newton, E. R., Charbonneau, D., Irwin, J., et al. 2014, *The Astronomical Journal*, 147, 20
- Nice, D. J., Arzoumanian, Z., & Thorsett, S. E. 2000, in *Astronomical Society of the Pacific Conference Series*, Vol. 202, *IAU Colloq. 177: Pulsar Astronomy - 2000 and Beyond*, ed. M. Kramer, N. Wex, & R. Wielebinski, 67
- Nice, D. J., Thorsett, S. E., Taylor, J. H., & Fruchter, A. S. 1990, *The Astrophysical Journal Letters*, 361, L61

- Nidever, D. L., Holtzman, J. A., Allende Prieto, C., et al. 2015, *The Astronomical Journal*, 150, 173
- Nieder, L., Clark, C. J., Kandel, D., et al. 2020, *The Astrophysical Journal Letters*, 902, L46
- Nieva, M. F., & Przybilla, N. 2008, *Astronomy and Astrophysics*, 481, 199
- Pacini, F. 1967, *Nature*, 216, 567
- Padmanabh, P. V., Ransom, S. M., Freire, P. C. C., et al. 2024, *Astronomy and Astrophysics*, 686, A166
- Pallanca, C., Dalessandro, E., Ferraro, F. R., et al. 2010, *The Astrophysical Journal*, 725, 1165
- Parsons, S. G., Marsh, T. R., Copperwheat, C. M., et al. 2010a, *Monthly Notices of the Royal Astronomical Society*, 402, 2591
- Parsons, S. G., Rebassa-Mansergas, A., Schreiber, M. R., et al. 2016, *Monthly Notices of the Royal Astronomical Society*, 463, 2125
- Parsons, S. G., Marsh, T. R., Copperwheat, C. M., et al. 2010b, *Monthly Notices of the Royal Astronomical Society*, 407, 2362
- Parsons, S. G., Marsh, T. R., Gänsicke, B. T., et al. 2012a, *Monthly Notices of the Royal Astronomical Society*, 420, 3281
- . 2012b, *Monthly Notices of the Royal Astronomical Society*, 419, 304
- Parsons, S. G., Schreiber, M. R., Gänsicke, B. T., et al. 2015, *Monthly Notices of the Royal Astronomical Society*, 452, 1754
- Parsons, S. G., Gänsicke, B. T., Marsh, T. R., et al. 2018, *Monthly Notices of the Royal Astronomical Society*, 481, 1083
- Pedregosa, F., Varoquaux, G., Gramfort, A., et al. 2011, *Journal of Machine Learning Research*, 12, 2825
- Phinney, E. S. 1992, *Philosophical Transactions of the Royal Society of London Series A*, 341, 39

- Phinney, E. S. 1993, in *Astronomical Society of the Pacific Conference Series*, Vol. 50, *Structure and Dynamics of Globular Clusters*, ed. S. G. Djorgovski & G. Meylan, 141
- Pietrukowicz, P., Mróz, P., Soszyński, I., et al. 2013, *Acta Astron.*, 63, 115
- Polzin, E. J., Breton, R. P., Stappers, B. W., & LOFAR PWG. 2018, in *Pulsar Astrophysics the Next Fifty Years*, ed. P. Weltevrede, B. B. P. Perera, L. L. Preston, & S. Sanidas, Vol. 337, 396–397
- Prager, B. J. 2017, PhD thesis, University of Virginia
- Prager, B. J., Ransom, S. M., Freire, P. C. C., et al. 2017, *The Astrophysical Journal*, 845, 148
- Press, W. H., Teukolsky, S. A., Vetterling, W. T., & Flannery, B. P. 1992, *Numerical recipes in FORTRAN. The art of scientific computing*
- Prestage, R. M., Bloss, M., Brandt, J., et al. 2015, in *2015 URSI-USNC Radio Science Meeting*, 4
- Price-Whelan, A. M. 2017, *The Journal of Open Source Software*, 2, 388
- Price-Whelan, A. M., Hogg, D. W., Foreman-Mackey, D., & Rix, H.-W. 2017, *The Astrophysical Journal*, 837, 20
- Price-Whelan, A. M., Hogg, D. W., Rix, H.-W., et al. 2020, *The Astrophysical Journal*, 895, 2
- Przybilla, N., Butler, K., Becker, S. R., & Kudritzki, R. P. 2006a, *Astronomy and Astrophysics*, 445, 1099
- Przybilla, N., Nieva, M. F., & Edelmann, H. 2006b, *Baltic Astronomy*, 15, 107
- Raghavan, D., McAlister, H. A., Henry, T. J., et al. 2010, *The Astrophysical Journal Supplement Series*, 190, 1
- Ransom, S. 2011, *PRESTO: Pulsar Exploration and Search TOOLkit*, *Astrophysics Source Code Library*, record ascl:1107.017, ,
- Ransom, S. M. 2001, PhD thesis, Harvard University, Massachusetts

- Ransom, S. M. 2008, in *Dynamical Evolution of Dense Stellar Systems*, ed. E. Vesperini, M. Giersz, & A. Sills, Vol. 246, 291–300
- Ransom, S. M., Hessels, J. W. T., Stairs, I. H., et al. 2005, *Science*, 307, 892
- Rasmussen, C. E., & Williams, C. K. I. 2006, *Gaussian Processes for Machine Learning* (The MIT Press)
- Rebassa-Mansergas, A., Agurto-Gangas, C., Schreiber, M. R., Gänsicke, B. T., & Koester, D. 2013, *Monthly Notices of the Royal Astronomical Society*, 433, 3398
- Rebassa-Mansergas, A., Gänsicke, B. T., Schreiber, M. R., Koester, D., & Rodríguez-Gil, P. 2010, *Monthly Notices of the Royal Astronomical Society*, 402, 620
- Rebassa-Mansergas, A., Parsons, S. G., Dhillon, V. S., et al. 2019, *Nature Astronomy*, 3, 553
- Rebassa-Mansergas, A., Ren, J. J., Parsons, S. G., et al. 2016a, *Monthly Notices of the Royal Astronomical Society*, 458, 3808
- Rebassa-Mansergas, A., Zorotovic, M., Schreiber, M. R., et al. 2012, *Monthly Notices of the Royal Astronomical Society*, 423, 320
- Rebassa-Mansergas, A., Anguiano, B., García-Berro, E., et al. 2016b, *Monthly Notices of the Royal Astronomical Society*, 463, 1137
- Rebassa-Mansergas, A., Ren, J. J., Irawati, P., et al. 2017, *Monthly Notices of the Royal Astronomical Society*, 472, 4193
- Ren, J. J., Rebassa-Mansergas, A., Parsons, S. G., et al. 2018, *Monthly Notices of the Royal Astronomical Society*, 477, 4641
- Ren, J. J., Rebassa-Mansergas, A., Luo, A. L., et al. 2014, *Astronomy and Astrophysics*, 570, A107
- Rios-Venegas, C., Contreras-Quijada, A., Vogt, N., et al. 2020, *Monthly Notices of the Royal Astronomical Society*, 493, 1197
- Roberts, M. S. E. 2013, in *Neutron Stars and Pulsars: Challenges and Opportunities after 80 years*, ed. J. van Leeuwen, Vol. 291, 127–132

- Romani, R. W., Graham, M. L., Filippenko, A. V., & Zheng, W. 2016, *The Astrophysical Journal*, 833, 138
- Romani, R. W., Kandel, D., Filippenko, A. V., Brink, T. G., & Zheng, W. 2022, *The Astrophysical Journal Letters*, 934, L17
- Rosenthal, A. C., Ransom, S. M., Corcoran, K. A., et al. 2024, arXiv e-prints, arXiv:2410.21648
- Saffer, R. A., Bergeron, P., Koester, D., & Liebert, J. 1994, *The Astrophysical Journal*, 432, 351
- Scargle, J. D. 1982, *The Astrophysical Journal*, 263, 835
- Schaffenroth, V., Barlow, B. N., Drechsel, H., & Dunlap, B. H. 2015, *Astronomy and Astrophysics*, 576, A123
- Schaffenroth, V., Classen, L., Nagel, K., et al. 2014a, *Astronomy and Astrophysics*, 570, A70
- Schaffenroth, V., Geier, S., Drechsel, H., et al. 2013, *Astronomy and Astrophysics*, 553, A18
- Schaffenroth, V., Geier, S., Heber, U., et al. 2014b, *Astronomy and Astrophysics*, 564, A98
- Schaffenroth, V., Barlow, B. N., Geier, S., et al. 2019, *Astronomy and Astrophysics*, 630, A80
- Schaffenroth, V., Casewell, S. L., Schneider, D., et al. 2020, *Monthly Notices of the Royal Astronomical Society*, arXiv:2011.10013
- Schreiber, M. R., Gänsicke, B. T., Rebassa-Mansergas, A., et al. 2010, *Astronomy and Astrophysics*, 513, L7
- Soker, N. 1998, *The Astronomical Journal*, 116, 1308
- Soszyński, I., Stępień, K., Pilecki, B., et al. 2015, *Acta Astron.*, 65, 39
- Souto, D., Cunha, K., Smith, V. V., et al. 2020, *The Astrophysical Journal*, 890, 133

- Stoughton, C., Lupton, R. H., Bernardi, M., et al. 2002, *The Astronomical Journal*, 123, 485
- Strader, J., Swihart, S., Chomiuk, L., et al. 2019, *The Astrophysical Journal*, 872, 42
- Susobhanan, A., Kaplan, D., Archibald, A., et al. 2024, arXiv e-prints, arXiv:2405.01977
- Swihart, S. J., Strader, J., Chomiuk, L., et al. 2022, *The Astrophysical Journal*, 941, 199
- Swihart, S. J., Strader, J., Shishkovsky, L., et al. 2018, *The Astrophysical Journal*, 866, 83
- Tauris, T. M., & van den Heuvel, E. P. J. 2006, in *Compact stellar X-ray sources*, Vol. 39, 623–665
- Thongmearkom, T., Clark, C. J., Breton, R. P., et al. 2024, *Monthly Notices of the Royal Astronomical Society*, 530, 4676
- Tody, D. 1986, in *Society of Photo-Optical Instrumentation Engineers (SPIE) Conference Series*, Vol. 627, Proc. SPIE, ed. D. L. Crawford, 733
- Tody, D. 1993, in *Astronomical Society of the Pacific Conference Series*, Vol. 52, *Astronomical Data Analysis Software and Systems II*, ed. R. J. Hanisch, R. J. V. Brissenden, & J. Barnes, 173
- Tolosa, O., Breedt, E., De Martino, D., et al. 2019, , 51, 168
- Tonry, J. L., Denneau, L., Heinze, A. N., et al. 2018, *Publications of the Astronomical Society of the Pacific*, 130, 064505
- Torres, G., Andersen, J., & Giménez, A. 2010, *A&A Rev.*, 18, 67
- Tremblay, P. E., & Bergeron, P. 2009, *The Astrophysical Journal*, 696, 1755
- Troup, N. W., Nidever, D. L., De Lee, N., et al. 2016, *The Astronomical Journal*, 151, 85
- Urquhart, R., Bahramian, A., Strader, J., et al. 2020, *The Astrophysical Journal*, 904, 147

- van den Heuvel, E. P. J., & van Paradijs, J. 1988, *Nature*, 334, 227
- Vasiliev, E., & Baumgardt, H. 2021, *Monthly Notices of the Royal Astronomical Society*, 505, 5978
- Vennes, S., Christian, D. J., & Thorstensen, J. R. 1998, *The Astrophysical Journal*, 502, 763
- Virtanen, P., Gommers, R., Oliphant, T. E., et al. 2020a, *Nature Methods*, doi:<https://doi.org/10.1038/s41592-019-0686-2>
- . 2020b, *Nature Methods*, 17, 261
- von Zeipel, H. 1924, *Monthly Notices of the Royal Astronomical Society*, 84, 665
- Vos, J., Vučković, M., Chen, X., et al. 2019, *Monthly Notices of the Royal Astronomical Society*, 482, 4592
- Vurgun, E., Linares, M., Ransom, S., et al. 2022, *The Astrophysical Journal*, 941, 76
- Webbink, R. F. 2008, in *Astrophysics and Space Science Library*, Vol. 352, *Astrophysics and Space Science Library*, ed. E. F. Milone, D. A. Leahy, & D. W. Hobill, 233
- Wenger, M., Ochsenbein, F., Egret, D., et al. 2000, *Astronomy and Astrophysics Supplement Series*, 143, 9
- White, R. J., & Basri, G. 2003, *The Astrophysical Journal*, 582, 1109
- Willems, B., & Kolb, U. 2004, *Astronomy and Astrophysics*, 419, 1057
- Wilson, J. C., Hearty, F. R., Skrutskie, M. F., et al. 2019, *Publications of the Astronomical Society of the Pacific*, 131, 055001
- Yap, Y. X. J., Kong, A. K. H., & Li, K.-L. 2023, *The Astrophysical Journal*, 955, 21
- York, D. G., Adelman, J., Anderson, John E., J., et al. 2000, *The Astronomical Journal*, 120, 1579
- You, X. P., Manchester, R. N., Coles, W. A., Hobbs, G. B., & Shannon, R. 2018, *The Astrophysical Journal*, 867, 22

Yuan, H., Liu, X., Xiang, M., et al. 2015, *The Astrophysical Journal*, 799, 135

Zasowski, G., Johnson, J. A., Frinchaboy, P. M., et al. 2013, *The Astronomical Journal*, 146, 81

Zasowski, G., Cohen, R. E., Chojnowski, S. D., et al. 2017, *The Astronomical Journal*, 154, 198

Zhao, G., Zhao, Y., Chu, Y., Jing, Y., & Deng, L. 2012, arXiv e-prints, arXiv:1206.3569

Zorotovic, M., Schreiber, M. R., & Gänsicke, B. T. 2011, *Astronomy and Astrophysics*, 536, A42